QUANTUM TUNNELING, FIELD INDUCED INJECTING CONTACT, AND EXCITONS

Thesis by

Yixin Liu

In Partial Fulfillment of the Requirements

for the Degree of

Doctor of Philosophy

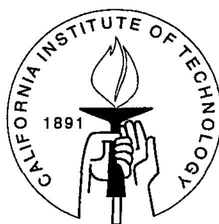

California Institute of Technology

Pasadena, California

1995

(Submitted March 9, 1995)

To my grandma and aunt

Acknowledgements

There are many people that I am greatly indebted to during my graduate career at Caltech. First, I would like to thank my advisor, Professor Tom McGill, for offering me the unique opportunity to work in his exceptionally well-equipped research group and providing me with technical guidance. His remarkable intuition and keen insight into physics problems have always been enlightening, and greatly influenced my own way of thinking. I also thank him for his help and comments on my paper and thesis writings.

Special thanks to our wonderful secretary, Marcia Hudson, for her crucial and superb administrative work that has kept the group operating smoothly and efficiently. Her friendliness and smile have also been a constant source of cheer and happiness for me in the group.

I want to thank Professor J. O. McCaldin for suggesting the work of injecting contact to me. I have benefited a great deal from his expertise on physical chemistry and semiconductor devices.

I have been extremely fortunate to be surrounded by a host of tremendously talented and equally generous people, past and present members of the McGill group. The interactions with them have enriched my experience and knowledge immensely. I am particularly indebted to Dr. David Ting. In addition to many fruitful discussions and guidance on technical issues, Dave has provided me with critical support and sound advice during my stay in the group. His friendship and good nature of manner will always be remembered and appreciated. It has

also been a great pleasure to have Dr. Shaun Kirby as a colleague and a friend. I enjoyed working closely with him during his tenure in the group. Besides, he was also a fun companion to conference and skiing trips, an enthusiastic partner for tennis and racketball. His friendliness and good nature have made our interactions extremely enjoyable. Dr. David Chow provided me with many helps when I first joined the group. His guidance and patience are truly appreciated. I have benefited tremendously from discussions and collaborations with Drs. Yasantha Rajakarunanayake, Mark Phillips, and Ron Marquardt on numerous research projects. I enjoyed many fascinating conversations with Dr. Doug Collins. Our business venture together has been a very "rewarding" experience. I am extremely grateful to Dr. Mike Wang and Johanes Swenberg for their kindness and patience in providing me assistance and advice whenever I needed. I have benefited a great deal from working with Dr. Harold Levy and Chris Springfield on the computer system administration. Their enthusiasm and wits have stimulated much of my own interests in the field. I have always enjoyed the interactions with Per-Olov Patterson. His enthusiasm of sharing his knowledge with others has always made our conversation very fascinating. Rob Miles, I missed his laugh and daily lunch hour comments that had kept the group in a lively spirit. I have also enjoyed interactions with Mike Jackson, Ed Yu, Ed Croke, J. R. Söderström, David Reich, Erik Daniel, Xiao-Chang Chen, Alicia Alonzo, Zvonimir Bandic, Eric Piquette, and Paul Bridger.

Outside the group, I enjoyed the interactions and friendship with many fellow Chinese students on campus, particularly with Bin Zhao, Mingsheng Han, Yong Guo, and Xinlei Hua, etc. It has served as a tie to my ethnic background, a channel of consultation and mutual encouragement when adjusting our lives here while experiencing the dramatic changes back in China.

Finally, I would like to thank my parents and brothers. Their unconditional love and faith in me have always been a major source of inspiration over the many years. I owe special thanks to my wife, Yili, for her love, understanding, and

encouragement, without which my accomplishment today would be impossible. I would like to dedicate this thesis to my grandmother and aunt. Their unselfish breeding will always be appreciated throughout my life, and their wholehearted love will be treasured deeply in my heart.

List of Publications

Work related to this thesis has been, or will be, published under the following titles:

An Efficient, Numerically Stable Multiband k·p Treatment of Quantum Transport in Tunnel structures,,
Y. X. Liu, D. Z.-Y. Ting, and T. C. McGill, to be published in *Phys. Rev. B* (1995).

Resonant Magnetotunneling in Interband Tunnel Structures,
Y. X. Liu, D. Z.-Y. Ting, R. R. Marquardt, and T. C. McGill, to be submitted to *Phys. Rev. B* .

Resonant Magnetotunneling Spectroscopy of p-well Interband Tunneling Diodes,
R.R. Marquardt, D.A. Collins, Y.X. Liu, D. Z.-Y. Ting, and T.C. McGill, *Proc. of Microscopic and Mesoscopic Systems*, Hawaii, (1994), also submitted to *Phys. Rev.* **B.**.

Multiband k·p Treatment of Quantum Transport in a Magnetic Field,
Y. X. Liu, D. Z.-Y. Ting, and T. C. McGill, APS 1993 March Meeting, Seattle, Washington. *Bull. Am. Phys. Soc.* **38**, 401 (1993).

Magnetotunneling in Interband Tunnel Structures,

Y. X. Liu, D. Z.-Y. Ting, and T. C. McGill, *Proc. of International Workshop on Quantum Structures*, Santa Barbara, California, (1993).

Novel Aspects of InAs/AlSb/GaSb Quantum Well and Tunnel Structures,

D. Z.-Y. Ting, H.J. Levy, S.K. Kirby, Y.X. Liu, R. M. Marquardt, D.A. Collins, E.S. Daniels, and T.C. McGill, *Proc. of International Workshop on Sb Based Systems*, Santa Barbara, California, (1993).

Schottky Barrier Induced Injecting Contact on Wide Bandgap Semiconductors,

Y.X. Liu, M.W. Wang, J.O. McCaldin, and T.C. McGill, *J. Vac. Sci. Technol. B* **10**, No.4, 2072(1992).

Exciton in II-VI Heterostructures,

Y.X. Liu, Y. Rajakarunanayake, and T.C. McGill, *J. Cryst. Growth* **117**, 742(1992).

Proposal for the Formation of a Minority Carrier Injecting Contact on Wide Bandgap Semiconductors,

Y.X. Liu, M.W. Wang, J.O. McCaldin, and T.C. McGill, *J. Cryst. Growth* **117** 913(1992).

Forming of Al-doped ZnTe Epilayers Grown by Molecular Beam Epitaxy,

M.C. Phillips, J.F. Swenberg, Y.X. Liu, M.W. Wang, J.O. McCaldin, and T.C. McGill, *J. Cryst. Growth* **117** 1050(1992).

Growth and Characterization of ZnTe Films Grown on GaAs, InAs and GaSb,

Y. Rajakarunanayake, Y.X. Liu, D.H. Chow, J. R. Söderström, B.H. Cole, J.O. McCaldin, and T.C. McGill, *Proc. of 4th Intern. Conf. on II-VI Compounds*, Berlin, Germany, (1989).

Abstract

This thesis consists of three parts: Quantum tunneling simulation, Schottky barrier induced injecting contact on wide band gap II-VI materials, and excitons in semiconductor heterostructures.

Part I (chapter 2, 3) deals with quantum transport and electronic band structure in semiconductor heterostructures. In chapter 2, we present a new method for quantum transport calculations in tunnel structures employing multiband $\mathbf{k}\cdot\mathbf{p}$ theory. This method circumvents the numerical instability problems that arise in the standard transfer-matrix method. In addition to being numerically stable, efficient, and easy to implement, this method can also be easily generalized to include the magnetic field and strain effects. The development of this technique mainly consists of two parts, the discretization of effective-mass Schrödinger's equation using finite-difference method, and the formulation of boundary conditions. The treatment of boundary condition in quantum transport is similar to the Multiband Quantum Transmitting Boundary Method (MQTBM) for use with multiband tight-binding models. The calculations of transmission coefficients reduce to a set of linear equations, which can be solved very easily. With appropriate formulation of boundary conditions, this technique can be readily extended to the calculations of electronic band structures in quantum confinement and superlattice structures. We have applied this new technique to magnetotunneling in interband tunnel structures in chapter 3, and studied two prototypical device structures: Resonant Interband Tunneling (RIT) devices and Barrierless Resonant Interband

Tunneling (BRIT) devices. Effects of transverse magnetic field on the band structures, transmission spectrum, and $I-V$ characteristics are investigated. Evidence of heavy-hole resonance contribution can be identified in the change of $I-V$ characteristics under applied magnetic field. The technique has also been illustrated for hole tunneling in p-type GaAs/AlAs double barrier tunnel structures, and calculations of electronic band structures in lattice-matched InAs/GaSb superlattices, and strained InAs/$Ga_{1-x}In_xSb$ superlattices.

Part II describes a novel approach to achieve ohmic injecting contact on wide bandgap II-VI semiconductors. The problem of making good ohmic contact to wide bandgap II-VI materials has been a major challenge in the effort of making visible light emitting diodes. The method we propose consists of forming the device structure in an electric field at elevated temperatures in the Schottky barrier region, to spatially separate the ionized dopants from the compensating centers. In this way, the ratio of dopants to compensating centers can be greatly increased at the semiconductor surface. Upon cooling, the dopant concentrations are frozen to retain a large net concentration of dopants in a thin surface layer, resulting in a depletion layer that is sufficiently thin to allow tunneling injection. Calculations of band profiles, distributions of dopant concentrations, and current-voltage characteristics were performed. We have selected the case of Al doped ZnTe in our study, in which two Al donors complex with a doubly negatively ionized Zn vacancy to produce total compensation. The results show that the bulk doping concentration and the total band bending during the forming process are the crucial factors for achieving injecting contacts. For Schottky barrier heights above 1 eV, doping concentrations as high as 10^{20} cm^{-3} are needed.

In part III, we studied excitons in semiconductor heterostructures, consisting of two subjects: excitons in II-VI heterostructures, and exciton coherent transfer process in quantum structures. Calculations of exciton binding energies and oscillator strengths are performed in both Type-I strained CdTe/ZnTe superlattices with very small valence-band offset and Type-II strained ZnTe/ZnSe superlattices.

A special variational approach was employed to take into account the effects of unusual band alignment, strain, and image charges at the heterojunction interface. It is found that the large enhancements of exciton binding energy and oscillator strength in the CdTe/ZnTe system are similar to what one finds in systems with a much larger valence band offset. For small CdTe layer thickness, however, the confinement of holes in the CdTe layer is weak, resulting in a lowering of the exciton binding energy. The oscillator strength in CdTe/ZnTe superlattice system shows the expected enhancement over the oscillator strengths in the bulk.

For the ZnTe/ZnSe system, the Type-II character of the heterojunction results in the confinement of the electrons and holes in different layers. It is found that strong confinement of electrons and holes by the large band offsets can give rise to a fairly large exciton binding energy for thin heterojunction layers. Also, the mismatch in dielectric constants induces an image charge at the interface, which modifies significantly the exciton Hamiltonian in an asymmetric superlattice structure and plays an important role in determining the degree of localization of the electron and hole at the interface.

We have investigated exciton coherent transfer in semiconductor quantum structures. In systems where the typical dimensions of the semiconductor quantum structures and the spacings between them are significantly smaller than the photon wavelength, the resonant transfer of excitons between two identical quantum structures is accomplished through the interaction of near field dipole-dipole transitions (exchange of virtual photons). The transfer matrix elements are calculated for three different geometries: quantum wells, quantum wires and quantum dots, respectively. The results show that the exciton transfer matrix element is proportional to exciton oscillator strength, and depends on exciton polarization. The transfer matrix element between quantum wells depends on the exciton wave vector in the plane of the wells, $\mathbf{k}_{\|}$, and vanishes when $\mathbf{k}_{\|} = 0$. For quantum wire and quantum dot structures, the transfer matrix elements between two units separated by R vary as R^{-2} and R^{-3}, respectively. For quantum structures with

typical characteristic size of 50 Å with separation about 100 Å, the transfer matrix element is on the order of 10^{-3} meV. It corresponds to a resonant transfer time of 1 ns, comparable with the exciton lifetime. However, it is significantly smaller than the inhomogeneous broadening due to phonons and structural imperfection in most synthesized semiconductor quantum structures achievable today, which is typically on the order of a few meV, making the realization of experimental observation difficult. The study is to explore new ideas and potential technological applications based on excitonic devices.

Contents

Acknowledgements iii

List of Publications vi

Abstract ix

List of Figures xiv

List of Tables xvii

1 Introduction 1

1.1 Multiband **k·p** Theory of Quantum Transport and Electronic Band Structures in Semiconductor Heterostructures 2

1.1.1 Motivation 2

1.1.2 Multiband Effective Mass Theory 5

1.1.3 Boundary Conditions 7

1.1.4 Applications 10

1.2 Schottky Barrier Induced Injecting Contact on Wide Bandgap II-VI Semiconductors 13

1.2.1 Motivation 13

1.2.2 Schottky Barrier Induced Injecting Contact 16

1.3 Excitons in II-VI Heterostructures and Exciton Coherent Transfer in Semiconductor Nanostructures 19

1.3.1 Motivation 19
1.3.2 Exciton Binding Energies and Oscillator Strengths in II-VI Heterostructures 22
1.3.3 Exciton Coherent Transfer in Semiconductor Nanostructures 23

2 Multiband k·p Treatment of Quantum Tunneling and Electronic Band Structures in Semiconductor Heterostructures 32

2.1 Introduction 32
2.1.1 Background 32
2.1.2 Outline of Chapter 34
2.2 Review of Existing Methods 35
2.2.1 Transfer-Matrix Method 36
2.2.2 Scattering Matrix Method 39
2.2.3 Tight-binding Method 40
2.3 Multiband **k·p** Method 42
2.3.1 **k·p** Hamiltonian 42
2.3.2 Strain Effect 45
2.3.3 Discretization of Schrödinger's Equation 46
2.3.4 Current Density Operator and Treatment of Heterostructure Interface 48
2.4 Quantum Tunneling 50
2.4.1 Boundary Conditions 50
2.4.2 Calculation of Transmission Coefficients 52
2.4.3 Comparison with Other Existing Methods 54
2.5 Applications to *p*-type GaAs/AlAs Double Barrier 54
2.6 Calculations of Electronic Band Structures 59
2.6.1 Confined Quantum Structures 59
2.6.2 Superlattices 61
2.7 Summary 68

3 Magnetotunneling in Interband Tunnel Structures 72

3.1 Introduction 72

3.2 Method 75

3.3 Resonant Interband Tunneling (RIT) Structures 78

3.3.1 Band Structures in GaSb Well 78

3.3.2 Transmission Coefficients 79

3.3.3 Current-Voltage Characteristics 82

3.4 Barrierless Resonant Interband Tunneling (BRIT) Structures 86

3.4.1 Transmission Coefficients 86

3.4.2 Current-Voltage Characteristics 87

3.5 Discussions 90

3.6 Summary 91

4 Schottky Barrier Induced Injecting Contact on Wide Bandgap II-VI Semiconductors 94

4.1 Introduction 94

4.2 Proposal and Calculation 95

4.3 Study of Al Doped ZnTe 100

4.4 Summary 106

5 Excitons in Semiconductor Heterostructures 110

5.1 Excitons in II-VI Heterostructures 110

5.1.1 Introduction 110

5.1.2 CdTe/ZnTe Type I Heterostructure 111

5.1.3 Type II ZnTe/ZnSe System 116

5.2 Exciton Coherent Transfer in Semiconductor Nanostructures 122

5.2.1 Introduction 122

5.2.2 Theory 123

5.2.3 Quantum Dots 126

5.2.4 Quantum Wires 129
5.2.5 Quantum Wells 132
5.2.6 Discussions 135
5.2.7 Summary 137

A Eight-band k·p Hamiltonian **141**

A.1 Basis and **k·p** Hamiltonian 141
A.2 Strain Induced Hamiltonian 143
A.3 Interaction of Spin and Magnetic Field 144

B Exciton Transfer Matrix Element in Quantum Structures **147**

B.1 Basis Functions and Hamiltonian 147
B.2 Band Offset Model and Effective Mass Approximation 150
B.3 Local Exciton States 152
B.4 Exciton Transfer Matrix Elements 154
B.4.1 Tunneling 154
B.4.2 Dipole Transitions 154

List of Figures

1.1 Discretization of device structure 6
1.2 Band alignment in the InAs/GaSb/AlSb material systems 11
1.3 Schematic of ohmic contacts 15
1.4 Schematic energy band diagram before and after forming 17
1.5 Energy band diagrams of CdTe/ZnTe and ZnTe/ZnSe heterostructures 21

2.1 Illustration of quantum tunneling in heterostructures 36
2.2 Disrectization of band profile in transfer-matrix method 37
2.3 Scattering-matrix method 39
2.4 Discretization of device regions 47
2.5 Transmission coefficients at $k_{\|} = 0$ in GaAs/AlAs 55
2.6 Transmission coefficients for heavy-hole channel in GaAs/AlAs at $k_{\|} \neq 0$ 57
2.7 Transmission coefficients for light-hole channel in GaAs/AlAs at $k_{\|} \neq 0$ 58
2.8 Schematic diagram of quantum well states 60
2.9 Hole dispersion in GaAs quantum well 62
2.10 Schematic band diagram of superlattices 63
2.11 Schematic band diagram of lattice-matched InAs/GaSb superlattice 64
2.12 Electronic band structure of InAs/GaSb superlattice 65
2.13 Schematic band diagram of strained InAs/$Ga_{1-x}In_xSb$ superlattice . 66

2.14 Electronic band structures of strained InAs/$Ga_{1-x}In_xSb$ superlattice 67

3.1 Schematic band diagrams of BRIT and RIT structures 74

3.2 Transverse magnetic field applied to tunnel structures 76

3.3 Hole subband dispersions in RIT structure without magnetic field . 80

3.4 Hole subband dispersions in RIT structure with magnetic field . . . 81

3.5 Transmission coefficients for RIT structure 83

3.6 $I-V$ characteristics for RIT with magnetic field 84

3.7 Measured $I-V$ characteristics for a p-well RIT device 85

3.8 Transmission coefficients for BRIT structure 88

3.9 $I-V$ curve for BRIT structure 89

4.1 Schematic of the forming process 97

4.2 Schematic energy diagram of Schottky contact before and after the forming process 98

4.3 Calculated vacancy density distribution 101

4.4 $I-V$ curves for various forming conditions at $N_{Al} = 10^{20}cm^{-3}$ . . . 103

4.5 $I-V$ curves for various forming conditions at $N_{Al} = 10^{19}cm^{-3}$ . . . 104

4.6 $I-V$ and charge distribution for doubly and singly ionized mobile charge 105

4.7 Experimental $I-V$ before and after forming 107

5.1 Schematic band diagram of CdTe/ZnTe and ZnTe/ZnSe heterostructures 112

5.2 Exciton binding energy as a function of ZnTe and CdTe layer thickness 115

5.3 Exciton binding energy as a function of CdTe layer thickness 117

5.4 Oscillator strength in CdTe/ZnTe 118

5.5 Exciton binding energy as a function of ZnTe and ZnSe layer thickness 120

5.6 Energy contribution due to Image charge 121

5.7 Exciton band dispersion in one-dimensional quantum dot array . . . 127

5.8 Exciton band dispersion in three-dimensional quantum dot arrays . 128
5.9 Exciton band dispersion in one-dimensional quantum wire array . . 131
5.10 Exciton band dispersion in quantum well superlattices 134

List of Tables

1.1 Doping types achievable for some II-VI semiconductors 13
1.2 List of Schottky barrier heights for some metals on ZnTe 14
1.3 Summary of exciton transfer matrix in various structures 25
5.1 Parameters used in II-VI exciton calculations 114
5.2 Summary of results for quantum wells, quantum wires, quantum dot, and anthracene 136

Chapter 1

Introduction

This thesis consists of three parts. The first part (chapter 2 and 3) presents an efficient and numerically stable method for quantum transport and electronic band structures calculations in heterostructures using multiband $\mathbf{k}\cdot\mathbf{p}$ theory, and discusses its applications to a number of III-V heterostructures. The second part (chapter 4) describes a novel approach to achieve minority injecting contact to II-VI wide bandgap materials using forming process. The third part (chapter 5) is devoted to excitons in semiconductor heterostructures, including the calculations of exciton binding energies and oscillator strengths in Type I and Type II wide bandgap II-VI heterostructures, and exciton coherent transfer process in various low-dimensional semiconductor structures: quantum wells, quantum wires and quantum dots.

1.1 Multiband k·p Theory of Quantum Transport and Electronic Band Structures in Semiconductor Heterostructures

1.1.1 Motivation

Physics of tunneling phenomena in semiconductor heterostructures has been a subject of considerable investigation since the early work of Tsu and Esaki[1]. Advances in epitaxial growth techniques such as molecular beam epitaxy (MBE) and metalorganic chemical vapor deposition (MOCVD) have made possible the experimental realization of these structures, whose fabrication requires control of layer thickness with resolution close to a single atomic layer.

A key feature of interest in tunnel structures is the negative differential resistance (NDR) in the current-voltage characteristic. The NDR behavior can be used in a number of applications, with considerable success having been achieved for high-frequency oscillators[2, 3]. Applications for extraction of spatial discontinuities in artificial retinas and logic circuits based on the large peak-to-valley ratio in the $I - V$ characteristics exhibited in resonant interband tunneling devices have also been explored[4, 5].

Extensive theoretical work has been carried out to understand, simulate and design tunnel device structures[6, 7, 8, 9, 10, 11]. Elastic transport processes are in general responsible for giving rise to the main features observed in the current-voltage characteristics. Various scattering processes, such as electron-phonon scattering, electron-electron scattering, impurity scattering, and interface roughness, are neglected. These scattering effects are important for detailed account of $I - V$ characteristics. They mainly modify the valley current in the tunneling devices, but are all very difficult to treat quantitatively and correctly.

The central issue in quantum tunneling calculation is the computation of trans-

mission coefficients. The theoretical models for calculations of transmission coefficients range from the simplest in which the electrons are described by a single effective band (one-band model) to where the entire band structures of the constituent layers are included (multiband model). While a simple one-band model can explain the qualitative behavior of electron tunneling in GaAs/AlAs double-barrier resonant tunneling structures(DBRT), it is essential to employ multiband band-structure model to understand and simulate the behavior of hole tunneling in p-type GaAs/AlAs heterostructures[12, 13, 14, 15] and resonant interband tunnel structures involving InAs/GaSb/AlSb systems[16, 17].

Among the theoretical techniques being developed, The transfer-matrix method[18] has been the best well-known technique in the calculation of transmission coefficients, being widely used in various situations[1, 12, 13, 14, 19]. In one-band model applied to electron tunneling in n-type GaAs/AlAs system[1], the transfer-matrix method gives satisfactory results. However, when used in conjunction with realistic multiband band-structure models, particularly when the active device structures are larger than a few tens of Å, the transfer-matrix method becomes numerically unstable[20, 13]. The origin of the instability lies in the presence of the exponentially growing states in a barrier region. The transfer-matrix methods treats the growing and decaying states on the equal footing, resulting in the swamping of the exponentially decaying wave function during computation by the exponentially growing wave function. The error propagates and is magnified in the successive multiplication of matrices. Various modifications have been proposed to deal with this problem. However, they are simply truncation schemes of differing degree of complexity. For the purpose of resonant tunneling, such schemes are undesirable because, on resonance, the growing and the decaying states contribute equally to the wave function.

To circumvent the numerical difficulties that arises in transfer-matrix calculation, several techniques have been proposed recently[16, 21, 22]. The S-matrix method proposed by Ko and Inkson[21] is essentially a reformulation of transfer-

matrix method. Unlike transfer-matrix method which relates the wave functions at the final layer on the right-hand side to the wave functions at the first layer on the left-hand side through a transfer-matrix $\mathbf{T}$, the S-matrix method separates the wave functions on both sides into incoming incident waves and outgoing scattering waves, and relates the outgoing scattering states to the incoming incident states via the scattering matrix $\mathbf{S}$. By doing so, the physics of tunneling process is more faithfully described and the less localized and the propagating states dominate numerically, ensuring numerical stability. However, the construction of $\mathbf{S}$ matrix involves an iterative procedure that is not as easy to use as the transfer-matrix method, which simply involves the product of matrices. Thus, the gain in stability in the S-matrix method is compensated by the numerical inefficiency.

The Multiband Quantum Transmitting Boundary Method (MQTBM) proposed by Ting *et al.* [16] is a major step in circumventing the numerical instability while providing an efficient and easy to implement technique in multiband simulation of quantum tunneling in semiconductor heterostructures. MQTBM is a multiband generalization of Frensley's [23] one-band effective mass approximation implementation of the Quantum Transmitting Boundary Method (QTBM), originally developed by Lent and Kirkner [24] for treating electron waveguide using a finite-element approach. Ting has implemented the method based on the multiband effective bond-orbital model [25] developed by Chang. This model is essentially a reformulation of Kane's multiband $\mathbf{k}\cdot\mathbf{p}$ model [26] in the tight-binding framework. The method has been successfully applied to the studies of interband tunneling in the InAs/GaSb/AlSb systems[16, 17], and hole tunneling in the GaAs/AlAs double-barrier heterostructures.[15] It has also been implemented in a Slater-Koster second-neighbor sp^3 tight-binding model[27] for studying X-point tunneling.[28] The calculation of transmission coefficient in MQTBM becomes a simple problem of solving a system of linear equations. The method has been demonstrated to be numerically stable for device structures wider than 2000Å. In addition to being as efficient as the transfer-matrix method, this method is

considerably simpler to implement than the transfer-matrix method.

Despite the success of this method in numerous applications, the tight-binding model that Ting's method is based on is inconvenient when applied to systems involving external magnetic field and strain effects. **k·p** method, on the other hand, is naturally suited for dealing with magnetic field and strain effects. Since the study of magnetic field and strain effects are extremely important for understanding the electronic structure and carrier transport properties in semiconductor heterostructures[29, 30, 31, 32] and exploring band structure engineering in lattice-mismatched heterostructure systems[33], our goal is to develop a similar method for quantum tunneling study based on multiband **k·p** theory[34]. Also the same technique can be applied to the calculations of electronic band structures for quantum confinement states and superlattices with appropriate modifications of boundary conditions.

1.1.2 Multiband Effective Mass Theory

The effective mass theory developed by Luttinger and Kohn[35] is particularly suited for studying the electronic states near the Brillouin zone center in periodic crystals with external fields. The basic results of the effective mass theory are that if the external potential V varies slowly over the unit cell, the effect of the periodic field of lattice can be replaced by a set of parameters $H_{ij}(\mathbf{k})$, which are determined by the unperturbed bulk band structure. The solutions to the original Schrödinger's equation can be obtained by solving the following coupled effective mass differential equations

$$\sum_{j=1}^{M} \left[H_{ij}(-i\nabla) + V(\mathbf{r})\delta_{ij}\right] F_j = EF_i \,, \tag{1.1}$$

where the envelope functions F_i is related to the wave function by

$$\psi = \sum_{i=1}^{M} F_i u_{i0}, \tag{1.2}$$

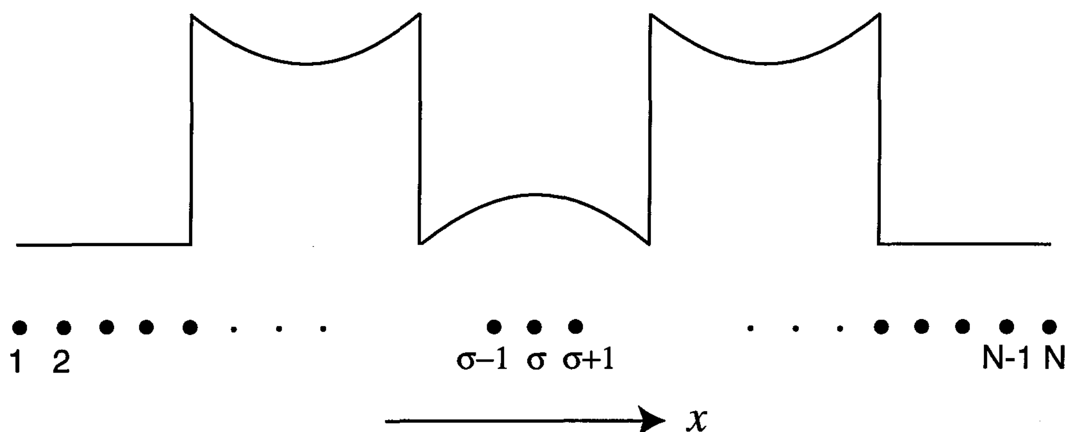

Figure 1.1: The entire device region is discretized into N mash points, typically with spacing equal to the crystal lattice constant.

where M is the number of energy bands involved in the model, u_{i0} are the Bloch basis with lattice periodicity, and the form of matrix elements $H_{ij}(\mathbf{k})$ are determined by the $\mathbf{k}\cdot\mathbf{p}$ method[26].

We consider one-dimensional problem in semiconductor heterostructures in which the system varies only along the growth direction – x axis, and is translational invariant in the lateral directions. The transfer-matrix method uses a numerical technique similar to the shooting method for solving differential equation problems[36]. It first solves the effective mass Schrödinger's equation (1.1) in general forms at each piece-wise constant potential layer across the device structure, and then starts from one boundary and successively relates the solutions at each layer to its previous one through a transfer matrix $\mathbf{T}$, and arrives at the other boundary. This numerical technique is known to become unstable in the case of trying to maintain a dying exponential in the presence of growing exponentials during the shooting process[36], which often is the case for tunnel structures in the barrier regions.

We employ a very different numerical approach – finite-difference method –

in solving the effective mass Schrödinger's equation (1.1). The idea is similar to the relaxation method[36], which replaces the differential equations by finite difference equations on a mesh of points that cover the range of interests. To do this, we discretize the entire device region into a mash of N points along the growth direction, typically with equal spacing, as shown in Fig. 1.1. Effective mass theory assumes that the external potential V and, thereby, the envelope function F vary slowly over the unit cell. If the spacing a is taken to be on the order of lattice constant, the derivatives of envelope function at each discretized point x_σ can therefore be well approximated by finite differences

$$\frac{\partial F}{\partial x}|_{x_\sigma} \Longrightarrow \frac{F_{\sigma+1} - F_\sigma}{a}, \tag{1.3}$$

$$\frac{\partial^2 F}{\partial x^2}|_{x_\sigma} \Longrightarrow \frac{F_{\sigma+1} + F_{\sigma-1} - 2F_\sigma}{a^2}. \tag{1.4}$$

In the second-order $\mathbf{k{\cdot}p}$ model, the M coupled second order differential Schrödinger's Eq. (1.1) can then be transformed into M linear finite difference equations at each discretized point σ

$$\mathbf{H}_{\sigma,\sigma+1}\mathbf{F}_{\sigma+1} + \mathbf{H}_{\sigma,\sigma}\mathbf{F}_\sigma + \mathbf{H}_{\sigma,\sigma-1}\mathbf{F}_{\sigma-1} = 0, \tag{1.5}$$

where we have used the vector notation $\mathbf{F}_\sigma$ to refer to the entire set of envelope functions $\{ F_1, \cdots, F_M\}$ at point x_σ, and $\mathbf{H}_{\sigma,\sigma'}$ are $M \times M$ matrices.

Equation (1.5) only applies to a given material region in a heterostructure. At the heterojunction interface, the current and wave function continuity conditions lead to a similar linear difference equation at the interface (details are given in section 2.3.4). Therefore the effective mass Schrödinger's equations are replaced by a set of linear equations for the entire regions of heterostructure. Combined with appropriate boundary conditions, the problems can be readily solved.

1.1.3 Boundary Conditions

Quantum Tunneling

The boundary conditions for quantum tunneling problems are that we have known incoming plane-wave state from the left region. Part of the incident wave is reflected and part is transmitted. In simple one-band model, the boundary conditions are described by

$$F_L = Ie^{ik_L x} + re^{-ik_L x}, \tag{1.6}$$

$$F_R = te^{ik_R x}, \tag{1.7}$$

for the left and right flat band regions, where I represents the known incoming plane-wave state, while t and r describe the unknown transmitted and reflected states.

In Quantum Transmitting Boundary Method (QTBM)[23, 24], the two boundaries at $\sigma = 1$ and $\sigma = N$ are extended to flat band regions where electron states are plane-wave like satisfying Eqs. (1.6) and (1.7), respectively. The basic idea is to eliminate the unknown t and r, and establish a relationship between F_1 and F_2 on left boundary through Eq. (1.6), and similarly for F_{N-1} and F_N on the right boundary through Eq. (1.7). By doing so, we can obtain the following two equations at the boundaries

$$F_1 - e^{ik_L a} F_2 = I(1 - e^{i2k_L a}), \tag{1.8}$$

$$F_{N-1} e^{ik_R a} - F_N = 0. \tag{1.9}$$

These two equations, together with the discretized Schrödinger's Eq. (1.5), constitute a system of linear equations that completely determine the solutions for the tunneling problem. Solving this system of linear equations yields the entire envelope function profile, and from Eq.(1.7), the coefficient of transmitted plane-wave states t can be calculated by

$$t = e^{-ik_R (N-1)a} F_N. \tag{1.10}$$

The implementation of QTBM in multiband band structure models is a bit more sophisticated, though the basic idea is the same. It will be discussed in detail in chapter 2.

Electronic Band Structures in Quantum Confinements and Superlattices

Unlike quantum tunneling problems where the electron states are propagating plane-waves, the electron states in confined quantum structures such as quantum wells are spatially localized in the heterostructure growth direction. The wave function decays exponentially in the barrier regions and goes to zero at infinity. The boundaries are chosen so that mesh points 1 and N are deep enough into the barrier regions, the wave functions at these positions are sufficiently small so that they can be neglected to the tolerance of numerical accuracy. The boundary conditions for confinement states therefore can be simply represented by

$$\mathbf{F}_1 = 0, \tag{1.11}$$

$$\mathbf{F}_N = 0. \tag{1.12}$$

Combined with Eq. (1.5), the solutions to electronic band structures in confined states becomes a simple eigenvalue problem.

Superlattice is a periodic structure consisting of alternating layers of different materials. Since superlattice displays translational symmetry in the growth direction x with periodicity d, we can associate with that a quantum number q, the wave-vector along the x direction. The Bloch condition

$$\psi(x + md) = e^{imqd}\psi(x) \tag{1.13}$$

implies the following boundary condition

$$\mathbf{F}_N = \mathbf{F}_0 e^{iqd}. \tag{1.14}$$

This homogeneous condition, together with Eq. (1.5), also forms an eigenvalue problem. Solving this eigenvalue problem yields the superlattice electronic subband dispersion $E(q)$.

1.1.4 Applications

We have applied this new technique to several prototypical device structures. Our primary interest is to study the magnetotunneling effects in InAs/GaSb/AlSb based interband tunnel structures. The nearly lattice-matched InAs/GaSb/AlSb material system has been a subject of extensive studies due to the tremendous flexibility it offers for heterostructure device design. The relative positions of conduction-band and valence-band edges for InAs, GaSb and AlSb are shown in Fig. 1.2. The band offsets in this material system include Type I between GaSb and AlSb, Type II staggered between InAs and AlSb, and Type II broken-gap between InAs and GaSb[1]. The most interesting band alignment is the Type II broken-gap between InAs and GaSb, since the band gaps of the two materials do not overlap with the conduction-band edge of InAs 0.15 eV below the valence-band edge of GaSb. Interband Tunnel Structures (ITS) exploit device systems involving transport and coupling between electron states in InAs conduction-band and hole states in GaSb valence-band.

Various interband devices have been studied both experimentally and theoretically[37]−[42], revealing rich physics and great potential in device applications. Among them, two device structures are of particular interest because of the physics and technological applications involved[4, 5, 16]. One is the Resonant Interband Tunneling (RIT) structure made up of InAs-AlSb-GaSb-AlSb-InAs, and the other is Barrierless Resonant Interband Tunneling (BRIT) structure consisting of a GaSb well sandwiched between two InAs electrodes. The primary interband transport mechanism arises from the coupling between the light-hole states in GaSb well and InAs conduction-band states[9]. Although the heavy-hole states in the GaSb well are believed to introduce additional transmission resonances and substantial

[1]In Type-I band alignment, the smaller band gap of one semiconductor lies completely within the larger band gap of the other; In Type-II band alignment, the band is staggered with the band gaps of the two materials either overlap or broken, but one does not completely enclose the other.

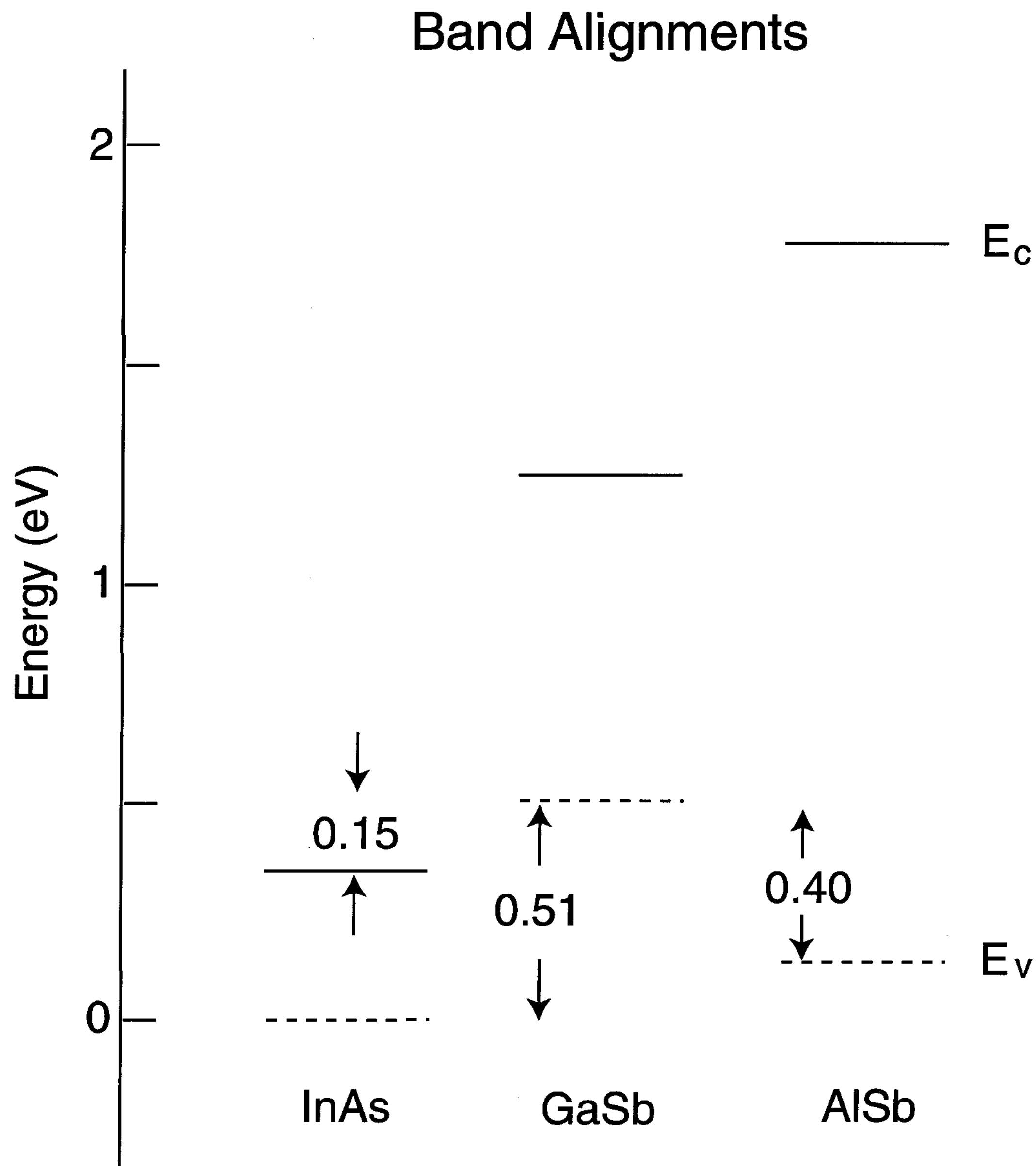

Figure 1.2: Relative positions of the conduction (solid) and valence (dashed) band edges for the InAs/GaSb/AlSb material systems. The energy gaps and band offsets allow the possibility of Type I, Type II, and Type II broken-gap band alignments. The indirect conduction band minimum in the Δ direction in the Brillouin zone is shown for AlSb.

hole-mixing effects[16], evidence of heavy-hole contributions to the current-voltage characteristics is not clear. Resonant magnetotunneling technique[30], in which the magnetic field is applied perpendicular to the transport direction, provides an effective tool to probe the interactions of incident electrons with various hole subbands in the GaSb well, thus, allows us to examine the role of heavy-holes in the interband tunneling processes.

We employed eight-band **k·p** Hamiltonian in our study of magnetotunneling effects in RIT and BRIT structures. The basis set contains the Γ_6 conduction-band, the Γ_8 light-hole and heavy-hole bands, and the Γ_7 spin-orbit split-off valence-band. The transmission coefficient calculations show that at $B = 0$, the normal incident electrons only couple with the light-hole states in the GaSb well, resulting in a single light-hole transmission resonance peak. For $B \neq 0$, additional narrow heavy-hole resonances are exhibited. The application of transverse magnetic field lends an in-plane momentum to the incident electron, which induce the coupling between electrons and heavy-hole states by the **k·p** component in the Hamiltonian. The heavy-hole resonance widths broaden as the applied B field increases, indicating stronger coupling between the electron states and heavy-hole states. The heavy-hole resonances appear as a shoulder peak developed in the $I - V$ characteristics under applied magnetic field. The effects have been observed experimentally[43], and the change of behavior in $I - V$ agrees well with the calculations, providing direct evidence of heavy-hole contribution to the tunneling process.

We also demonstrated our technique to several other prototypical structures. Transmission coefficients for hole tunneling in p-type GaAs/AlAs double barrier resonant tunneling structures are calculated using 4×4 Luttinger-Kohn Hamiltonian to study the effects of band mixing between the light-hole and heavy-hole states due to quantum confinement. Superlattice constituting strained InAs and $Ga_{1-x}In_xSb$ layers has potential applications as long-wavelength infrared detector [47, 46]. We have calculated the superlattice band structures for this strained system. The results indicate that comparing with the unstrained InAs/GaSb su-

perlattice system, the strain induced shifts of band edges can indeed result in reduction of InAs/$Ga_{1-x}In_xSb$ superlattice band gap, and achieve the desired band gap for long-wavelength infrared detectors.

1.2 Schottky Barrier Induced Injecting Contact on Wide Bandgap II-VI Semiconductors

1.2.1 Motivation

Wide bandgap II-VI semiconductors have great potential for application as optoelectronic materials in the short-wavelength visible light emission. In the research effort of trying to manufacture blue and green light emitting diode (LED) based on wider bandgap II-VI compounds in the last thirty years, a major problem has been the inability of conventional processing to dope them both *n*-type and *p*-type, where selective doping is almost always compensated by opposing charges, arising from defects, impurities or more complex entities[48]. The conventional high doping types achievable for wide bandgap II-VI semiconductors are listed in Table 1.1. Tellurides tend to be *p*-type, the rest *n*-type. This means that the most basic LED structure – the *pn* junction – is very difficult to obtain with II-VI materials.

Materials	ZnS	ZnSe	CdS	ZnTe	CdSe	CdTe
Band Gaps(eV)	3.6	2.7	2.4	2.26	1.74	1.5
Doping Types	n	n p	n	p	n	n p

Table 1.1: High doping types achievable for some wide bandgap II-VI semiconductors.

In recent years, however, new processing methods have overcome this problem

in several cases, most notably producing p-ZnSe by nitrogen plasma doping [49, 50]. Although such doping has led to the first demonstration of blue-green laser diode (LD) and light emitting diodes (LED) [50, 51, 52], the maximum net acceptor concentration saturates at roughly 10^{18} cm^{-3}, which are still not high enough to afford ohmic contact. Large contact resistance typically exists in these devices, and thereby large threshold voltages are required for LEDs and LDs operation.

Good ohmic contact requires either small Schottky barrier height typically existing between a metal and a semiconductor, or high doping concentration in the semiconductor to allow electron tunneling injection[53], as illustrated in Fig. 1.3. A metal does not generally exist with a low enough work function to yield a low Schottky barrier for wide bandgap II-VI materials, as shown for ZnTe in Table 1.2. In such cases the general technique for making an ohmic contact involves the establishment of a heavily doped surface layer to produce a very short depletion region that allows tunneling[56]. For barrier heights as high as the ones found for wide bandgap II-VI compounds, the doping concentration necessary is typically well above 10^{19} cm^{-3}. Doping levels this high have not been reported for bulk n-ZnTe and p-ZnSe.

Metals	Au	Ag	In	Al	Ni	Ta	Pt
ϕ_{Bp}(eV)	1.35	0.65	1.0	0.9	0.65	1.50	0.64

Table 1.2: List of Schottky barrier heights for some metals on ZnTe[54, 55].

The difficulty to achieve high amphoteric doping efficiency in wide bandgap II-VI materials is believed to be caused by self-compensation mechanism. The self-compensation mechanism in the case of Al doped ZnTe has been well-studied and understood[57, 58]. An Al substitute in a Zn site would normally be a donor. As more Al is added to the system, moving the electron free energy up close to the conduction-band, the less covalent bonding, more ionic nature of ZnTe crystal

Ohmic Contacts

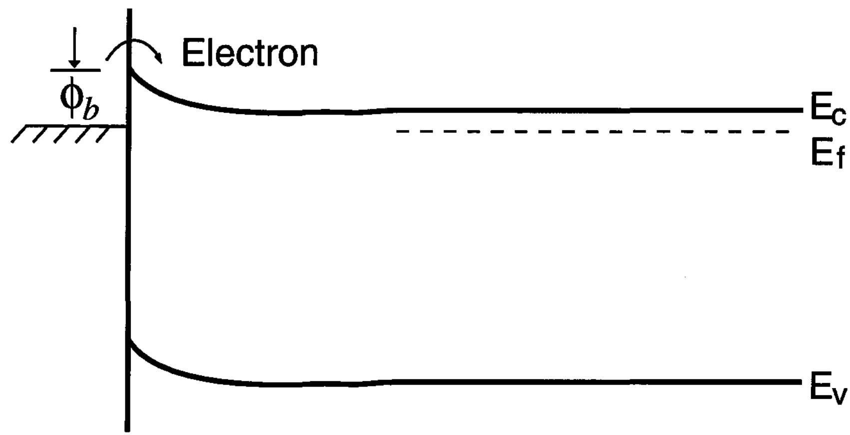

Low Barrier Height

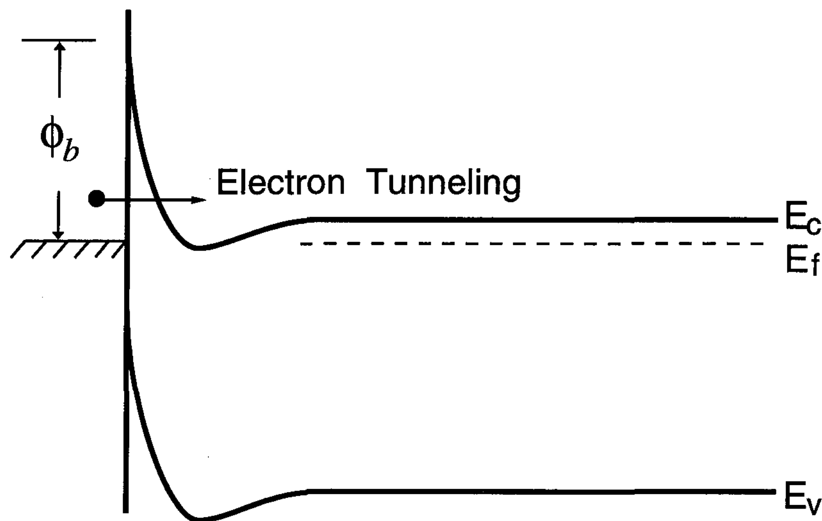

High Doping

Figure 1.3: Schematic illustration of ohmic contact on a n-type semiconductor. Ohmic contact is typically obtained by a metal with low barrier height and/or high doping in the semiconductors, where the electrons can be injected from the metal to the semiconductor through thermionic emission (low barrier) or through tunneling (heavy doping).

would tend to lower the total free energy by creating doubly negatively ionized Zn vacancy. This doubly negatively ionized Zn vacancy combines with neighboring substitutional Al donor impurity to form the so called "A-center", which acts as an acceptor to produce compensation to the Al donor. The typical n-type doping level observed in ZnTe is about $10^{12}/cm^3$, and the resulting ZnTe is semi-insulating.

As an attempt to overcome the difficulty of making ohmic contact to wide bandgap II-VI materials, we have proposed a novel technique to defeat the self-compensation in a very thin layer region near the contacting surface, so that high doping concentration can be achieved, allowing electron tunneling injection.

1.2.2 Schottky Barrier Induced Injecting Contact

The method we propose consists of forming the device structure in an electric field at elevated temperatures, to spatially separate the ionized dopants from the compensating centers. In this way, the ratio of dopants to compensating centers can be greatly increased at the semiconductor surface. Upon cooling, the dopant concentrations are frozen to retain a large net concentration of dopants in a thin surface layer, resulting in a depletion layer that is sufficiently thin to allow tunneling injection. The schematic band diagram at the metal-semiconductor interface before and after the forming process is shown in Fig. 1.4. Before the forming, the nearly perfect self-compensation results in a very lightly doped bulk with very thick depletion layer. After the forming, it produces a very heavily doped region near the surface. If the depletion layer is thin enough, the electrons can thus tunnel through the barrier.

Similar ion drift techniques have been applied successfully to other semiconductor device fabrication. For instance, in making p-i-n diodes doped with Lithium[59, 60], the mobile interstitial Li with positive charge drifts in the built-in field of the p-n junction from the Li^+ rich n side to the Li^+ deficient p side, resulting in the formation of an intrinsic region in between. The drift is usually enhanced by

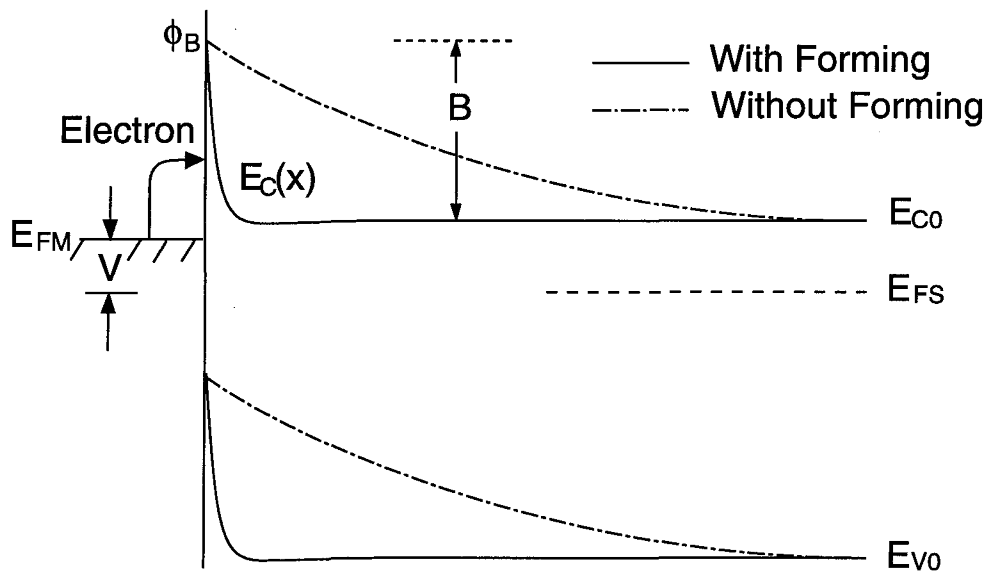

Figure 1.4: The energy diagram at the metal-semiconductor interface before and after the forming process. Before the forming process, the nearly perfect self-compensation results in a very lightly doped bulk where the depletion layer is very thick. After the forming process, the self-compensation is not as effective resulting in a very heavily doped region near the surface and a very thin depletion layer. The total band bending B is a crucial parameter in the forming process.

adding a reverse bias to the built-in field. Another example is the measurement of dissociation kinetics of neutral acceptor-hydrogen complexes and donor-hydrogen complexes in hydrogen passivated Si samples by the forming technique[61, 62]. In this technique, the dopant-hydrogen pairs are thermally dissociated, and the charged hydrogens subsequently drift away from the high field depletion region of the reversed biased Schottky diode near the surface.

Calculations were carried out on Al doped ZnTe. Distributions of mobile Zn vacancies are first calculated under the forming condition by solving Poisson's equation assuming thermal equilibrium distribution is reached. Then the charge distributions are used to calculate the band profile and the tunneling current to obtain the current-voltage characteristics. The results show that the doping concentration and the total band bending B during the forming process are the crucial factors for achieving injecting contacts. The mobile vacancies can be depleted from the surface in an extremely thin region, typically less than 50Å, leaving large concentrations of ionized donors behind to form a tunneling contact. For Schottky barrier heights above 1 eV, doping concentrations as high as 10^{20} cm^{-3} and total band bending above 1.0 V are needed to obtain 100A/cm^2 injecting current density, which is required for laser diode operation. Preliminary experiments have been performed to support that such forming effects do occur in ZnTe doped with Al[63].

1.3 Excitons in II-VI Heterostructures and Exciton Coherent Transfer in Semiconductor Nanostructures

1.3.1 Motivation

Excitons are bound electron-hole pairs and are the lowest electronic excited states in non-metallic crystals. They are easily detected in optical spectra, because they typically give rise to sharp line structure below the fundamental absorption edge, in contrast to broad continuum transitions between the conduction-band and valence-band. In bulk semiconductors, excitons are treated as hydrogen-like entities in the effective mass approximation. Due to smaller effective masses and large dielectric constant in semiconductors, the binding energy of excitons is typically on the order of a few meV and the size of a few tens of Å. The nature of excitons is Wannier-like.

Excitons in low dimensional confinement states usually exhibit higher binding energies and oscillator strengths than those in bulk materials[64]. In ideal 2-dimensional system, for example, the exciton binding energy is four times as large as that in 3-dimensional bulk, while the characteristic Bohr radius of an exciton in 2-D is only one fourth of that in 3-D[65]. Excitons in quantum wells, quantum wires, and quantum dots have been extensively studied[66, 67, 68, 69, 70, 71]. Most of research works has been focused on the study of excitons in Type I GaAs/AlAs quantum well systems. Here we have studied two subjects of great theoretical and technological interests: excitons in II-VI heterostructures and exciton coherent transfer in semiconductor nanostructures.

Strong excitonic luminescences have been reported in both CdTe/ZnTe and ZnTe/ZnSe superlattice systems[72]. In CdTe/ZnTe systems, the valence band offset between CdTe and ZnTe is believed to be small, obeying the common anion rule[73]. As shown in Fig 1.5, the compressive uniaxial strain in the CdTe well

region resulted from large lattice mismatch (6.2%) shifts up the heavy hole valence band and shifts down the light hole valence band, while in the ZnTe barrier region under uniaxial tension the corresponding bands shift in opposite directions, resulting in Type-I band structures for "heavy-hole" excitons and Type-II band structures for "light-hole" excitons. The photoluminescence is primarily due to the free heavy-hole exciton recombination.

The Type-II band alignment in ZnTe/ZnSe system leads to the confinement of electrons and holes in separate adjacent layers. Excitons are formed near the interface. Because of the different dielectric constants in the ZnTe layer and ZnSe layer, image charges are induced at the ZnTe/ZnSe interface, which provides additional Coulomb interactions to the exciton systems. The special band alignments and the intermediate values for the effective masses in wide bandgap II-VI heterostructures raise the interesting question of the role of the attractive interaction between the hole and electron on the binding energy and oscillator strength[74].

Novel semiconductor growth and fabrication techniques have given rise to a new class of man-made structures exhibiting reduced dimensionality and quantum confinement effects, such as quantum wells, quantum wires and quantum dots. These structures are normally large on the scale of a unit cell but small compared with electron mean free path and the wavelengths of optical transitions in the structures. When an exciton localized in a quantum structure recombines and emits a photon, the photon can be reabsorbed creating an exciton in another quantum structure nearby. In systems where the typical dimensions of the semiconductor quantum structures and the spacings between them are significantly smaller than the photon wavelength, the transfer of excitons between different structures is accomplished through the interaction of near field dipole-dipole transitions (exchange of virtual photons).

The study of exciton transfer in semiconductor nanostructures is, in many ways, analogous to exciton transfer behavior in molecular crystals[75, 76]. There the neutral molecules are bound together through the Van der Waals force, which is very

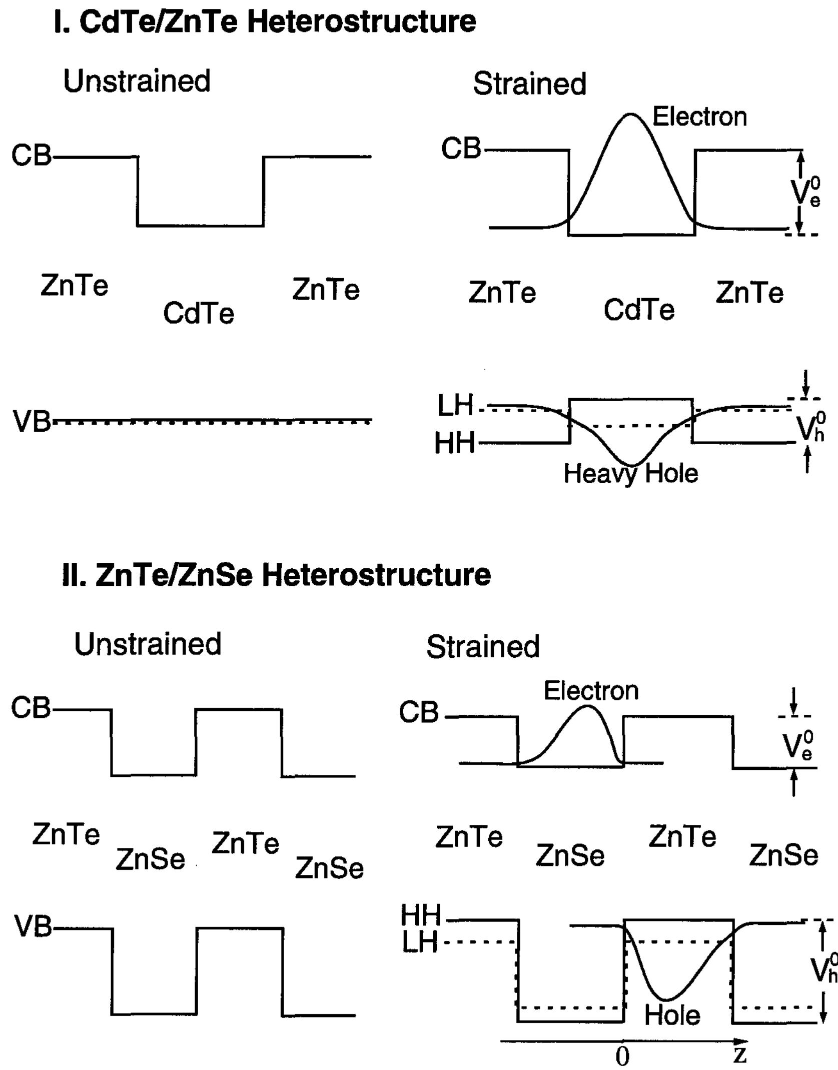

Figure 1.5: A schematic of the valence and conduction band edges in CdTe/ZnTe and ZnTe/ZnSe heterostructures. The conduction band and valence band are shown for both the strained and the unstrained cases. The valence band offset for the CdTe/ZnTe heterojunction without strain is small. Under strain the valence bands are split with the heavy-hole and conduction band forming a Type-I heterostructure and the light-hole and conduction band forming a Type-II. For ZnTe/ZnSe, the accepted values for the band offsets result in Type-II structures for both the strained and unstrained cases. The electron and hole wave functions making up the exciton are hence in different layers.

small compared to the Coulomb force which binds the electrons to the molecules. An exciton in a molecular crystal is therefore strongly localized around a molecule. Such a localized exciton state will propagate from one molecule to another as a result of the interaction of their electric multipole-multipole transitions.

Exciton transfer in molecular crystals plays an important role in various phenomena such as photochemical reactions, delayed fluorescence, etc[76]. Our study of exciton transfer process in semiconductor quantum structure systems is to explore new ideas and potential technological applications based on excitonic devices.

1.3.2 Exciton Binding Energies and Oscillator Strengths in II-VI Heterostructures

The Wannier excitons in semiconductor heterostructures can be described by the effective mass approximation[77, 78]. The effective mass Hamiltonian for excitons is made up of three parts: the electron Hamiltonian in conduction-band quantum well, the hole Hamiltonian in valence-band quantum well, and the Coulomb interaction term between electron and hole. An exact solution to exciton effective mass Schrödinger's equation in quantum wells is not attainable. Variational approach are generally employed for calculations of exciton binding energies and oscillator strengths for excitons. We use the following form of trial wave function for the s-like ground state exciton:

$$\Psi(\vec{r}_{\|}, z_e, z_h) = \psi_e(z_e)\psi_h(z_h)\phi(r_{\|}, z_e - z_h)\,, \tag{1.15}$$

where $\psi_e(z_e)$ and $\psi_h(z_h)$ are taken to be the ground state wave functions in finite square quantum wells, and $\phi(r_{\|}, z) = \exp\left(\frac{-r}{\lambda}\right)$ is of the form of s-like hydrogen ground state wave function, depending only on the relative electron and hole coordinates. The parameter λ characterizes the exciton size.

The Type-I small valence band offset in CdTe/ZnTe only gives rise to weak confinement to the heavy hole state. However, the Coulomb attraction force by the

strongly confined electrons in the conduction band will enhance the localization of heavy holes in the well region. Therefore the effective well potentials determining the forms of trial wave functions $\psi_e(z_e)$ and $\psi_h(z_h)$ are taken to be variational parameters V_e, V_h in our calculations, together with exciton size parameter λ. In Type-II ZnTe/ZnSe system, due to the large band offsets for both conduction band and valence band, we assume that electron and hole are perfectly confined in separate adjacent layers. The image charge formed at the interface due to mismatch in dielectric constants adds additional terms to the exciton Hamiltonian.

Results show [74] that exciton binding energy and oscillator strength in the CdTe/ZnTe system are greatly enhanced compared that in the bulk. For structures of 50Å CdTe and 50Å ZnTe, the exciton binding energy is about 20meV, and the oscillator strength is about 6 times larger than that in the bulk. For small CdTe layer thickness, however, the confinement of holes in the CdTe layer is weak. The leakage of the hole wave function into the surrounding ZnTe layer results in a lowering of the binding energy of the exciton.

For the ZnTe/ZnSe system, although electrons and holes are confined in different layers due to the Type-II character of the band offset, it is found that strong confinement of electrons and holes by the large band offsets can give rise to a very large exciton binding energy for thin heterojunction layers. Exciton binding energy in a 50Å ZnTe and 50Å ZnSe superlattice is about 13meV. Exciton energy due to image charge for an asymmetric structure of 15Å ZnTe and 50Å ZnSe can be as large as 6meV, a significant contribution to the total exciton Hamiltonian.

1.3.3 Exciton Coherent Transfer in Semiconductor Nanostructures

Two distinctive basis are used to describe the exciton transfer in semiconductor quantum structures where the characteristic dimensions are large on the scale of a semiconductor unit cell, but small enough to strongly confine electronic states. The

Wannier exciton model based on the effective mass approximation is used to treat the exciton confined within a single semiconductor quantum structure, while the transfer of localized excitons between quantum structures is described by analogy with the Frenkel excitons in the molecular crystals. Exciton resonant transfer occurs between two identical quantum structures and is accomplished through the interaction of near field dipole-dipole transitions. The exciton transfer matrix element between two quantum structures L and M is given by[79]

$$\Gamma_{\vec{L},\vec{M}} = \iint \phi^*_{\vec{L}}(\vec{r}', \vec{r}') \frac{\vec{\mu}^*_{\vec{L}} \cdot \vec{\mu}_{\vec{M}} - 3(\vec{\mu}^*_{\vec{L}} \cdot \hat{n})(\vec{\mu}_{\vec{M}} \cdot \hat{n})}{\epsilon|\vec{r} - \vec{r}'|^3} \phi_{\vec{M}}(\vec{r}, \vec{r})\, d\vec{r}\, d\vec{r}' , \qquad (1.16)$$

where $\hat{n}$ is the unit vector along $(\vec{r} - \vec{r}')$, and $\vec{\mu}$ is the transition dipole moment between the conduction band and the valence band, $\phi_{\vec{L}}(\vec{r}_e, \vec{r}_h)$ is the exciton envelope function.

The transfer matrix elements are calculated for three different geometries: quantum wells, quantum wires and quantum dots, respectively. The results indicate that the exciton transfer matrix element is proportional to the oscillator strength of an exciton localized in a single quantum structure, and that it depends on the exciton polarization. The transfer matrix element between quantum wells depends on the exciton wave vector in the plane of the wells, $\vec{k}_{\|}$, and vanishes when $\vec{k}_{\|} = 0$. For quantum wire and quantum dot structures, the transfer matrix elements between two units separated by R vary as R^{-2} and R^{-3} respectively. The results are summarized in Table 1.3.

The exciton energy bands and effective masses are also calculated for various configurations of quantum wells, wires, and dots. Numerical analysis on prototypical GaAs/GaAlAs systems indicate that, for quantum structures of typical characteristic size of 50Å with separation about 100Å, the transfer matrix element is on the order of 10^{-3}meV. It corresponds to a resonant transfer time of 1 ns, comparable with the exciton lifetime. However, the inhomogeneous broadening due to structural imperfection and phonons in most synthesized semiconductor quantum structures achievable today is typically on the order of a few meV, sig-

Systems	Well	Wire	Dot	Anthracene
Γ	$\propto \frac{k_\parallel e^{-k_\parallel R}}{a^2}$	$\propto \frac{1}{R^2 a}$	$\propto \frac{1}{R^3}$	$\propto \frac{1}{R^3}$
Dipole Moment	4.3Å	4.3Å	4.3Å	1.3Å
Spacing R	10^2Å	10^2Å	10^2Å	9Å
Exciton Size a	10^2Å	10^2Å	10^2Å	1.3Å
Strength	$10^{-4} \sim 10^{-3}$meV	10^{-3}meV	10^{-3}meV	14meV

Table 1.3: Summary of exciton transfer matrix elements in quantum wells, quantum wires, quantum dots based on GaAs material systems, and their comparison with molecular crystal anthracene. R is the distance between the two structures and a is a parameter characterizing exciton size.

nificantly larger than the coupling between excitons in these structures. Therefore experimental observation of exciton transfer in semiconductor quantum structures is beyond the capability of current nanotechnology. It poses a challenge to future development of nanotechnology.

Bibliography

[1] R. Tsu and L. Esaki, *Appl. Phys. Lett.* **22**, 562 (1973).

[2] T. C. L. G. Sollner, W. D. Goodhue, P. E. Tannenwald, C. D. Parker, and D. D. Peck, *Appl. Phys. Lett.* **43**, 588 (1983).

[3] E. R. Brown, C. D. Parker, L. J. Mahoney, J. R. Söderström, and T. C. McGill, presented at *the 48th Annual Device Research Conference*, Santa Barbara, CA (1990).

[4] H. J. Levy, D. A. Collins, and T. C. McGill, in *Proceedings of the 1992 IEEE International Symposium on Circuits and Systems*, San Diego, CA (1992).

[5] H. J. Levy, and T. C. McGill, *IEEE Trans. Neural Nets* **4**, 427(1993).

[6] B. Ricco and M. Ya. Azbel, *Phys. Rev. B* **29**, 1970 (1984).

[7] W. R. Frensley, *J. Vac. Sci. Technol. B* **3**, 1261 (1985).

[8] S. Luryi, *Appl. Phys. Lett.* **47**, 490 (1985).

[9] J. R. Söderström, E. T. Yu, M. K. Jackson, Y. Rajakarunanayake, and T. C. McGill, *J. Appl. Phys.* **68**, 1372 (1990).

[10] D. Z.-Y. Ting, E. T. Yu, D. A. Collins, D. H. Chow, and T. C. McGill, *J. Vac. Sci. Technol. B* **8**, 810 (1990).

[11] D. Z.-Y. Ting, E. T. Yu, and T. C. McGill, *Appl. Phys. Lett.* **58** 292 (1991).

[12] R. Wessel and M. Altarelli, *Phys. Rev. B* **39**, 12802 (1989).

[13] C. Mailhiot and D. L. Smith, *Phys. Rev. B* **33**, 8360 (1986).

[14] C. Y. Chao and S. L. Chuang, *Phys. Rev. B* **43**, 7027 (1991).

[15] D. Z.-Y. Ting, E. T. Yu, and T. C. McGill, *Phys. Rev. B* **45**, 3576 (1992).

[16] D. Z.-Y. Ting, E. T. Yu, and T. C. McGill, *Phys. Rev. B* **45**, 3583 (1992).

[17] D. A. Collins, D. Z.-Y. Ting, E. T. Yu, D. H. Chow, J. R. Söderström, and T. C. McGill, *J. Crystal Growth* **111**, 664 (1991).

[18] E. O. Kane, *Tunneling Phenomena in Solids*, edited by E. Burstein and S. Lundqvist, (Plenum Press, New York, 1969), p. 1.

[19] G. Y. Wu, K.-M. Hung, and C.-J. Chen, *Phys. Rev. B* **46**, 1521 (1992).

[20] S. Brand and D. T. Hughes, *Semicond. Sci. Technol.* **2**, 607(1987).

[21] D. Y. K. Ko and J. C. Inkson, *Phys. Rev. B* **38**, 9945 (1988).

[22] T. B. Boykin, J. P. A. van der Wagt, and J. S. Harris, *Phys. Rev. B* **43**, 4777 (1991).

[23] W. R. Frensley, *Rev. Mod. Phys.* **62**, 745 (1990).

[24] C. S. Lent and D. J. Kirkner, *J. Appl. Phys.* **67**, 6353 (1990).

[25] Y. C. Chang, *Phys. Rev. B* **37**, 8215 (1988).

[26] E. O. Kane, *Semiconductors and Semimetals*, edited by R. K. Willardson and A. C. Beer (Academic, New York, 1966) Vol. 1, p. 75.

[27] J. C. Slater and G. F. Koster, *Phys. Rev.* **94**, 1498 (1954).

[28] D. Z.-Y. Ting and T. C. McGill, *Phys. Rev. B* **47**, 7281 (1993).

[29] *Molecular Beam Epitaxy and Heterostructures*, proceedings of the NATO Advanced Study Institute on Molecular Beam Epitaxy (MBE) and Heterostructures, Erice, Italy, edited by L. L. Chang and K. Ploog (Martinus Nijhoff, Dordrecht, 1985).

[30] R. K. Hayden *et al.*, *Phys. Rev. Lett.* **66**, 1749 (1991).

[31] J. P. Eisenstein, T. J. Gramila, L. N. Pfeiffer, and K. W. West, *Phys. Rev. B* **44**, 6511 (1991).

[32] U. Gennser *et al.*, *Phys. Rev. Lett.* **67**, 3828 (1991).

[33] G. C. Osbourn, *Phys. Rev. B*, **27**, 5126(1983).

[34] Y. X. Liu, D. Z.-Y. Ting, and T. C. McGill, to be published in *Phys. Rev. B* (1995).

[35] J. M. Luttinger and W. Kohn, *Phys. Rev.* **97**, 869 (1955).

[36] W. H. Press, B. P. Flannery, S. A. Teukolsky, and W. T. Vetterling, *Numerical Recipes: The Art of Scientific Computing* (Cambridge University Press, Cambridge, 1986), pp.578-614.

[37] J. R. Söderström, D. H. Chow, and T. C. McGill, *Appl. Phys. Lett.* **55**, 1094 (1989).

[38] L. F. Luo, R. Beresford, and W. I. Wang, *Appl. Phys. Lett.* **55**, 2023 (1989).

[39] R. Beresford, L. F. Luo, and W. I. Wang, *Appl. Phys. Lett.* **56**, 551 (1990); *Appl. Phys. Lett.* **56**, 952 (1990).

[40] K. Taira, I. Hase, and K. Kawai, *Electron. Lett.* **25**, 1708 (1989).

[41] D. A. Collins, E. T. Yu, Y. Rajakarunanayake, J. R. Söderström, D. H. Chow, D. Z.-Y. Ting, and T. C. McGill, *Appl. Phys. Lett.* **57**, 683 (1990).

[42] L. Yang, J. F. Chen, and A. Y. Cho, *J. Appl. Phys.* **68**, 2997 (1990)

[43] R. R. Marquardt, Y. X. Liu,D. Z.-Y. Ting, D. A. Collins, and T. C. McGill, to be published in *Phys. Rev. B.*

[44] E. E. Mendez, W. I. Wang, B. Ricco, and L. Esaki, *Appl. Phys. Lett.* **47**, 415(1985).

[45] E. T. Yu, M. K. Jackson, and T. C. McGill, *Appl. Phys. Lett.* **55**, 744 (1989).

[46] D. L. Smith, C. Mailhiot, *J. Appl. Phys.* **62**, 2545 (1987).

[47] R. H. Miles, D. H. Chow, J. N. Schulman, and T. C. McGill, *Appl. Phys. Lett.* **57**, 801 (1990).

[48] J.O. McCaldin, *J. Vac. Sci. Technol. A* **8**, 1188 (1990).

[49] K. Akimoto, T. Miyajima and Y. Mori, *Jpn. J. Appl. Phys.* **28**, L528 (1989).

[50] M.A. Haase, J. Qiu, J.M. DePuydt and H. Cheng, *Appl. Phys. Lett.* **59**, 1272 (1991).

[51] H. Jeon, J. Ding, A. V. Nurmikko, W. Xie, M. Kobayashi, and R. L. Gunshor, *Appl. Phys. Lett.* **60**, 892(1992).

[52] Y.Lansari, J. Ren, B. Sneed, K. A. Bowers, J. W. Cook, and J. F. Schetzina, *Appl. Phys. Lett.* **61**, 2552(1992).

[53] See, for example, S. M. Sze, *Physics of Semicondutor Devices*, 2nd edition, chapter 5, (John Wiley & Sons, New York, 1981).

[54] W. D. Baker and A. G. Milnes, *J. Appl. Phys.* **43**, 5152 (1972).

[55] A. K. Wahi, K. Miyano, G. P. Carey, T. T. Chiang, I. Lindau, and W. E. Spicer, *J. Vac. Sci. Technol. A* **8**, 1926 (1990).

[56] W.J. Boudville and T.C. McGill, *J. Vac. Sci. Technol. B* **3**, 1192 (1985).

[57] F.A. Kroger, *J. Phys. Chem. Solid* **26**, 1717 (1965).

[58] G. Mandal, *Phys. Rev.* **134**, A1073 (1964).

[59] E.M. Pell, *J. Appl. Phys.* **31**, 291 (1960).

[60] J.W. Mayer, *J. Appl. Phys.* **33**, 2894(1962).

[61] T. Zundel and J. Weber, *Phys. Rev. B* **39**, 13549 (1989).

[62] S.J. Pearton and J. Lopata, *Appl. Phys. Lett.* **59**, 2841(1991).

[63] M. C. Phillips, J. F. Swenberg, Y. X. Liu, M. W. Wang, J. O. McCaldin and T. C. McGill, *J. Cryst. Growth* **117**, 1050 (1992).

[64] A. C. Gossard, *Treatise on Material Science and Technology*, edited by K. T. Tu and R. Rosenberg(Academic, New York, 1982), Vol. 24.

[65] A. Sommerfeld, *Wave Mechanics* (E.P. Dutton, New York, 1930), Chapter 1.

[66] R. L. Greene, K. K. Bajaj, and D. E. Phelps, *Phys. Rev. B* **29**, 1807(1984).

[67] G. Bastard, E. E. Mendez, L. L. Chang, and L. Esaki, *Phys. Rev. B* **26**, 1974(1982).

[68] G. Duggan and H. I. Ralph, *Phys. Rev. B* **35**, 4125(1987).

[69] I. Suemune, and L. A. Coldren, *IEEE J. Quantum Electron.* **24**, 1778 (1988).

[70] G. W. Bryant, *Phys. Rev. B* **37**, 8763(1988).

[71] J.-L. Zhu, J.-J. Xiong, B.-L Gu, *Phys. Rev. B* **41**, 6001(1990).

[72] Y. Rajakarunanayake, M. C. Phillips, J. O. McCaldin, D. H. Chow, D. A. Collins, and T. C. McGill, *Proc. of the SPIE.* Vo l. **1285**, 142(1990).

[73] J. O. McCaldin, T. C. McGill and C.A. Mead, *Phys. Rev. Lett.* **36**, 56(1976).

[74] Y. X. Liu, Y. Rajakarunanayake, and T. C. McGill, *J. Cryst. Growth* **117**, 742(1992).

[75] W. R. Heller and A. Marcus, *Phys. Rev.* **84**, 809 (1951).

[76] A. S. Davydov, *Theory of Molecular Excitons*, New York-London 1971.

[77] R. J. Elliott, *Phys. Rev.* **108**, 1384 (1957).

[78] A. Baldereschi and N. O. Lipari, *Phys. Rev. B* **3**, 439(1971).

[79] Y. X. Liu, S. K. Kirby, and T. C. McGill, unpublished.

Chapter 2

Multiband k·p Treatment of Quantum Tunneling and Electronic Band Structures in Semiconductor Heterostructures

2.1 Introduction

2.1.1 Background

The proposal and subsequent experimental demonstration of resonant tunneling in semiconductor heterostructures by Tsu and Esaki[1] in 1973 initiated the development of an entire field of research on resonant tunneling devices. A key feature of interest in tunnel structures is the negative differential resistance (NDR) in the current-voltage characteristic. The NDR behavior can be used in a number of applications, with considerable success having been achieved for high-frequency oscillators[2, 3]. Much of the early study on resonant tunneling devices has been focused on intraband tunneling structures based on GaAs/GaAlAs material sys-

tem. More recently, interband tunnel structures involving transport and coupling between conduction-band electron and valence-band hole states based on InAs/GaSb/AlSb systems have been explored[4, 5, 6, 7]. They exhibited very high peak current densities or large peak-to-valley current ratio, making them extremely attractive for use in high-frequency oscillators[3] and neural network circuits[8, 9].

The simulation of electrical characteristics of tunnel structures consists of three major components. First, electrostatic band bending of the device structure, corresponding to the given doping profile and applied bias is calculated. Next, the computed band profiles are used to calculate transmission coefficients of incident electrons in the device structures. Finally, current density is computed from the transmission coefficients by integrating over the incident electron distribution. This simulation scheme does not take into account various scattering processes, nor does it require self-consistency treatment between the band profile and the wave functions of the transmitting electron states.

The central issue in quantum tunneling simulation is to compute the transmission coefficient, given the device structures, energy and momentum of incident electrons. While simple one-band model can explain the qualitative behavior of electron tunneling in GaAs/AlAs double-barrier resonant tunneling structures(DBRT)[1], multiband band-structure models are required to understand and simulate InAs/GaSb/AlSb based interband tunnel devices[10, 11]. The existing techniques for quantum tunneling calculations, such as transfer-matrix method[14] and multiband quantum transmitting boundary method based on tight-binding model[11], have either numerical instability problem or are inconvenient to include magnetic field and strain effects. The technique we present in this chapter is based on multiband $\mathbf{k}\cdot\mathbf{p}$ model, making it easy to include magnetic field and strain effects. In addition, it is efficient, numerically stable, and simple to implement. With appropriate modifications of boundary conditions, the calculations of electronic band structures for quantum confinement and superlattice states can be carried out using the same technique.

2.1.2 Outline of Chapter

In this chapter, we present an efficient and numerically stable method for treating quantum transport and electronic band structures in semiconductor heterostructures using multiband **k·p** theory. We begin in section 2.2 with a brief review of three existing methods in quantum transport studies: transfer-matrix method, scattering-matrix method, and the tight-binding method. To keep it illustrative and intuitive, we will use simple one-band structure model to describe these methods and point out their difficulties and limitations in certain applications.

We then present the general theoretical framework of our multiband **k·p** method in section 2.3. First a general formulation of multiband **k·p** Hamiltonian is given in section 2.3.1. Then we discuss how the **k·p** formulation can be extended to include the strain effects in section 2.3.2. The numerical technique employed to solve Schrödinger's equation – finite difference method, is described in section 2.3.3, followed by discussions of heterostructure interface treatment and current density operator representation in the framework of multiband **k·p** theory in section 2.3.3.

In section 2.4, we present a detail account of the technique for quantum tunneling study in heterostructures. A detailed account of **k·p** version of the Multiband Quantum Transmitting Boundary Method (MQTBM) is presented in section 2.4.1. Sections 2.4.2 discusses the calculations of transmission coefficients. In the end, a brief comparison of our method with other existing methods is given in section 2.4.3.

In section 2.5, we demonstrate our technique in prototypical *p*-type GaAs/AlAs double barrier tunnel structure using the well-known 4-band Luttinger-Kohn Hamiltonian, and examine the hole-mixing effect. Applications of this new technique to magnetotunneling study in InAs/GaSb/AlSb based interband tunnel structures are presented in chapter 3.

In section 2.6.1 and 2.6.2, we apply the finite-difference method to the calculations of electronic band structures in quantum confinement states and superlattices

by implementing appropriate boundary conditions. Calculations of band structures in unstrained InAs/GaSb superlattice and strained $InAs/Ga_{1-x}In_xSb$ superlattices are presented. Finally, a summary of the chapter is given in section 2.7.

2.2 Review of Existing Methods

In this section, we will review three well-known techniques that have been developed for the quantum tunneling calculation: transfer-matrix method, scattering-matrix method, and the tight-binding method. For illustrative purposes and without losing the important essence, we will describe these methods using simple one-band model.

In simple one-band model with parabolic band structure of effective mass m^*, Schrödinger's equation in Effective Mass Approximation (EMA) is

$$-\frac{\hbar^2}{2}\frac{d}{dx}\left(\frac{1}{m^*}\frac{d\psi(x)}{dx}\right)+V(x)\psi(x)=E\psi(x). \tag{2.1}$$

The probability current for the Hamiltonian in Eq. (2.1) is given by

$$J=\frac{i\hbar}{2}\left[\psi^*\left(\frac{1}{m^*}\frac{d\psi}{dz}\right)-\left(\frac{1}{m^*}\frac{d\psi^*}{dz}\right)\psi\right]. \tag{2.2}$$

At the hetero-interface between two materials, wave-function and current continuity require that ψ and $\frac{1}{m^*}\frac{d\psi}{dx}$ be continuous across the interface. The problems in quantum tunneling, as schematically illustrated in Fig. 2.1, is defined as that we have a known incoming plane-wave state from the left region, no incoming states from the right, and unknown outgoing transmitted and reflected plane-wave states in the right and left regions, respectively. The wave functions on the left and right flat band regions are expressed as

$$\psi_L = Ie^{ik_Lx}+re^{-ik_Lx}, \tag{2.3}$$

$$\psi_R = te^{ik_Rx}, \tag{2.4}$$

where I represents the known incoming plane-wave state from the left region, while t and r describe the transmitted and reflected states. The calculation of

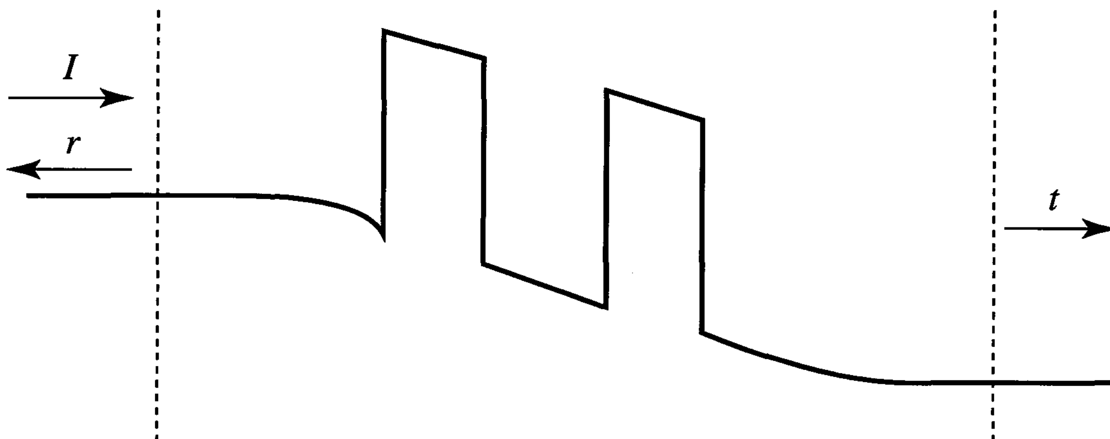

Figure 2.1: The boundary conditions for quantum tunneling in heterostructures are that we have a known incoming plane-wave state I from the left region, no incoming states from the right, and unknown outgoing transmitted and reflected plane-wave states t and r in the right and left regions, respectively.

transmission coefficient is to evaluate the amplitude of transmitted plan wave state t given the incoming state I.

2.2.1 Transfer-Matrix Method

The standard technique for computing transmission coefficients in heterostructures is the transfer-matrix method originally developed by Kane[12]. As schematically shown in Fig. 2.2, To calculate the transmission coefficient across a device structure with an arbitrary energy band profile, the continuous band profile is approximated by a set of piecewise-constant profile across the entire device region. The two boundaries at the ends are extended to flat band regions where the electron states are plane-wave like

$$\psi_1 = Ie^{ik_L x} + re^{-ik_L x}, \tag{2.5}$$

$$\psi_N = te^{ik_R x}, \tag{2.6}$$

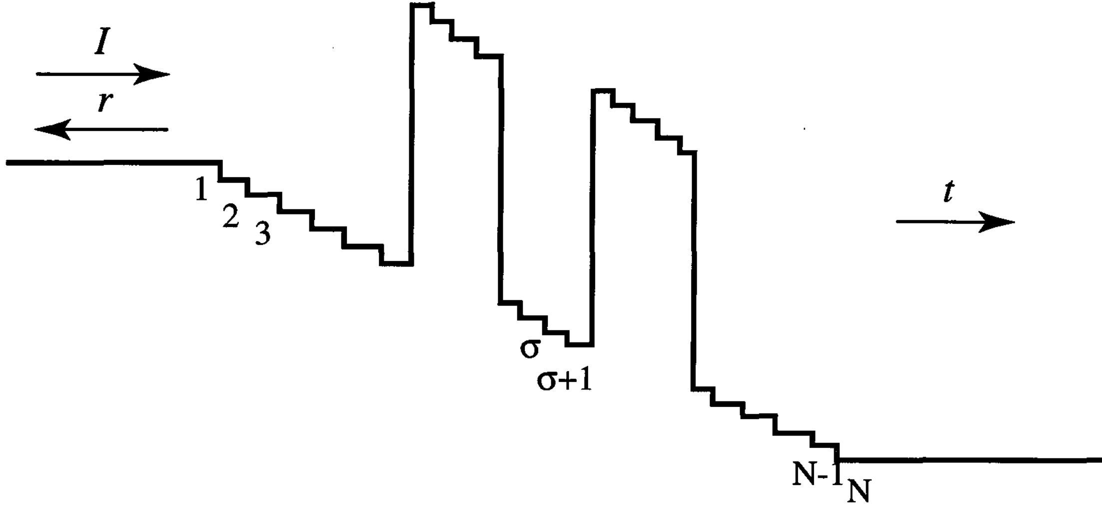

Figure 2.2: In transfer-matrix method, the continuous band profile of device structure is approximated by a piecewise-constant profile with constant band edges in the intervals between discretized lattice points. The two boundaries at the ends are extended to flat band regions where the electron states are plane-wave like.

The general solutions of wave functions to Schrödinger's Eq. (2.1) at each piecewise-constant potential consist of both the forward and backward plane-wave states in the following general form

$$\psi_\sigma = A_\sigma e^{ik_\sigma x} + B_\sigma e^{-ik_\sigma x} \tag{2.7}$$

$$\psi_{\sigma+1} = A_{\sigma+1} e^{ik_{\sigma+1} x} + B_{\sigma+1} e^{-ik_{\sigma+1} x}\,. \tag{2.8}$$

The requirements that ψ and $\dfrac{1}{m^*}\dfrac{d\psi}{dx}$ be continuous across the device structure lead to the following form of the transfer matrix $\mathbf{T}_\sigma$, which relates the wave function in one thin layer $\sigma+1$ to the wave function in the previous layer σ:

$$\begin{aligned} \begin{bmatrix} A_{\sigma+1} \\ B_{\sigma+1} \end{bmatrix} &= \begin{bmatrix} \frac{1+\alpha_\sigma}{2} e^{i(k_\sigma - k_{\sigma+1})x_\sigma} & \frac{1-\alpha_\sigma}{2} e^{-i(k_\sigma + k_{\sigma+1})x_\sigma} \\ \frac{1-\alpha_\sigma}{2} e^{i(k_\sigma + k_{\sigma+1})x_\sigma} & \frac{1+\alpha_\sigma}{2} e^{-i(k_\sigma - k_{\sigma+1})x_\sigma} \end{bmatrix} \begin{bmatrix} A_\sigma \\ B_\sigma \end{bmatrix} \\ &= \mathbf{T}^\sigma \begin{bmatrix} A_\sigma \\ B_\sigma \end{bmatrix}, \end{aligned} \tag{2.9}$$

where $\alpha_\sigma = \frac{m^\star_{\sigma+1}}{m^\star_\sigma}\frac{k_\sigma}{k_{\sigma+1}}$ and $k_\sigma = \sqrt{2m^\star_\sigma(E-V_\sigma)/\hbar^2}$. Applying the transfer matrix equation (2.9) repeatedly to the entire device structure, we obtain the transfer matrix equation that relate the wave functions at left and right regions

$$\begin{aligned}\begin{bmatrix} t \\ 0 \end{bmatrix} &= \mathbf{T}^N\mathbf{T}^{N-1}\cdots\mathbf{T}^2\mathbf{T}^1\begin{bmatrix} I \\ r \end{bmatrix} \\ &= \mathbf{T}\begin{bmatrix} I \\ r \end{bmatrix}. \end{aligned} \tag{2.10}$$

The amplitude of the transmitted wave t is then given by

$$t = \frac{\mathbf{T}_{11}\mathbf{T}_{22} - |\mathbf{T}_{12}|^2}{\mathbf{T}_{22}} I. \tag{2.11}$$

The transmission coefficient T is simply the ratio of the transmitted to the incident currents. From Eq. (2.2) we therefore obtain

$$\begin{aligned} T &= \frac{m_L k_L}{m_R k_R}|t|^2 \\ &= \frac{m_L k_L}{m_R k_R}\left|\frac{\mathbf{T}_{11}\mathbf{T}_{22} - |\mathbf{T}_{12}|^2}{\mathbf{T}_{22}} I\right|^2. \end{aligned} \tag{2.12}$$

Historically, transfer-matrix method has been used most widely to study heterojunction tunneling devices. Tsu and Esaki employed the method in their study of the first resonant tunneling device, n-type GaAs/AlAs double barrier heterostructure in 1973[1]. Electron tunneling in the conduction band of heterostructures can be satisfactorily described within the framework of one-band transfer-matrix method described above. Later, it has been applied to two-band[10] and four-band band structure models to take into account the valence band structure in the study of p-type GaAs/AlAs double barrier heterostructures[13, 14, 15, 16, 17], and InAs/GaSb/AlSb resonant interband tunnel devices[7, 10, 11]. However, transfer-matrix method has encountered serious numerical instability problems when used in conjunction with multiband model for device structures larger then a few tens of Å. The origin of the failure is due to the loss of exponentially decaying wave

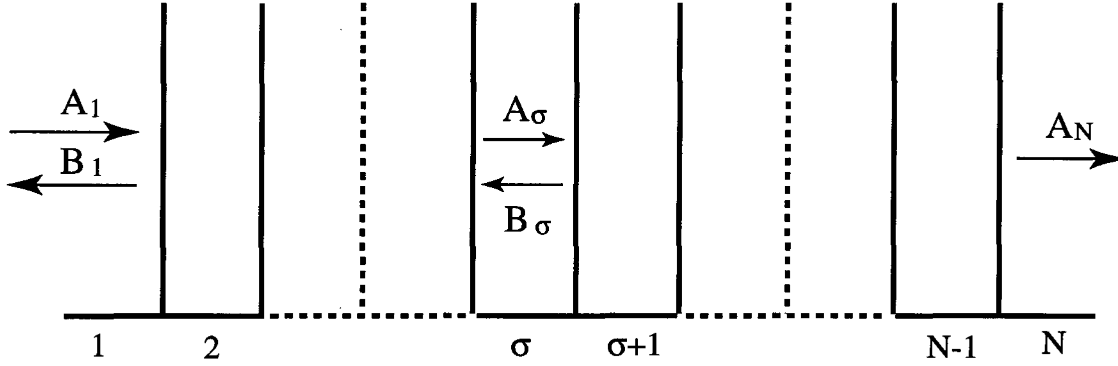

Figure 2.3: Schematic diagram of tunneling in S-matrix method, where the states are categorized as incoming states A_1, B_σ, and outgoing states B_1, A_σ. The relationship between them is represented by a **S** matrix.

functions in the presence of exponentially growing wave functions in a barrier region. This numerical instability problem was addressed by the S-matrix method proposed by Ko and Inkson[18].

2.2.2 Scattering Matrix Method

Unlike the transfer-matrix method, which groups the incoming and outgoing states together in a given layer region, and relates them to the states in next layer through a transfer matrix $\mathbf{T}$, the S-matrix method proposed by Ko and Inkson[18], as shown in Fig. 2.3, separates the states into incoming states A_1, B_σ, and outgoing states B_1, A_σ, and couples them explicitly by a **S** matrix

$$\begin{bmatrix} A_\sigma \\ B_1 \end{bmatrix} = \mathbf{S}^\sigma \begin{bmatrix} A_1 \\ B_\sigma \end{bmatrix}. \tag{2.13}$$

Together with the transfer matrix Eq. (2.9), we can derive the **S** matrix successively starting with unix matrix for $\mathbf{S}^1$ with the following relationship

$$\begin{bmatrix} A_{\sigma+1} \\ B_1 \end{bmatrix} = \mathbf{S}^{\sigma+1} \begin{bmatrix} A_1 \\ B_{\sigma+1} \end{bmatrix}$$

$$= \begin{bmatrix} 0 & (T_{11}^{\sigma} - S_{12}^{\sigma}T_{21}^{\sigma})^{-1} \\ 1 & S_{22}^{\sigma}T_{21}^{\sigma}(T_{11}^{\sigma} - S_{12}^{\sigma}T_{21}^{\sigma})^{-1} \end{bmatrix}$$
$$\cdot \begin{bmatrix} S_{21}^{\sigma} & S_{22}^{\sigma}T_{22}^{\sigma} \\ S_{11}^{\sigma} & S_{12}^{\sigma}T_{22}^{\sigma} - T_{12}^{\sigma} \end{bmatrix} \begin{bmatrix} A_1 \\ B_{\sigma+1} \end{bmatrix} . \quad (2.14)$$

The coefficients of transmitted and reflected states, t and r, can then be related to the incoming state I by

$$\begin{bmatrix} t \\ r \end{bmatrix} = \mathbf{S}^N \begin{bmatrix} I \\ 0 \end{bmatrix} . \quad (2.15)$$

The stability and accuracy of the S-matrix method is derived from the separation of the forward and backward states and by doing so, the less localized and the propagating states dominate numerically, the physics of the tunneling process is more faithfully described. The iterative procedure in Eq. (2.14), however, is not as easy to use as the transfer-matrix method Eq. (2.10), which simply involves the product of matrices. The gain in stability is at the cost of computational efficiency.

2.2.3 Tight-binding Method

A major step in developing an efficient and stable numerical method for quantum tunneling computation is made by Ting *et al.* [11]. The multiband tight-binding approach they developed is a generalization of Frensley's [19] one-band effective mass approximation implementation of the Quantum Transmitting Boundary Method (QTBM), originally developed by Lent and Kirkner [20] for treating electron waveguide using a finite-element approach. The key point in this technique is the formulation of boundary conditions.

In one-dimensional case, the wave function in tight-binding method is expressed in terms of local tight-binding orbitals $|\sigma\rangle$

$$|\psi\rangle = \sum_{\sigma} C_{\sigma}|\sigma\rangle . \quad (2.16)$$

The Schrödinger's equation $(H-E)|\psi\rangle = 0$ in the local orbital basis is represented by a set of linear equations on the tight-binding coefficients

$$H_{\sigma,\sigma-1}C_{\sigma-1} + (H_{\sigma,\sigma} - E)C_{\sigma} + H_{\sigma,\sigma+1}C_{\sigma+1} = 0, \tag{2.17}$$

where only the nearest neighbor coupling are considered and the hopping matrix elements are given by

$$H_{\sigma,\sigma'} = \langle\sigma|H|\sigma'\rangle\ . \tag{2.18}$$

The two boundaries at $\sigma = 1$ and $\sigma = N$ are extended to flat band regions where electron states are of Bloch plane-wave form satisfying $\psi(x+a) = e^{ika}\psi(x)$. Therefore, the boundary condition for tunneling at the left end given by Eq. (2.5) leads to the following equations

$$C_1 = I + r, \tag{2.19}$$

$$C_2 = Ie^{ik_La} + re^{-ik_La}. \tag{2.20}$$

Eliminate r, we obtain

$$C_1 - e^{ik_La}C_2 = I(1 - e^{i2k_La}). \tag{2.21}$$

Similarly apply the technique to the boundary condition at the right region Eq.(2.6), we have

$$C_{N-1}e^{ik_Ra} - C_N = 0. \tag{2.22}$$

The above equations, together with Eq.(2.17), constitute a system of N linear equations which can be written in the matrix form as

$$\begin{bmatrix} 1 & -e^{ik_{\rm L}a} & 0 & \cdots & \cdots & \cdots & 0 \\ H_{2,1} & H_{2,2} & H_{2,3} & 0 & \cdots & \cdots & 0 \\ 0 & H_{3,2} & H_{3,3} & H_{3,4} & 0 & \cdots & 0 \\ \vdots & & \ddots & \ddots & \ddots & \vdots & \vdots \\ 0 & & & 0 & H_{N-1,N-2} & H_{N-1,N-1} & H_{N-1,N} \\ 0 & \cdots & \cdots & \cdots & 0 & -e^{ik_{\rm R}a} & 1 \end{bmatrix} \cdot \begin{bmatrix} C_1 \\ C_2 \\ C_3 \\ \vdots \\ C_{N-1} \\ C_N \end{bmatrix}$$

$$= \begin{bmatrix} I(1-e^{i2k_{\mathrm{R}}a}) \\ 0 \\ 0 \\ \vdots \\ 0 \\ 0 \end{bmatrix}. \tag{2.23}$$

The boundary conditions of incoming and outgoing plane-wave states in the quantum tunneling problems are represented by the boundary and inhomogeneous terms in this system of linear equations.

Equation (2.23) can be solved readily using standard numerical mathematical algorithms. Having obtained the coefficients of envelope function C_σ, it follows from Eq.(2.6) that the coefficient of transmitted plane-wave states t is given by

$$t = e^{-ik_R(N-1)a} C_N. \tag{2.24}$$

This method has been demonstrated to be numerically stable for device structures wide than 2000Å and as efficient as the transfer-matrix method. The implementation of this method is also very simple.

Despite the great success of this method in numerous applications, the tight-binding model is inconvenient when apply to systems involving external magnetic field and strain effects. It is known that **k**·**p** method is naturally suited for dealing problems involving magnetic field and strain. Our goal in the next two sections is to develop a similar method to QTBM based on the **k**·**p** theory[21].

2.3 Multiband k·p Method

2.3.1 k·p Hamiltonian

The basic results of the effective mass theory are that if the external potential V varies slowly over the unit cell, the effect of the periodic field of crystal lattice can

be replaced by a set of parameters H_{ij}, which are determined by the unperturbed bulk band structure. The solutions to the original Schrödinger's equation can be obtained by solving the following coupled effective mass differential equations[22]

$$i\hbar \frac{\partial F_i}{\partial t} = \sum_{j=1}^{M} \left[H_{ij}(-i\nabla) + V(\mathbf{r})\delta_{ij} \right] F_j, \tag{2.25}$$

where the envelope functions F_i is related to the wave function by

$$\psi = \sum_{j=1}^{M} F_j u_{j0}, \tag{2.26}$$

where M is the number of the bands involved in the model, u_{i0} are the Bloch basis at the Brillouin zone center with lattice periodicity, and the form of matrix elements $H_{ij}(\mathbf{k})$ are determined by the $\mathbf{k}\cdot\mathbf{p}$ method.[23] The bulk band matrix element H_{ij}, in the second order $\mathbf{k}\cdot\mathbf{p}$ method, can be generally written as

$$H_{ij} = D_{ij}^{(2)\alpha\beta} k_\alpha k_\beta + D_{ij}^{(1)\alpha} k_\alpha + D_{ij}^{(0)} \tag{2.27}$$

where indices α and β are summed over x, y, z.

The well-known 4×4 Luttinger-Kohn Hamiltonian describing the top of valence band Γ_8 states is of the form[24]

$$\mathbf{H}(\mathbf{k}) = \begin{bmatrix} P+Q & -S & R & 0 \\ -S^* & P-Q & 0 & R \\ R^* & 0 & P-Q & S \\ 0 & R^* & S^* & P+Q \end{bmatrix}, \tag{2.28}$$

with

$$P(\mathbf{k}) = \frac{\hbar^2}{2m}\gamma_1 k^2 - E_V, \tag{2.29}$$

$$Q(\mathbf{k}) = \frac{\hbar^2}{2m}\gamma_2(k_x^2 + k_y^2 - 2k_z^2), \tag{2.30}$$

$$S(\mathbf{k}) = \frac{\hbar^2}{2m}2\sqrt{3}\gamma_3(k_x - ik_y)k_z, \tag{2.31}$$

$$R(\mathbf{k}) = \frac{\hbar^2}{2m}\sqrt{3}\left[-\gamma_2(k_x^2 - k_y^2) + 2i\gamma_3 k_x k_y\right], \tag{2.32}$$

where γ_1, γ_2 and γ_3 are Luttinger parameters. The linear terms in $\mathbf{k}$ usually appear when the model includes explicitly the interaction between conduction band and valence bands of the system. In appendix A.1, we also give the expressions for $\mathbf{k}\cdot\mathbf{p}$ matrix elements in 8×8 band structure models which include explicitly the interaction between conduction-band and valence-band, and will be used for the interband tunneling study in chapter 3.

The problems we consider are one-dimensional in which the system varies only along the growth direction(x axis), and is translational invariant in the lateral directions. We can rewrite the the Hamiltonian matrix element Eq. (2.27) as second order polynomial in k_x,

$$H_{ij} = H_{ij}^{(2)} k_x^2 + H_{ij}^{(1)}(\mathbf{k}_{\|}) k_x + H_{ij}^{(0)}(\mathbf{k}_{\|}), \tag{2.33}$$

with $\mathbf{k}_{\|} = k_y \hat{y} + k_z \hat{z}$ being a good quantum number. In short, we can write

$$\mathbf{H}(\mathbf{k}) = \mathbf{H}^{(2)} k_x^2 + \mathbf{H}^{(1)}(\mathbf{k}_{\|}) k_x + \mathbf{H}^{(0)}(\mathbf{k}_{\|}) \tag{2.34}$$

where $\mathbf{H}^{(n)}$ are $M \times M$ matrices. For top of valence band 4×4 Hamiltonian given in Eq.(2.28), we have

$$\mathbf{H}^{(2)} = \frac{\hbar^2}{2m} \begin{bmatrix} \gamma_1+\gamma_2 & 0 & -\sqrt{3}\gamma_2 & 0 \\ 0 & \gamma_1-\gamma_2 & 0 & -\sqrt{3}\gamma_2 \\ 0 & -\sqrt{3}\gamma_2 & \gamma_1-\gamma_2 & 0 \\ 0 & -\sqrt{3}\gamma_2 & 0 & \gamma_1+\gamma_2 \end{bmatrix}, \tag{2.35}$$

$$\mathbf{H}^{(1)}(\mathbf{k}_{\|}) = \frac{\hbar^2}{2m} \begin{bmatrix} 0 & -2\sqrt{3}\gamma_3 k_z & i2\sqrt{3}\gamma_3 k_y & 0 \\ -2\sqrt{3}\gamma_3 k_z & 0 & 0 & i2\sqrt{3}\gamma_3 k_y \\ -i2\sqrt{3}\gamma_3 k_y & 0 & 0 & 2\sqrt{3}\gamma_3 k_z \\ 0 & -i2\sqrt{3}\gamma_3 k_y & 2\sqrt{3}\gamma_3 k_z & 0 \end{bmatrix}, \tag{2.36}$$

$$\mathbf{H}^{(0)}(\mathbf{k}_{\|}) = \frac{\hbar^2}{2m} \begin{bmatrix} (\gamma_1+\gamma_2)k_y^2 + (\gamma_1-2\gamma_2)k_z^2 & i2\sqrt{3}\gamma_3 k_y k_z \\ -i2\sqrt{3}\gamma_3 k_y k_z & (\gamma_1-\gamma_2)k_y^2 + (\gamma_1+2\gamma_2)k_z^2 \\ \sqrt{3}\gamma_2 k_y^2 & 0 \\ 0 & \sqrt{3}\gamma_2 k_y^2 \end{bmatrix}$$

$$
\begin{array}{cc}
\sqrt{3}\gamma_2 k_y^2 & 0 \\
0 & \sqrt{3}\gamma_2 k_y^2 \\
(\gamma_1-\gamma_2)k_y^2+(\gamma_1+2\gamma_2)k_z^2 & -i2\sqrt{3}\gamma_3 k_y k_z \\
i2\sqrt{3}\gamma_3 k_y k_z & (\gamma_1+\gamma_2)k_y^2+(\gamma_1-2\gamma_2)k_z^2
\end{array}
\Bigg] . \quad (2.37)
$$

Given the expression for $\mathbf{k}\cdot\mathbf{p}$ Hamiltonian, the construction of matrices $\mathbf{H}^{(2)}$, $\mathbf{H}^{(1)}$, and $\mathbf{H}^{(0)}$ is straightforward.

2.3.2 Strain Effect

One of the great advantages of $\mathbf{k}\cdot\mathbf{p}$ theory is that it can be easily extended to include various external fields. The strain effect exists in various lattice-mismatched heterostructure systems. It has been widely employed as an additional degree of freedom in the exploration of band structures engineering[25]. The presence of strain modifies the crystal potential and changes crystal symmetry. The effect of strain on the band structures can be described very easily in $\mathbf{k}\cdot\mathbf{p}$ theory.

Treating strain as a perturbation to the original crystal potential, Bir and Pikus [26] have shown that strain adds a few matrix elements to the $\mathbf{k}\cdot\mathbf{p}$ Hamiltonian through the use of deformation potentials. For top of valence band Γ_8 states, because strain in a cubic crystal can be described by a strain tensor ϵ_{ij} having the same symmetry as the quadratic tensor $k_i k_j$, the added constant term to Hamiltonian in Eq. (2.34) due to strain can be written as

$$
\mathbf{H}(\epsilon) = \begin{bmatrix}
P_\epsilon + Q_\epsilon & -S_\epsilon & R_\epsilon & 0 \\
-S_\epsilon^* & P_\epsilon - Q_\epsilon & 0 & R_\epsilon \\
R_\epsilon^* & 0 & P_\epsilon - Q_\epsilon & S_\epsilon \\
0 & R_\epsilon^* & S_\epsilon^* & P_\epsilon + Q_\epsilon
\end{bmatrix}, \quad (2.38)
$$

with

$$
P_\epsilon = a_v(e_{xx} + e_{yy} + e_{zz}), \quad (2.39)
$$

$$
Q_\epsilon = b[e_{zz} - \frac{1}{2}(e_{xx} + e_{yy})], \quad (2.40)
$$

$$S_\epsilon = -d(e_{xz} - ie_{yz})\,, \tag{2.41}$$

$$R_\epsilon = \frac{\sqrt{3}}{2}b(e_{xx} - e_{yy}) - ide_{xy}\,, \tag{2.42}$$

where a is referred to as the hydrostatic deformation potential which determines the shift due to isotropic strain. b is referred to as the uniaxial deformation strain which determines the heavy-hole and light-hole band splitting for [001] strain. The strain induced extra term $\mathbf{H}(\epsilon)$ just adds constant term to $\mathbf{H}^{(0)}$ in Eq. (2.37).

For band models involving strong interactions between the conduction band and valence band, strain also adds a linear term in k to the matrix elements between conduction-band and valence-band in addition to constant terms. Therefore, only $\mathbf{H}^{(1)}$ and $\mathbf{H}^{(0)}$ need to be modified in the presence of strain. An explicit representation of strain Hamiltonian in 8×8 band structures is given in appendix A.2.

2.3.3 Discretization of Schrödinger's Equation

Replacing k_x by the operator $\frac{1}{i}\frac{\partial}{\partial x}$ in Eq. (2.34), the effective mass Schrödinger's equation $HF = EF$ is represented by

$$\left(-\mathbf{H}^{(2)}\frac{\partial^2}{\partial x^2} - i\mathbf{H}^{(1)}\frac{\partial}{\partial x} + \mathbf{H}^{(0)} + V(x)\right)\mathbf{F} = E\mathbf{F}\,, \tag{2.43}$$

where the envelope function $\mathbf{F}$ is a vector of length M.

To solve Eq. (2.43) numerically, we employ finite-difference method. As schematically illustrated in Fig. 2.4, the entire device region is discretized into N lattice points $\{x_\sigma\}$, $\sigma = 1, 2, \ldots, N$, typically with equal spacing a. If we choose a to be on the order of lattice spacing, within the framework of effective mass theory, the derivatives of envelope function can then be well approximated by finite differences

$$\frac{\partial \mathbf{F}}{\partial x}\Big|_{x_\sigma} \Longrightarrow \frac{\mathbf{F}_{\sigma+1} - \mathbf{F}_\sigma}{a}\,, \tag{2.44}$$

$$\frac{\partial^2 \mathbf{F}}{\partial x^2}\Big|_{x_\sigma} \Longrightarrow \frac{\mathbf{F}_{\sigma+1} + \mathbf{F}_{\sigma-1} - 2\mathbf{F}_\sigma}{a^2}. \tag{2.45}$$

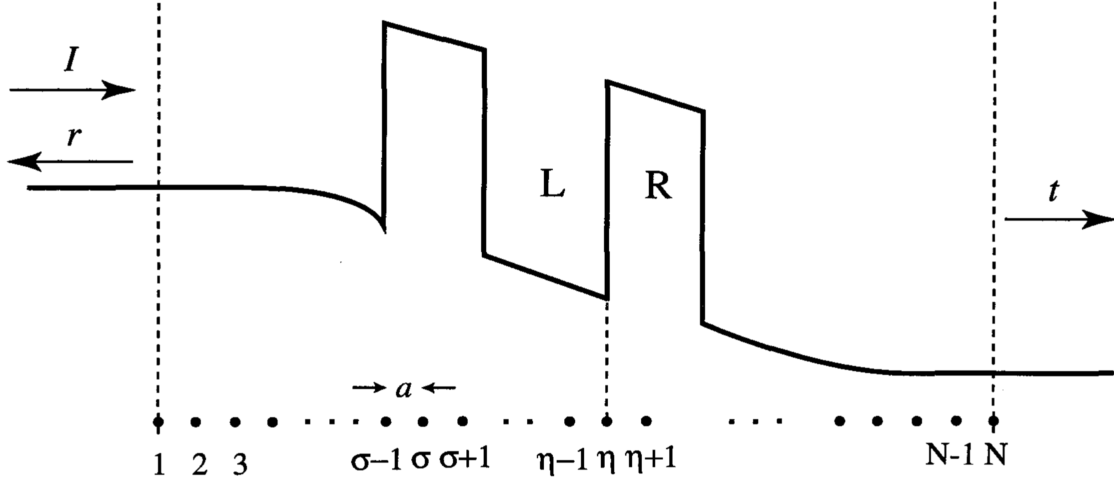

Figure 2.4: The entire device region is discretized in to N lattice points. The two boundaries at the ends are extended to flat band regions where the electron states are plane-wave like.

Within each heterojunction region, apply the finite difference approximations of Eq.(2.44) and Eq. (2.45) at each discretized lattice point σ, the M coupled differential equations (2.43) are then transformed into M linear finite difference equations

$$\mathbf{H}_{\sigma,\sigma-1}\mathbf{F}_{\sigma-1} + \mathbf{H}_{\sigma,\sigma}\mathbf{F}_{\sigma} + \mathbf{H}_{\sigma,\sigma+1}\mathbf{F}_{\sigma+1} = 0, \tag{2.46}$$

with

$$\mathbf{H}_{\sigma,\sigma} = \frac{2\mathbf{H}^{(2)}}{a^2} + \mathbf{H}^{(0)} + V_\sigma - E, \tag{2.47}$$

$$\mathbf{H}_{\sigma,\sigma+1} = -\frac{\mathbf{H}^{(2)}}{a^2} - i\frac{\mathbf{H}^{(1)}}{2a}, \tag{2.48}$$

$$\mathbf{H}_{\sigma,\sigma-1} = -\frac{\mathbf{H}^{(2)}}{a^2} + i\frac{\mathbf{H}^{(1)}}{2a}, \tag{2.49}$$

where $\mathbf{H}_{\sigma,\sigma'}$ are $M \times M$ matrices.

Eq.(2.46) has the similar form as the tight-binding formulation Eq. (2.17) with nearest neighbor interaction. This important observation led us to develop a similar method, based on multiband $\mathbf{k}\cdot\mathbf{p}$ theory, to that of the tight-binding

MQTBM approach for treating quantum transport.

2.3.4 Current Density Operator and Treatment of Heterostructure Interface

Effective mass theory assumes that envelope function F_i varies much more slowly compared to the Bloch basis function u_{i0}. Following the treatment of Altarelli[13], the probability density can be approximated by its average over a unit cell,

$$\begin{aligned} \rho &= \psi^*\psi \approx \sum_{i,j} F_i^* F_j \langle u_{i0}|u_{j0}\rangle & (2.50) \\ &= \mathbf{F}^\dagger \mathbf{F}, & (2.51) \end{aligned}$$

using the fact that

$$\langle u_{i0}|u_{j0}\rangle = \delta_{ij}. \tag{2.52}$$

Using the Hamiltonian expression in Eq. (2.34), the time-dependent Schrödinger's equation (2.25) can be written as

$$i\hbar\frac{\partial \mathbf{F}}{\partial t} = \left[\mathbf{H}^{(2)}k_x^2 + \mathbf{H}^{(1)}k_x + \mathbf{H}^{(0)} + V(x)\right]\mathbf{F}. \tag{2.53}$$

Using the properties that $\mathbf{H}^{(i)}$ are Hermitian, we can derive the probability conservation equation

$$i\hbar\frac{\partial \rho}{\partial t} = -\frac{\partial}{\partial x}\left(\mathbf{F}^\dagger\mathbf{H}^{(2)}\frac{\partial \mathbf{F}}{\partial x} - \frac{\partial \mathbf{F}^\dagger}{\partial x}\mathbf{H}^{(2)}\mathbf{F} + i\mathbf{F}^\dagger\mathbf{H}^{(1)}\mathbf{F}\right). \tag{2.54}$$

The current in the $\mathbf{k}\cdot\mathbf{p}$ theory is then given by

$$\begin{aligned} J_x &= \frac{1}{i\hbar}\left(\mathbf{F}^\dagger\mathbf{H}^{(2)}\frac{\partial \mathbf{F}}{\partial x} - \frac{\partial \mathbf{F}^\dagger}{\partial x}\mathbf{H}^{(2)}\mathbf{F} + i\mathbf{F}^\dagger\mathbf{H}^{(1)}\mathbf{F}\right) \\ &= \mathrm{Re}(\mathbf{F}^\dagger\mathbf{J}_x\mathbf{F}), & (2.55) \end{aligned}$$

with

$$\mathbf{J}_x = \frac{1}{\hbar}\left(-2i\mathbf{H}^{(2)}\frac{\partial}{\partial x} + \mathbf{H}^{(1)}\right). \tag{2.56}$$

At the heterojunction interface $\sigma = \eta$, the $\mathbf{k}\cdot\mathbf{p}$ matrix elements for different materials on both sides of the interface have different values. The wave functions

on both sides of the interface are related to each other through the the conditions of the wave function and current continuity. Following the treatment of Altarelli[13], we ignore the differences in the Bloch basis functions u_{i0} for materials across the hetero-interface. Then the condition of wave function continuity results in the continuity of envelope functions

$$\mathbf{F}_L = \mathbf{F}_R. \tag{2.57}$$

The current continuity requires that $\mathbf{J}_x\mathbf{F}$, or

$$-2i\mathbf{H}^{(2)}\frac{\partial \mathbf{F}}{\partial x} + \mathbf{H}^{(1)}\mathbf{F} \tag{2.58}$$

be continuous across the interface, which results in the following linear finite-difference equations when applying finite-difference Eq. (2.44),

$$\mathbf{H}_{\eta,\eta-1}\mathbf{F}_{\eta-1} + \mathbf{H}_{\eta,\eta}\mathbf{F}_{\eta} + \mathbf{H}_{\eta,\eta+1}\mathbf{F}_{\eta+1} = 0\,. \tag{2.59}$$

The $\mathbf{H}$ matrices at the interface η are given by:

$$\mathbf{H}_{\eta,\eta} = \frac{2(\mathbf{H}_R^{(2)} + \mathbf{H}_L^{(2)})}{a^2} - i\frac{\mathbf{H}_R^{(1)} - \mathbf{H}_L^{(1)}}{2a}, \tag{2.60}$$

$$\mathbf{H}_{\eta,\eta+1} = -\frac{2\mathbf{H}_R^{(2)}}{a^2} - i\frac{\mathbf{H}_R^{(1)}}{2a}, \tag{2.61}$$

$$\mathbf{H}_{\eta,\eta-1} = -\frac{2\mathbf{H}_L^{(2)}}{a^2} + i\frac{\mathbf{H}_L^{(1)}}{2a}. \tag{2.62}$$

Eq. (2.46) and Eq. (2.59) are the discretized form of effective mass Schrödinger's Equation. They together constitute a set of $N \times M$ coupled linear equations across the entire heterostructure region. Combined with appropriate treatments of boundary conditions, it can be readily applied to the study of various problems ranging from quantum tunneling in heterostructures to calculations of electronic band structures in superlattices and confined heterostructures. We will address these issues and their applications in the next few sections.

2.4 Quantum Tunneling

2.4.1 Boundary Conditions

We follow the idea of multiband quantum transmission boundary method (MQTBM) [11] in formulating boundary conditions for calculation of transmission coefficients. The basic idea has been illustrated in section 2.2.3 for one-band band structure model. The formulation of boundary conditions in multiband model is however more sophisticated and deserves special attention.

In bulk flat band region, the Bloch plane-wave solutions of wave vector $\mathbf{k}$ can be generally written as

$$\mathbf{F_k} = e^{i\mathbf{k}\cdot\mathbf{r}}\mathbf{C_k} \tag{2.63}$$

where $\mathbf{C_k}$ satisfies that

$$\mathbf{H}(\mathbf{k})\mathbf{C_k} = E\mathbf{C_k}. \tag{2.64}$$

Matrix elements $H_{ij}(\mathbf{k})$ are generally a quadratic polynomial in k_α, so for fixed energy E and in-plane wave-vector $\mathbf{k}_{\|}$, there will be $2M$ complex wave vector solutions $k_{x,j}$ and associated eigenstates $\mathbf{C}_{\mathbf{k}_j}$ in general. The wave function ψ for given energy E is in general a linear combination of these solutions,

$$\mathbf{F}(\mathbf{r}) = e^{i\mathbf{k}_{\|}\cdot\mathbf{r}_{\|}}\sum_{j=1}^{2M} b_i e^{ik_{x,j}x}\mathbf{C}_{\mathbf{k}_j}, \tag{2.65}$$

$$\psi = \mathbf{F}(\mathbf{r})\mathbf{u}_0(\mathbf{r}). \tag{2.66}$$

To find out the $2M$ eigenstates given the energy E and $\mathbf{k}_{\|}$, we rewrite Eq. (2.64) explicitly using Eq. (2.34) as

$$\left[\mathbf{H}^{(2)}k_x^2 + \mathbf{H}^{(1)}(\mathbf{k}_{\|})k_x + \mathbf{H}^{(0)}(\mathbf{k}_{\|}) - E\right]\mathbf{C_k} = 0\,. \tag{2.67}$$

The generalized eigenvalue problem of Eq. (2.67) can be converted into the standard eigenvalue form for k_x[27, 28]

$$\begin{bmatrix} \mathbf{0} & \mathbf{1} \\ -(\mathbf{H}^{(2)})^{-1}\left[\mathbf{H}^{(0)}(\mathbf{k}_{\|}) - E\right] & -(\mathbf{H}^{(2)})^{-1}\mathbf{H}^{(1)}(\mathbf{k}_{\|}) \end{bmatrix} \begin{bmatrix} \mathbf{C_k} \\ k_x\mathbf{C_k} \end{bmatrix} = k_x \begin{bmatrix} \mathbf{C_k} \\ k_x\mathbf{C_k} \end{bmatrix}. \tag{2.68}$$

It can be shown that the matrix $\mathbf{H}^{(2)}$ is non-singular[14]. Eq. (2.68) has $2M$ eigenvalues $k_{x,j}$ solutions and $2M$ corresponding eigenvectors $\mathbf{C}_{\mathbf{k},j}$. This method is much more convenient and efficient than some other calculations of the complex band structures, [16, 24] which involves finding the zeros of the secular determinant $\det[\mathbf{H}(\mathbf{k}) - E]$.

The boundary conditions are such that the wave function in the left region includes both the incoming and reflected plane-wave states, and the wave function on the right region has only transmitted plane-wave states. The eigenvalues $k_{x,j}$ in general can be complex values describing evanescent states. Following the treatment of boundary conditions by Ting *et al.*[11], we order the wave vectors $k_{x,j}$ such that $j = 1, 2, \ldots, M$ corresponds to the forward states which propagate or decay to the right (i.e. $k_{x,j}$ is either positive real number or its imaginary part is positive for electron states and vice versa for hole states), while $j = M+1, \ldots, 2M$ corresponds to the backward states which propagate or decay to the left. The boundary conditions can be described in the bulk eigenstate basis by choosing the proper form for the wave functions in the left and right regions:

$$\mathbf{F}_L = \exp(i\mathbf{k}_{\|} \cdot \mathbf{r}_{\|}) \sum_{j=1}^{M} \left(I_j e^{ik^L_{x,j}x} \mathbf{C}_{\mathbf{k},j} + r_j e^{ik^L_{x,j+M}x} \mathbf{C}_{\mathbf{k}_L,j+M} \right) , \tag{2.69}$$

$$\mathbf{F}_R = \exp(i\mathbf{k}_{\|} \cdot \mathbf{r}_{\|}) \sum_{j=1}^{M} t_j e^{ik^R_{x,j}x} \mathbf{C}_{\mathbf{k}_R,j} , \tag{2.70}$$

where $k^L_{x,j}$ and $k^R_{x,j}$ are the bulk complex wave vectors in the left and right regions respectively. In bulk crystals, the number of states propagating to the right should equal to the number of states propagating to the left. Similarly, the number of states decaying to the right should equal to the number of states decaying to the left.

Let $\mathbf{I}$, $\mathbf{r}$, and $\mathbf{t}$ be column vectors of dimension M containing the coefficients $\{I_j\}$, $\{r_j\}$, and $\{t_j\}$, respectively. $\mathbf{I}$ represents the known incoming states, while $\mathbf{r}$ and $\mathbf{t}$ describe the reflected and transmitted components. By examining Eqs. (2.69), and (2.70), we find that $\mathbf{I}$, $\mathbf{r}$, and $\mathbf{t}$ are related to the envelope function

coefficients by a simple basis transformation:

$$\begin{bmatrix} \mathbf{F}_1 \\ \mathbf{F}_2 \end{bmatrix} = \begin{bmatrix} \mathbf{D}^L_{11} & \mathbf{D}^L_{12} \\ \mathbf{D}^L_{21} & \mathbf{D}^L_{22} \end{bmatrix} \begin{bmatrix} \mathbf{I} \\ \mathbf{r} \end{bmatrix}, \tag{2.71}$$

$$\begin{bmatrix} \mathbf{F}_{N-1} \\ \mathbf{F}_N \end{bmatrix} = \begin{bmatrix} \mathbf{D}^R_{11} & \mathbf{D}^R_{12} \\ \mathbf{D}^R_{21} & \mathbf{D}^R_{22} \end{bmatrix} \begin{bmatrix} \mathbf{t} \\ \mathbf{0} \end{bmatrix}, \tag{2.72}$$

where $\mathbf{D}^L_{11}$, $\mathbf{D}^L_{12}$ and $\mathbf{D}^R_{11}$, $\mathbf{D}^R_{12}$ are $M \times M$ matrices whose column vectors are the eigenvectors $\mathbf{C}_{\mathbf{k}_L,j}$ and $\mathbf{C}_{\mathbf{k}_R,j}$ obtained by solving Eq. (2.68) for the left and right regions respectively, and arranged in the same order as the corresponding eigenvalues.

$$\mathbf{D}^\lambda_{11} = \left[\mathbf{C}_{\mathbf{k}_\lambda,1}, \quad \mathbf{C}_{\mathbf{k}_\lambda,2}, \ \ldots, \ \mathbf{C}_{\mathbf{k}_\lambda,M}\right], \tag{2.73}$$

$$\mathbf{D}^\lambda_{12} = \left[\mathbf{C}_{\mathbf{k}_\lambda,M+1}, \quad \mathbf{C}_{\mathbf{k}_\lambda,M+2}, \ \ldots, \ \mathbf{C}_{\mathbf{k}_\lambda,2M}\right], \tag{2.74}$$

and

$$\mathbf{D}^\lambda_{21} = \left[e^{ik^\lambda_{x,1}a}\mathbf{C}_{\mathbf{k}_\lambda,1}, \ e^{ik^\lambda_{x,2}a}\mathbf{C}_{\mathbf{k}_\lambda,2}, \ \ldots, \ e^{ik^\lambda_{x,M}a}\mathbf{C}_{\mathbf{k}_\lambda,M}\right], \tag{2.75}$$

$$\mathbf{D}^\lambda_{21} = \left[e^{ik^\lambda_{x,M+1}a}\mathbf{C}_{\mathbf{k}_\lambda,M+1}, \ e^{ik^\lambda_{x,M+2}a}\mathbf{C}_{\mathbf{k}_\lambda,M+2}, \ \ldots, \ e^{ik^\lambda_{x,2M}a}\mathbf{C}_{\mathbf{k}_\lambda,2M}\right], \tag{2.76}$$

where $\lambda = L, R$.

2.4.2 Calculation of Transmission Coefficients

Now pursuing along the same technique illustrated in section 2.2.3 for one-band model, we eliminate $\mathbf{r}$ and $\mathbf{t}$ from Eqs. (2.71) and (2.72)

$$\mathbf{F}_1 - \mathbf{D}^L_{12}\mathbf{D}^{L\ -1}_{22}\mathbf{F}_2 = \mathbf{D}^L_{11}\mathbf{I} - \mathbf{D}^L_{12}\mathbf{D}^{L\ -1}_{22}\mathbf{D}^L_{21}\mathbf{I}, \tag{2.77}$$

$$-\mathbf{D}^R_{21}\mathbf{D}^{R\ -1}_{11}\mathbf{F}_{N-1} + \mathbf{F}_N = \mathbf{0}. \tag{2.78}$$

which are the generalized multiband forms of Eqs. (2.21) and (2.22). These equations, together with Eq.(2.46) and (2.59), constitute a system of MN linear equations. It can be written in the following matrix form corresponding to the

generalized multiband model

$$\begin{bmatrix} \mathbf{1} & -\mathbf{D}_{12}^{L}\mathbf{D}_{22}^{L}{}^{-1} & \mathbf{0} & \cdots & \cdots & \cdots & \mathbf{0} \\ \mathbf{H}_{2,1} & \mathbf{H}_{2,2} & \mathbf{H}_{2,3} & \mathbf{0} & \cdots & \cdots & \mathbf{0} \\ \mathbf{0} & \mathbf{H}_{3,2} & \mathbf{H}_{3,3} & \mathbf{H}_{3,4} & \mathbf{0} & \cdots & \mathbf{0} \\ \vdots & & \ddots & \ddots & \ddots & \vdots & \\ \mathbf{0} & & & \mathbf{0} & \mathbf{H}_{N-1,N-2} & \mathbf{H}_{N-1,N-1} & \mathbf{H}_{N-1,N} \\ \mathbf{0} & \cdots & \cdots & \cdots & \mathbf{0} & -\mathbf{D}_{21}^{R}\mathbf{D}_{11}^{R}{}^{-1} & \mathbf{1} \end{bmatrix} \cdot \begin{bmatrix} \mathbf{F}_1 \\ \mathbf{F}_2 \\ \mathbf{F}_3 \\ \vdots \\ \mathbf{F}_{N-1} \\ \mathbf{F}_N \end{bmatrix}$$

$$= \begin{bmatrix} \mathbf{D}_{11}^{L}\mathbf{I} - \mathbf{D}_{12}^{L}\mathbf{D}_{22}^{L}{}^{-1}\mathbf{D}_{21}^{L}\mathbf{I} \\ \mathbf{0} \\ \mathbf{0} \\ \vdots \\ \mathbf{0} \\ \mathbf{0} \end{bmatrix}. \tag{2.79}$$

Having obtained the envelope function coefficients $\mathbf{F}_\sigma$, it follows from Eq. (2.72) that the coefficients of the transmitted plane-wave states are given by

$$\mathbf{t} = \mathbf{D}_{21}^{R}{}^{-1}\mathbf{F}_N. \tag{2.80}$$

The total transmission coefficient can be calculated from Eq. (2.55):

$$T(E, k_{\|}) = \sum_{j=1}^{M} |t_j(E, k_{\|})|^2 \frac{\mathrm{Re}(\mathbf{C}_j^\dagger \mathbf{J}_x \mathbf{C}_j)}{\mathrm{Re}(\mathbf{C}_I^\dagger \mathbf{J}_x \mathbf{C}_I)}. \tag{2.81}$$

It can be shown [16] that the current components for a given subband $\mathbf{j}_j = \mathrm{Re}(\mathbf{C}_j^\dagger \hat{\mathbf{J}} \mathbf{C}_j)$ is related to the group velocity $\mathbf{v}_j = \frac{1}{\hbar}\nabla_{\mathbf{k}} E_j(\mathbf{k})$ by

$$\mathbf{j} = \rho \mathbf{v}, \tag{2.82}$$

where $\rho = \mathbf{C}^\dagger \mathbf{C}$. So, the transmission coefficient T can also be expressed as

$$T(E, k_{\|}) = \sum_{j=1}^{M} |t_j(E, k_{\|})|^2 \frac{|v_j(E, k_{\|}; R)|}{|v_I(E, k_{\|}; L)|}. \tag{2.83}$$

2.4.3 Comparison with Other Existing Methods

We briefly compare our method with some other available methods. The well-known transfer matrix method has been employed for studying hole tunneling in the framework of **k·p** theory[15, 16, 24]. However, in addition to numerical instability problems occurred for devices larger than a few tens of Å, spherical approximation had to be used to simplify the multiband plane-wave solutions at each piecewise-constant potential region. The computational cost for an efficient implementation of the transfer matrix method is the same as our method[11]. Therefore the method we presented here has considerable advantage over the transfer-matrix method. The scattering matrix method developed by Ko and Inkson [18] overcomes the numerical instability in the transfer matrix method. However the gain in numerical stability is compensated by added computational cost in constructing the scattering matrix. The computational technique we developed here is similar to the MQTBM [11] for tight-binding models, namely, transforming the entire problem to a system of linear equations in the final form. They are both efficient, numerical stable and easy to implement. Our method based on **k·p** theory has the advantages of being readily familiar to many researchers and easily to extend to include the magnetic field and strain effects. However, the **k·p** theory can only be applied to problems involving small range in k-space around the Brillouin zone center. Problems like X-point tunneling are more easily studied under tight-binding framework[29]. Therefore, these two methods complement each other in various applications.

2.5 Applications to p-type GaAs/AlAs Double Barrier

For the purpose of illustration of our method, we consider hole-tunneling in p-type GaAs/AlAs double barrier resonant tunneling (DBRT) structure. Two types of

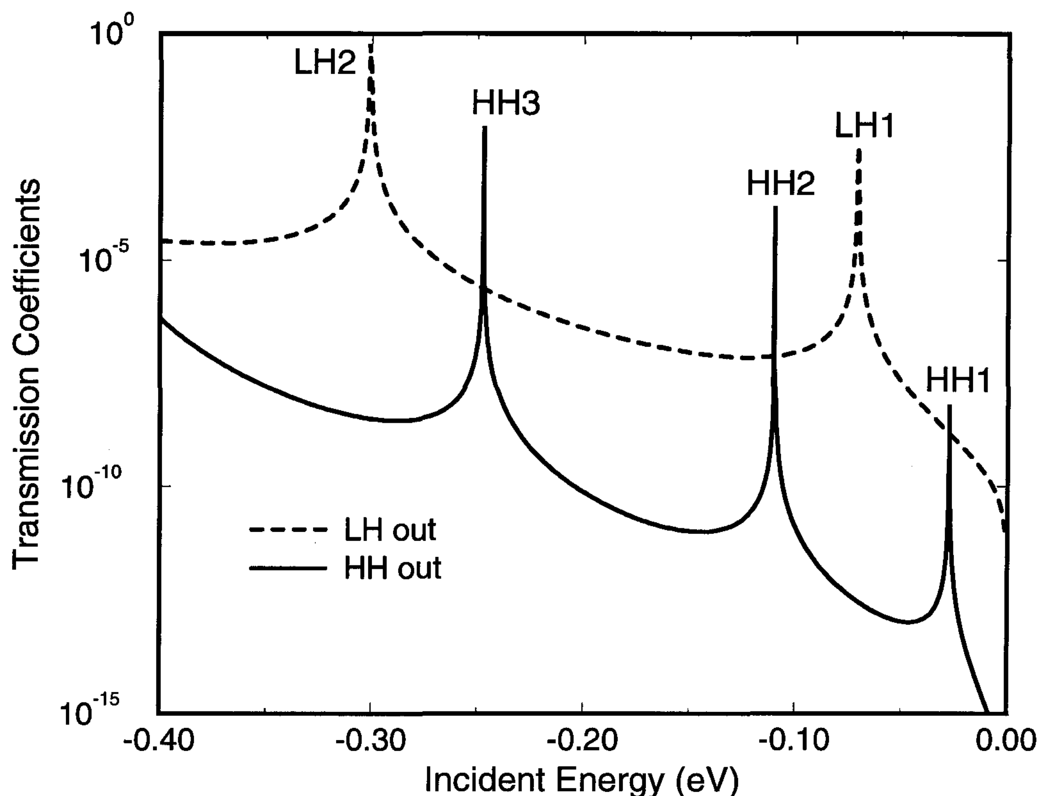

Figure 2.5: Transmission coefficients for heavy-hole (solid line) and light-hole (dashed line) states through a 30Å - 50Å - 30Å double barrier heterostructure with $k_{\|} = 0$.

carriers exist in the valence-band, heavy-hole and light-hole with different effective masses. If uncoupled, the carrier with lighter mass would have higher transmission probability than the heavier one, two independent sets of resonant transmission would be observed. However, the confinement in the double barrier structures introduces considerable hole-mixing effects. Experimental study have revealed this phenomenon[30].

The top of valence band Γ_8 states is described by the 4×4 Luttinger-Kohn Hamiltonian given in section 2.3.1. The lack of inversion symmetry in III-V sys-

tem is not represented by this Hamiltonian, therefore the bands have a twofold degeneracy at every point in $\mathbf{k}$ space. It is known that states $KJ\psi_{\mathbf{k},\uparrow} = \psi_{\mathbf{k},\downarrow}$ and $\psi_{\mathbf{k},\uparrow}$ are degenerate in energy and are orthogonal to each other, [31] where K is the Kramers time reversal operator and J is the space inversion operator.

Due to the degeneracy, the electron eigenstates $\mathbf{C}_k$ for a given energy E and $\mathbf{k}$ are not uniquely determined. For $\mathbf{k}_{\|} = 0$, the eigenstates are decoupled into spin-up and spin-down pure heavy-hole and light-hole states. In the case of $\mathbf{k}_{\|} \neq 0$, there are mixing between heavy-hole basis and light-hole basis. We construct and label the electron eigenstate basis in the following convention. The two degenerate basis for a given energy E and $\mathbf{k}$ are constructed to be $\psi_{\mathbf{k},\uparrow}$ and $KJ\psi_{\mathbf{k},\uparrow}$. For heavy- hole bands, $\psi_{\mathbf{k}_{hh},\uparrow}$ is constructed so that the heavy hole component with spin-down is zero

$$\mathbf{C}_{k_{hh},\uparrow} = (u_1, u_2, u_3, 0).$$

Its degenerate counterpart is therefore given by

$$\mathbf{C}_{k_{hh},\downarrow} = (0, u_3^*, -u_2^*, u_1^*),$$

in which the spin-up heavy hole component vanishes. Similarly, for light-hole bands, we choose

$$\mathbf{C}_{k_{lh},\uparrow} = (v_1, v_2, 0, v_4),$$

and

$$\mathbf{C}_{k_{lh},\downarrow} = (-v_4^*, 0, -v_2^*, v_1^*).$$

These four eigenstates are orthogonal to each other and constitute the basis for the electron states in the Γ_8 valence band.

The GaAs/AlAs double barrier resonant tunneling (DBRT) structure we consider has 50Å well width and 30Å barrier width. In our calculation of transmission coefficients, flat band condition is assumed. By assumption of the effective mass theory, the envelope functions vary slowly on the scale of the unit cell size, therefore it is a good approximation to take the lattice constant as the step size in our

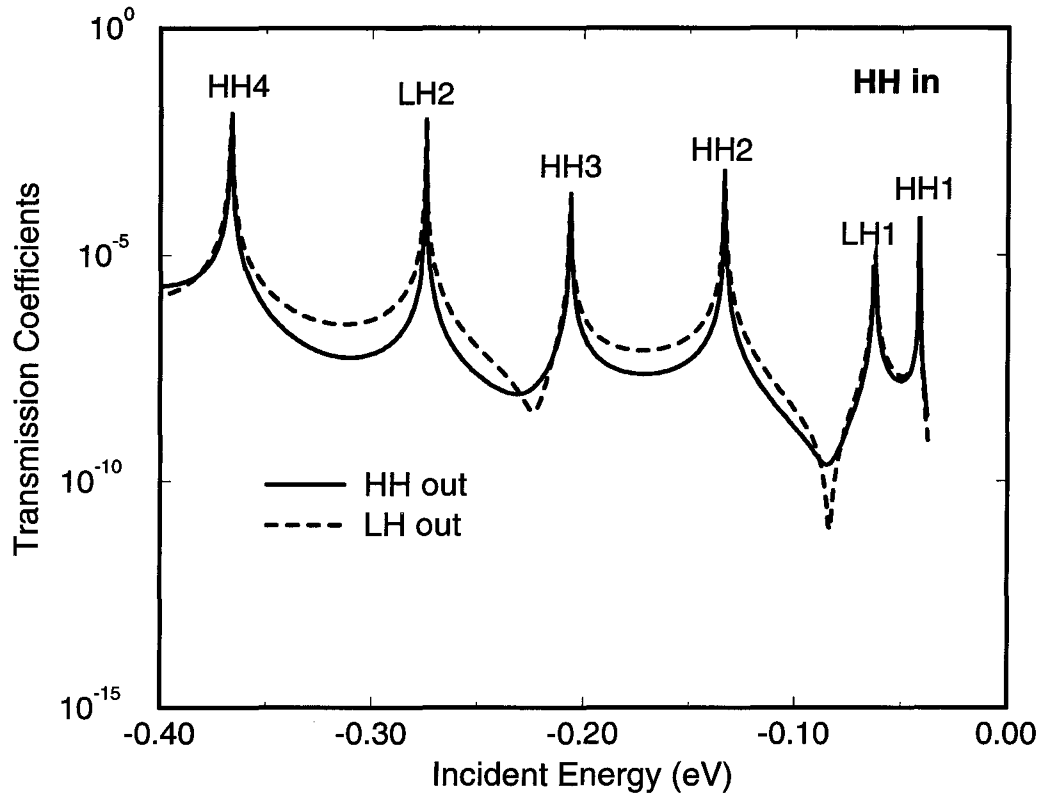

Figure 2.6: Transmission coefficients for heavy-hole (solid line) and light-holes (dashed line) channels with heavy-hole incoming state through a 30Å - 50Å - 30Å double barrier heterostructure with $k_{\|} = 0.03$ Å^{-1}.

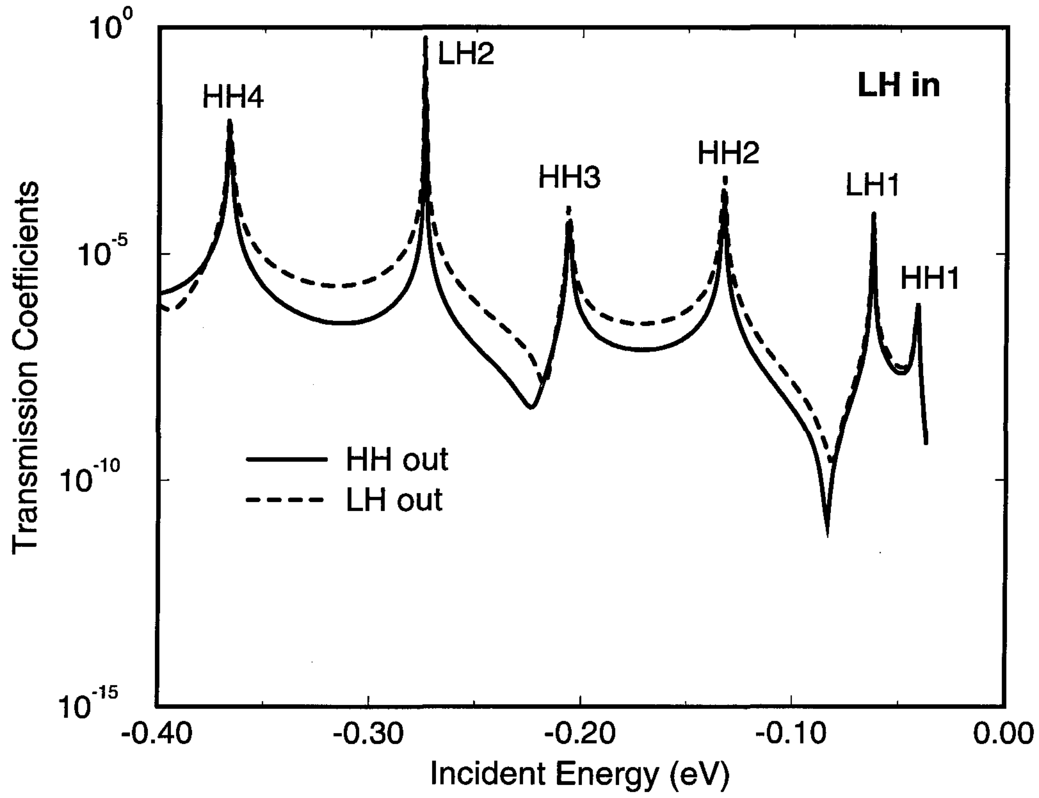

Figure 2.7: Transmission coefficients for heavy-hole (solid line) and light-hole (dashed line) channels with light-hole incoming state through a 30Å - 50Å - 30Å double barrier heterostructure with $k_{\|} = 0.03$ Å^{-1}.

discretization. Fig. 2.5 shows the transmission coefficients for normal incident HH and LH states. In the case $\mathbf{k}_{\|} = 0$, the HH and LH are decoupled. The resonant peaks correspond to the quasi-bound HH and LH states in the central GaAs well. As expected, the light hole state has higher transmission coefficient than the heavy hole due to smaller effective mass. In Figures 2.6 and 2.7, respectively, we show the transmission coefficients for incoming HH and LH states with $|\mathbf{k}_{\|}| = 0.03\text{Å}^{-1}$. The nonzero $\mathbf{k}_{\|}$ states contain mixing of heavy-hole and light-hole states, and interact with all the quasi-bound states formed in the well, resulting in multiple transmission resonances. The resonant states are labeled according to their dominant bulk-state component. Because of the hole-mixing effects, the incident heavy-hole state can transmit through not only heavy-hole channel, but also light-hole channel, and vice versa for the incident light-hole state. This hole-mixing effects in p-type GaAs/AlAs double barrier structures have been observed in the experimental $I - V$ characteristics[30].

2.6 Calculations of Electronic Band Structures

2.6.1 Confined Quantum Structures

Unlike quantum tunneling problems where the electron states are propagating plane-waves, the electron states in confined quantum structures such as quantum wells are spatially localized in the heterostructure growth direction. The wave function decay exponentially in the barrier regions and goes to zero at infinity, as depicted in Fig. 2.8. The discretized mash points are chosen so that the beginning $\sigma = 1$ and ending $\sigma = N$ are deep enough within the barrier regions. The wave functions at these positions are sufficiently small so that they can be neglected to the tolerance of numerical accuracy. The boundary conditions for confinement states therefore can be simply represented by

$$\mathbf{F}_1 = 0, \tag{2.84}$$

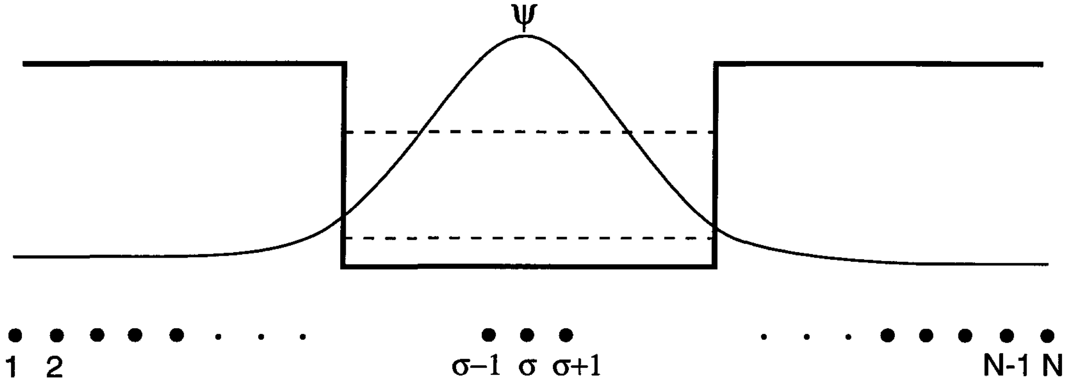

Figure 2.8: Schematic band diagram and electronic states in quantum well confinement. The wave-functions are confined mostly in the well regions and decay exponentially in the barrier region. The discretized regions are chosen so that the wave function at $\sigma = 1$ and $\sigma = N$ are sufficiently small to the tolerance of numerical accuracy.

$$\mathbf{F}_N = 0. \tag{2.85}$$

Combined with Eq. (2.46) and (2.59), the solution to Schrödinger's equation $HF = EF$ becomes a simple eigenvalue problem:

$$\begin{bmatrix} \mathbf{H}_{1,1} & \mathbf{H}_{1,2} & \mathbf{0} & \cdots & \cdots & \cdots & \mathbf{0} \\ \mathbf{H}_{2,1} & \mathbf{H}_{2,2} & \mathbf{H}_{2,3} & \mathbf{0} & \cdots & \cdots & \mathbf{0} \\ \mathbf{0} & \mathbf{H}_{3,2} & \mathbf{H}_{3,3} & \mathbf{H}_{3,4} & \mathbf{0} & \cdots & \mathbf{0} \\ \vdots & & \ddots & \ddots & \ddots & \vdots & \\ \mathbf{0} & & & \mathbf{0} & \mathbf{H}_{N-1,N-2} & \mathbf{H}_{N-1,N-1} & \mathbf{H}_{N-1,N} \\ \mathbf{0} & \cdots & \cdots & \cdots & \mathbf{0} & \mathbf{H}_{N,N-1} & \mathbf{H}_{N,N} \end{bmatrix} \cdot \begin{bmatrix} \mathbf{F}_1 \\ \mathbf{F}_2 \\ \mathbf{F}_3 \\ \vdots \\ \mathbf{F}_{N-1} \\ \mathbf{F}_N \end{bmatrix} = 0. \tag{2.86}$$

The number of eigenvalue solutions E_n equals to the dimension of the matrix $N \times M$ in Eq. (2.86). However, not all the solutions satisfy the boundary conditions $\mathbf{F}_1 = \mathbf{F}_N = 0$. The truly confined states that vanish exponentially in the barrier

regions are those satisfying the condition

$$V_{\text{well}} < E_n < V_{\text{barrier}} \,. \tag{2.87}$$

The rest are merely standing wave states with nods at x_1 and x_N, and energies beyond barrier height V_{barrier}. The number of the confined states should be independent of parameters like spacing a and the number of discretizing points N.

In Fig. 2.9, we show the calculated hole subband dispersion in the valence-band of a GaAs quantum well of 50 Å thickness with AlAs barrier on two sides. The subbands are labeled according to their dominant bulk component at $\mathbf{k}_{\|} = 0$. The quantum confinement introduces substantial heavy-hole and light-hole mixing effects at $\mathbf{k}_{\|} \neq 0$. Negative hole effective mass is exhibited in certain subband dispersion. In the GaAs/AlAs double barrier structures with the same GaAs well thickness that we studied in section 2.5, quasi-bound hole states are formed in the GaAs well, and are responsible for the resonances in the transmission spectrum. Close resemblance can be seen between the resonant peaks in Figs. 2.5–2.7 and the corresponding hole subbands calculated here.

2.6.2 Superlattices

Superlattice is a periodic structure consisting of alternating layers of different materials, as shown in Fig. 2.10. The superlattice structure dramatically modulates the electronic subband structures in the growth direction, and offers many interesting possibilities of engineered structures and potential technological applications depending on the choice of materials and layer thickness[32, 33, 34, 35]. The finite-difference method we developed in section 2.3.3 can be easily extended to the calculations of superlattice band structures with appropriate formulation of boundary conditions.

Since superlattice displays translational symmetry in the growth direction x with periodicity d, we can associate with that a quantum number q, the wave-vector along the x direction. The Bloch condition $\psi(x + md) = e^{imqd}\psi(x)$ implies

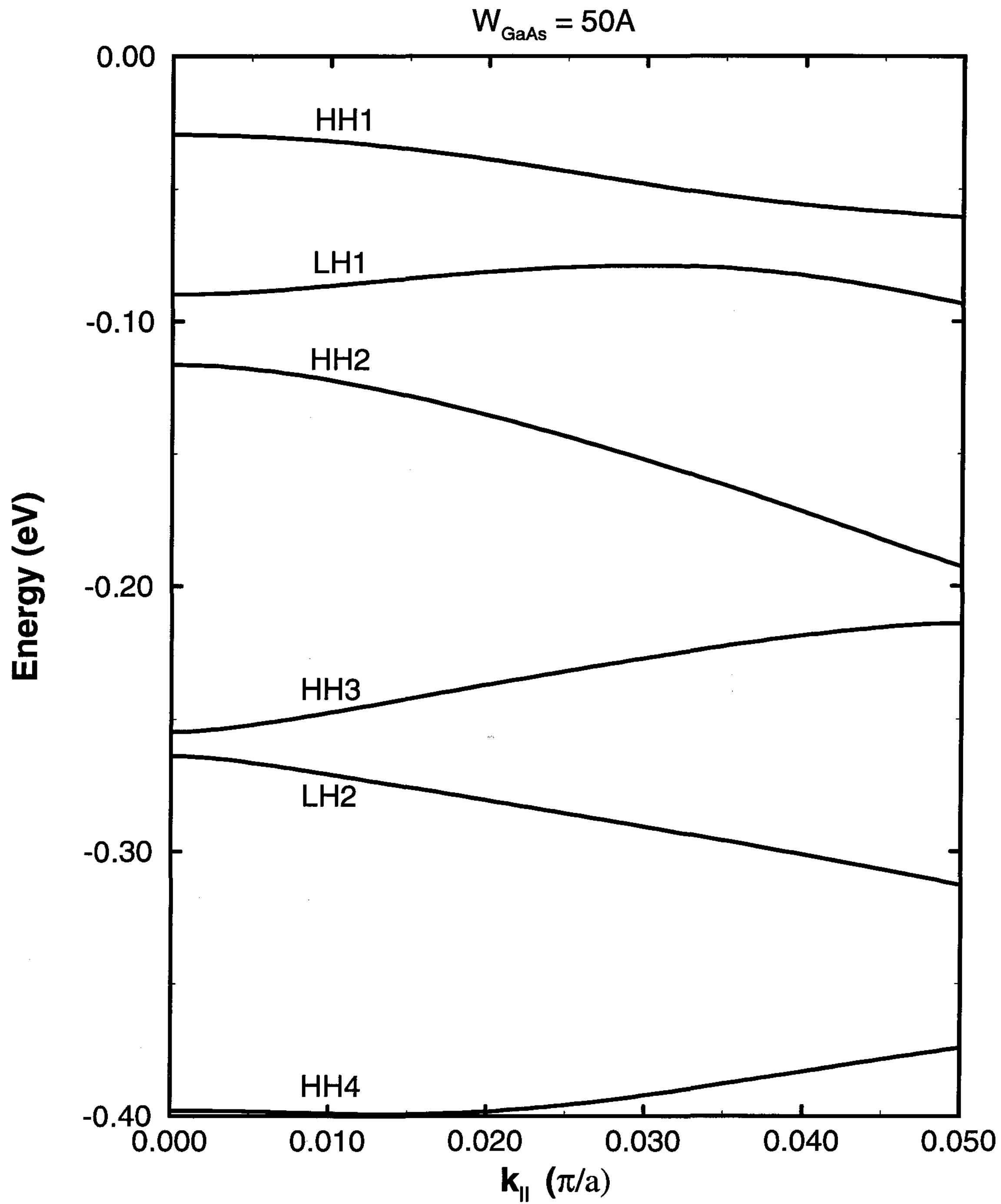

Figure 2.9: The hole subband dispersion in a 50 Å GaAs quantum well sandwiched between AlAs barrier. The energy zero is chosen to be the valence-band edge of GaAs. The subbands are labeled according to their dominant bulk-state component.

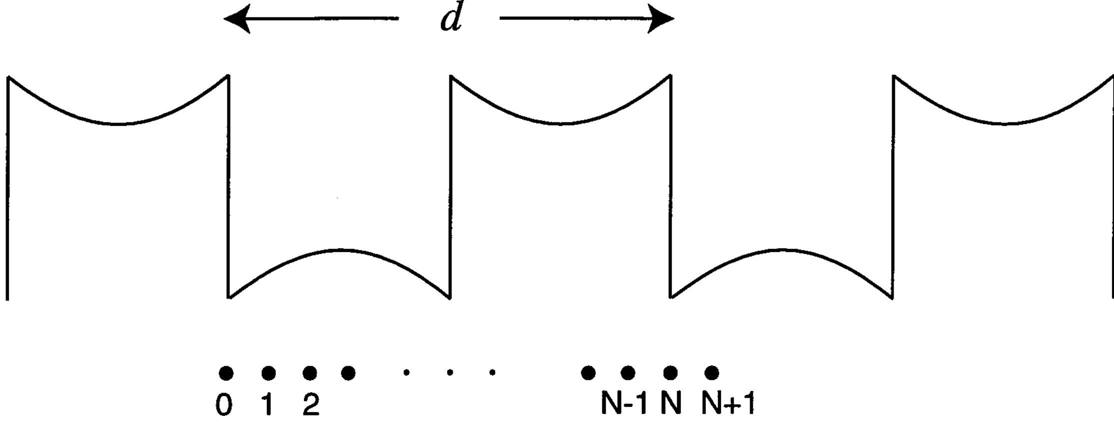

Figure 2.10: Schematic band diagram of a superlattice with periodicity d along the growth direction. To calculate the superlattice subband structures, the supercell is discretized into N lattice points along the growth direction, typically with the spacing chosen to be the same as lattice constant of the constituent materials.

the following boundary condition

$$\mathbf{F}_N = \mathbf{F}_0 e^{iqd} . \tag{2.88}$$

Together with Eq. (2.46) and (2.59), the solutions to electronic band structures in superlattices become the following eigenvalue problem:

$$\begin{bmatrix} \mathbf{H}_{1,1} & \mathbf{H}_{1,2} & \mathbf{0} & \cdots & \cdots & \cdots & \mathbf{H}_{1,0}e^{-iqd} \\ \mathbf{H}_{2,1} & \mathbf{H}_{2,2} & \mathbf{H}_{2,3} & \mathbf{0} & \cdots & \cdots & \mathbf{0} \\ \mathbf{0} & \mathbf{H}_{3,2} & \mathbf{H}_{3,3} & \mathbf{H}_{3,4} & \mathbf{0} & \cdots & \mathbf{0} \\ \vdots & & \ddots & \ddots & \ddots & \vdots & \\ \mathbf{0} & & & \mathbf{0} & \mathbf{H}_{N-1,N-2} & \mathbf{H}_{N-1,N-1} & \mathbf{H}_{N-1,N} \\ \mathbf{H}_{N,N+1}e^{iqd} & \cdots & \cdots & \cdots & \mathbf{0} & \mathbf{H}_{N,N-1} & \mathbf{H}_{N,N} \end{bmatrix} \cdot \begin{bmatrix} \mathbf{F}_1 \\ \mathbf{F}_2 \\ \mathbf{F}_3 \\ \vdots \\ \mathbf{F}_{N-1} \\ \mathbf{F}_N \end{bmatrix} = 0 . \tag{2.89}$$

Solving Eq. (2.89) yields the superlattice electronic subband dispersion $E(q)$.

We have applied the technique to two systems: lattice-matched InAs-GaSb superlattices and strained InAs-$Ga_{1-x}In_xSb$ superlattices. 8×8 $\mathbf{k}\cdot\mathbf{p}$ Hamiltonian is used in the calculations, which includes Γ_6 conduction-band, the Γ_8 light-hole and

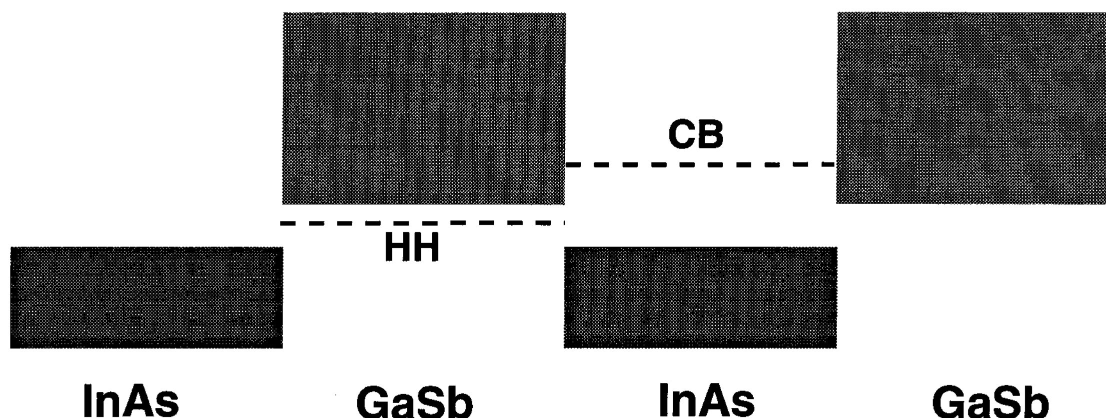

Figure 2.11: Schematic band diagram of lattice-matched InAs/GaSb superlattice. The superlattice conduction subband is formed from electron states confined in the InAs layer, and valence subband from the heavy-hole states confined in the GaSb layer.

heavy-hole bands, and the Γ_7 spin-orbit split-off valence-band. Explicit representations of the $\mathbf{k}\cdot\mathbf{p}$ Hamiltonian matrices are given in Appendix A.1. Due to their staggered type-II band alignment, electron and hole states are confined in separate adjacent layers. The resulted superlattice band structures depend strongly on the constituent layer thickness and exhibit some very interesting properties.

Fig. 2.11 and Fig. 2.12 show the schematic band diagram of InAs/GaSb superlattice and the calculated band dispersions for wave vectors both parallel and perpendicular to the [001] growth axis. The superlattice band-gap derives from the electron states confined mostly in the InAs conduction-band and the heavy-hole states confined in the GaSb valence-band. It depends strongly on the layer thickness due to quantum confinement effects. The superlattice structure in our calculation consists of 8 monolayers of InAs alternating with 8 monolayers of

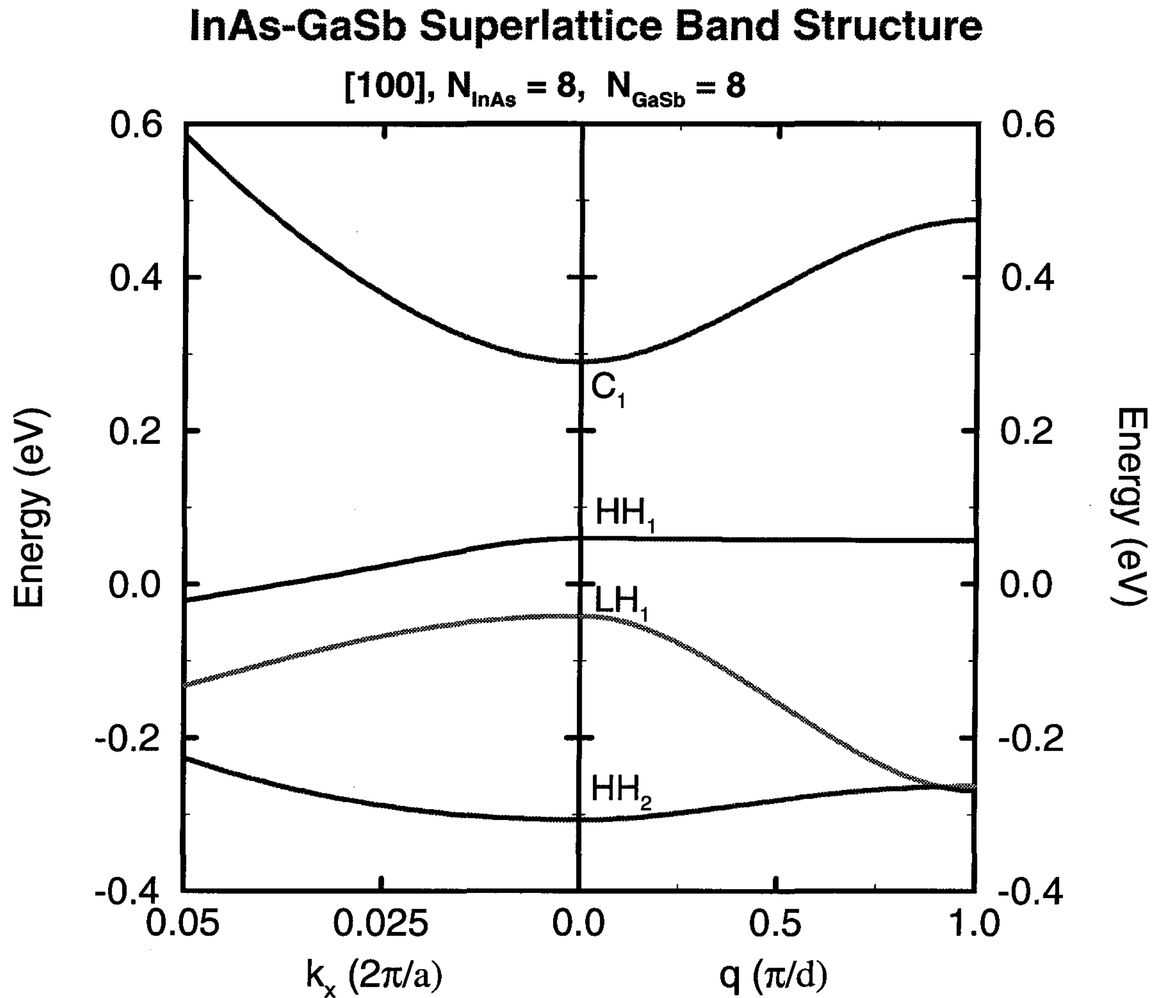

Figure 2.12: Electronic energy-band structure of a [001] lattice-matched superlattice consisting of 8 monolayers of InAs alternating with 8 monolayers of GaSb. The energy zero coincides with the conduction-band minimum of the bulk InAs.

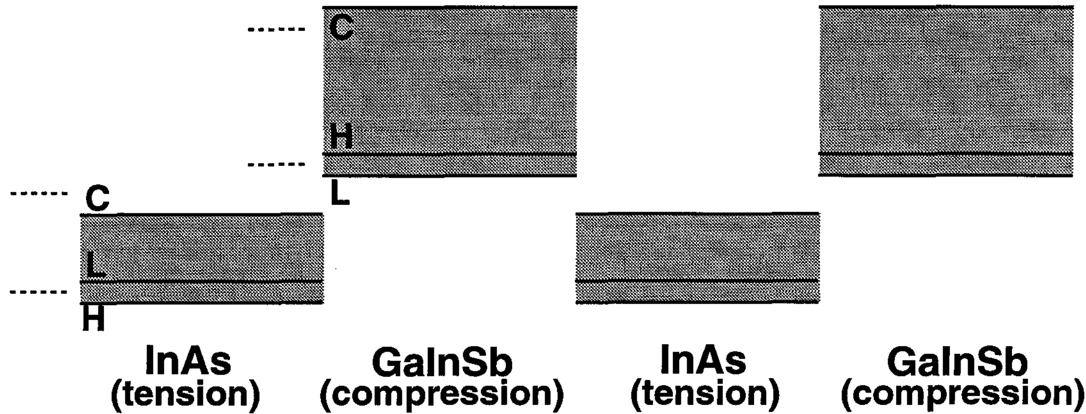

Figure 2.13: Schematic band diagram of strained InAs/$Ga_{1-x}In_xSb$ superlattice. The InAs layer is under tension strain while the $Ga_{1-x}In_xSb$ layer is under compression strain. The biaxial strains result in shift of band edges and splitting of heavy-hole and light-hole bands. The dashed lines indicate the band edges without strain.

GaSb. Subbands are labeled according to their dominant bulk-state component: conduction(C), heavy-hole(HH), and light-hole(LH). Spin split-off hole subbands are not shown here.

Fig .2.13 shows the schematic band diagram of strained InAs/$Ga_{1-x}In_xSb$ and Fig. 2.14 shows the calculated band dispersions for wave vectors both parallel and perpendicular to the [001] growth axis. The biaxial tension strain in InAs lowers the conduction band minimum, while the biaxial compression strain in $Ga_{1-x}In_xSb$ raises the heavy-hole band by deformation potential effects[34]. The superlattice band gap derives from electron states split up from the InAs conduction-band minimum and heavy-hole states split down from the $Ga_{1-x}In_xSb$ valence-band maximum by quantum confinement effects. Therefore, the presence of internal strain reduces the superlattice band gap at a given layer thickness, or equivalently

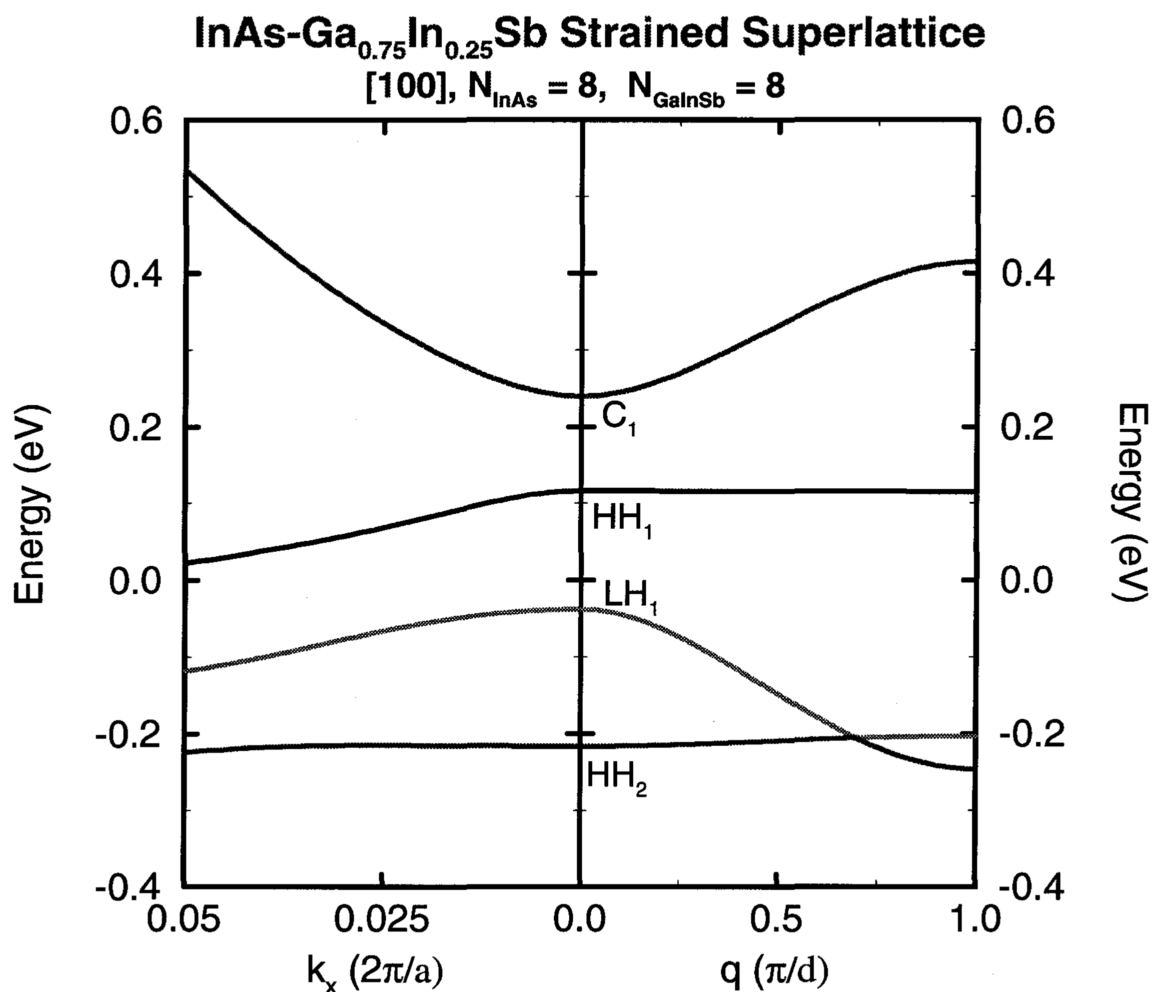

Figure 2.14: Calculated electronic energy-band structure of a [001] strained superlattice consisting of 8 monolayers of InAs alternating with 8 monolayers of $Ga_{1-x}In_xSb$. The energy zero coincides with the conduction-band minimum of the bulk InAs.

increases the superlattice cutoff wavelength. This result has lead to the proposal of long-wavelength infrared detector by C. Mailhiot and D. L. Smith[34], and subsequent experimental study by R. Miles *et al.*[35]. The strain induced band gap reduction is shown in Fig. 2.14, and the calculated band gap agrees very well with the experimental measurement[35].

2.7 Summary

We have developed a new method for quantum transport and electronic band structure calculations in semiconductor heterostructures. The method is based on the multiband **k·p** theory and the Multiband Quantum Transmitting Boundary Method. The method circumvents the numerical instability encountered in transfer matrix method. In addition to numerical stability, it is also efficient and easy to implement. The formulation based on **k·p** theory makes it suitable for studying problems involving strain and magnetic field effects. We have demonstrated the utility of the method by applying it to the *p*-type GaAs/AlAs double barrier tunnel structures. With appropriate formulation of boundary conditions, our technique has also been applied to the calculations of electronic band structures in quantum confined states and superlattice structures.

Bibliography

[1] R. Tsu and L. Esaki, *Appl. Phys. Lett.* **22**, 562 (1973).

[2] T. C. L. G. Sollner, W. D. Goodhue, P. E. Tannenwald, C. D. Parker, and D. D. Peck, *Appl. Phys. Lett.* **43**, 588 (1983).

[3] E. R. Brown, C. D. Parker, L. J. Mahoney, J. R. Söderström, and T. C. McGill, presented at *the 48th Annual Device Research Conference*, Santa Barbara, CA (1990).

[4] J. R. Söderström, D. H. Chow, and T. C. McGill, *Appl. Phys. Lett.* **55**, 1094 (1989).

[5] L. F. Luo, R. Beresford, and W. I. Wang, *Appl. Phys. Lett.* **55**, 2023 (1989).

[6] R. Beresford, L. F. Luo, and W. I. Wang, *Appl. Phys. Lett.* **56**, 551 (1990); *Appl. Phys. Lett.* **56**, 952 (1990).

[7] D. A. Collins, E. T. Yu, Y. Rajakarunanayake, J. R. Söderström, D. H. Chow, D. Z.-Y. Ting, and T. C. McGill, *Appl. Phys. Lett.* **57**, 683 (1990).

[8] H. J. Levy, D. A. Collins, and T. C. McGill, in Proceedings of the 1992 IEEE International Symposium on Circuits and Systems, San Diego, CA (1992).

[9] H. J. Levy, and T. C. McGill, *IEEE Trans. Neural Nets* **4**, 427(1993).

[10] J. R. Söderström, E. T. Yu, M. K. Jackson, Y. Rajakarunanayake, and T. C. McGill, *J. Appl. Phys.* **68**, 1372 (1990).

[11] D. Z.-Y. Ting, E. T. Yu, and T. C. McGill, *Phys. Rev. B* **45**, 3583 (1992).

[12] E. O. Kane, *Tunneling Phenomena in Solids*, edited by E. Burstein and S. Lundqvist, (Plenum Press, New York, 1969), p. 1.

[13] M. Altarelli, *Heterojunctions and Semiconductor Superlattices*, Edited by G. Allan, G. Bastard, N. Boccara, M. Lannoo, and M. Voos (Springer-Verlag, 1986).

[14] D. L. Smith and C. Mailhiot, *Phys. Rev. B* **33**, 8345 (1986).

[15] G. Y. Wu, K.-M. Huang, and C.-J. Chen, *Phys. Rev. B* **46**, 1521 (1992).

[16] C. Y. Chao and S. L. Chuang, *Phys. Rev. B* **43**, 7027 (1991).

[17] D. Z.-Y. Ting, E. T. Yu, and T. C. McGill, *Phys. Rev. B* **45**, 3576 (1992).

[18] D. Y. K. Ko and J. C. Inkson, *Phys. Rev. B* **38**, 9945 (1988).

[19] W. R. Frensley, *Rev. Mod. Phys.* **62**, 745 (1990).

[20] C. S. Lent and D. J. Kirkner, *J. Appl. Phys.* **67**, 6353 (1990).

[21] Y. X. Liu, D. Z.-Y. Ting, and T. C. McGill, to be published in *Phys. Rev. B*, (1995).

[22] J. M. Luttinger and W. Kohn, *Phys. Rev.* **97**, 869 (1955).

[23] E. O. Kane, *Semiconductors and Semimetals*, edited by R. K. Willardson and A. C. Beer (Academic, New York, 1966) Vol. 1, p. 75.

[24] R. Wessel and M. Altarelli, *Phys. Rev. B* **39**, 12802 (1989).

[25] G. C. Osbourn, *Phys. Rev. B* **27**, 5126(1983).

[26] G. L. Bir and G. E. Pikus, *Symmetry and Strain Induced Effects in Semiconductors*, (Wiley, New York, 1974).

[27] J. H. Wilkinson, *The Algebraic Eigenvalue Problem*, (Oxford University Press, 1965) p. 633-634.

[28] Y. C. Chang and J. N. Schulman, *Phys. Rev. B* **25**, 3975 (1982).

[29] D. Z.-Y. Ting and T. C. McGill, *Phys. Rev. B* **47**, 7281 (1993).

[30] E. E. Mendez, W. I. Wang, B. Ricco, and L. Esaki, *Appl. Phys. Lett.* **47**, 415 (1985).

[31] C. Kittel, *Quantum Theory of Solids*, (John Wiley & Sons, Inc, New York, 1963).

[32] See for example, L. Esaki, *Heterojunctions and Semiconductor Superlattices*, Edited by G. Allan, G. Bastard, N. Boccara, M. Lannoo, and M. Voos (Springer-Verlag, 1986).

[33] J. N. Schulman, and T. C. McGill, *Appl. Phys. Lett.* **34**, 663 (1979).

[34] D. L. Smith, C. Mailhiot, *J. Appl. Phys.* **62**, 2545 (1987).

[35] R. H. Miles, D. H. Chow, J. N. Schulman, and T. C. McGill, *Appl. Phys. Lett.* **57**, 801 (1990).

Chapter 3

Magnetotunneling in Interband Tunnel Structures

3.1 Introduction

Magnetic field has been an important tool in the investigation of electronic structure and carrier transport properties in semiconductor heterostructures[1]. Resonant magnetotunneling spectroscopy (RMTS) technique, with magnetic field aligned parallel to the interface, has been used to probe the in-plane subband dispersions of the well states in double barrier heterostructures[2, 3, 4, 5]. The essential principle is that the transverse magnetic field, while does no work to carriers, lends an additional contribution to the momentum. The carriers in the emitter will be shifted out in k space with respect to the well states by an amount proportional to the B field, while the applied voltage tunes the energy of the carriers in the emitter to that of the quantum well states. Therefore, the change reflected in $I - V$ characteristics as the applied B field varies provides an indirect way to probe the subband structures in the quantum wells.

Resonant magnetotunneling study has been focused primarily on intraband tunneling structures, where the carriers in the initial, intermediate and final tun-

neling states are of the same type. Interband Tunnel Structures (ITS), on the other hand, exploit device systems involving transport and coupling between electron states in the conduction-band and hole states in the valence-band. The interband tunnel structures based on nearly lattice-matched InAs/GaSb/AlSb material system has been a subject of great interests recently due to the tremendous flexibility it offers for heterostructure device design. The most interesting feature in band alignments of this system is the Type II broken-gap between InAs and GaSb, where the band gaps of the two materials do not overlap with the conduction-band edge of InAs 0.15eV below the valence-band edge of GaSb. Various interband devices have been studied both experimentally and theoretically[6]–[12], revealing rich physics and great potential in device applications.

In this chapter, we applied the technique developed in chapter 2 for multiband **k·p** treatment of quantum transport to the study of interband magnetotunneling in InAs/GaSb/AlSb systems. The two interband device structures we consider are: the Resonant Interband Tunneling (RIT) structure made up of InAs-AlSb-GaSb-AlSb-InAs, and the Barrierless Resonant Interband Tunneling (BRIT) structure consisting of a GaSb well sandwiched between two InAs electrodes, as illustrated in Fig 3.1. Electrons from InAs electrodes interact with the quasi-bound hole states in GaSb well, giving rise to resonant interband tunneling. It is understood that the primary interband transport mechanism arises from the coupling between the light-hole states in GaSb well and InAs conduction-band states[13]. Although the heavy-hole states in the GaSb well are believed to introduce additional transmission resonances and substantial hole-mixing effects[14], evidence of heavy-hole contributions to the current-voltage characteristics is not clear. Resonant magnetotunneling technique provides an effective method to study the interactions of incident electrons with various hole subbands in the GaSb well, thus, allows us to examine the role of heavy-holes in the interband tunneling processes.

We begin with a brief description of theoretical treatment of magnetic field in **k·p** theory and the technique for current-voltage calculations in section 3.2. Detail

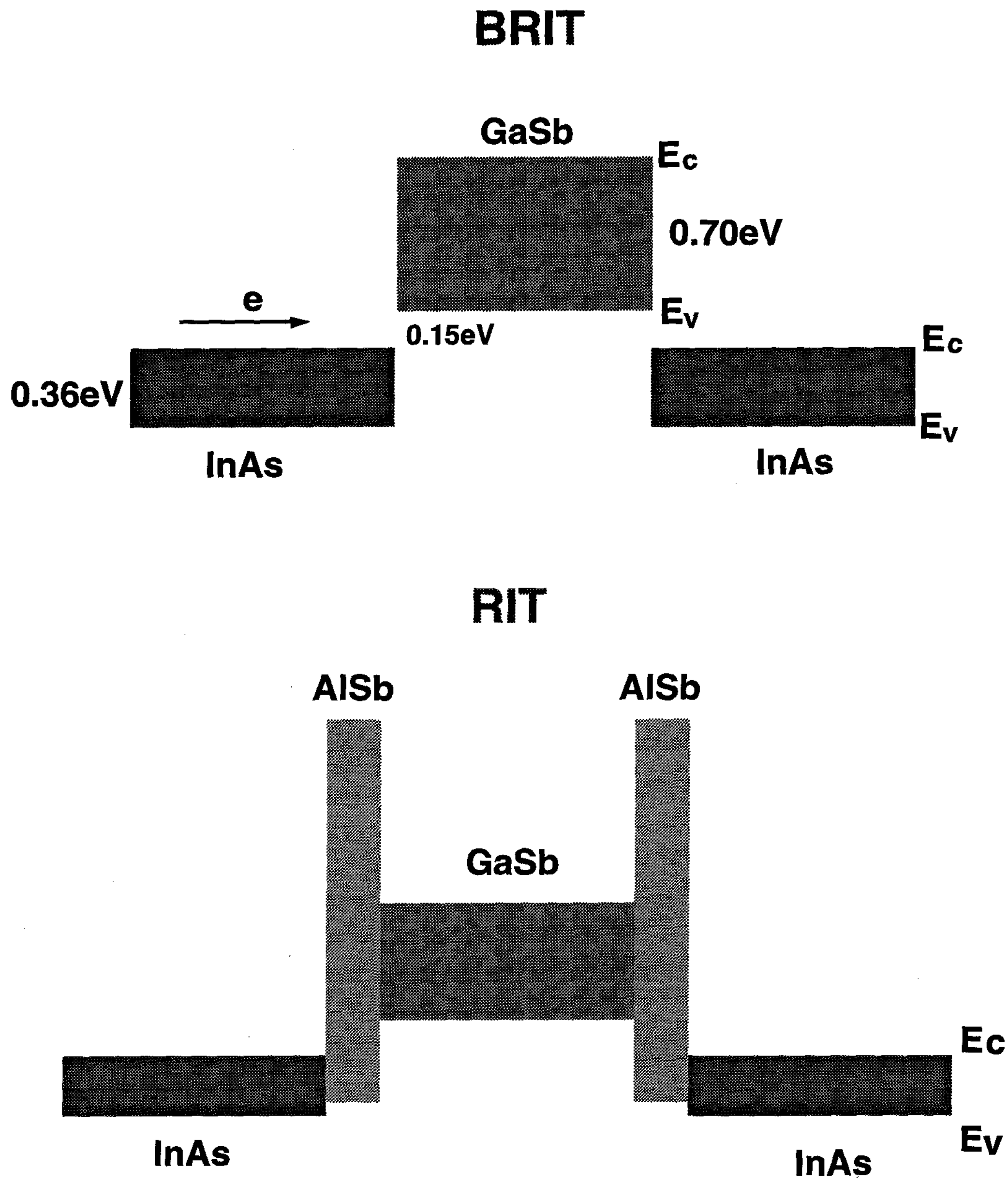

Figure 3.1: Schematic band diagrams for the InAs-GaSb-InAs BRIT structure and the *p*-well InAs-AlSb-GaSb-AlSb-InAs RIT structure.

studies of band structures, transmission coefficients, and $I-V$ characteristics under transverse external magnetic field for RIT and BRIT structures are presented in section 3.3 and 3.4 respectively. A brief discussion of computational cost in our simulation and the limitation to extend the study to the cases with magnetic field aligned in other directions are given in section 3.5. Section 3.6 summarizes the results.

3.2 Method

Because of the strong interaction between electrons in the conduction-band of InAs and holes in valence-band of GaSb, theoretical study of interband tunnel structures should include both conduction-band and valence-band states in the band structure models. We employed eight-band **k·p** Hamiltonian in our calculation. The basis set contains the Γ_6 conduction-band, the Γ_8 light-hole and heavy-hole bands, and the Γ_7 spin-orbit split-off valence-band. Explicit representations of the basis set and **k·p** Hamiltonian matrices are given in Appendix A.1.

k·p method provides a natural theoretical basis for studying magnetic fields in semiconductors. The incorporation of a magnetic field in the **k·p** Hamiltonian follows the lines of the classical work of Luttinger[15] on the cyclotron resonance of holes in semiconductors. The introduction of magnetic field is included by simply replacing the wave vector **k** by

$$\mathbf{k}' \longrightarrow -i\nabla - \frac{q}{c\hbar}\mathbf{A} \tag{3.1}$$

in the **k·p** Hamiltonian, where **A** is the vector potential which is related to the magnetic field by

$$\mathbf{B} = \nabla \times \mathbf{A}. \tag{3.2}$$

Also, additional constant terms representing the direct interaction of the electron and hole spins to the magnetic field arise. Explicit expression of these terms are given in Appendix A.3.

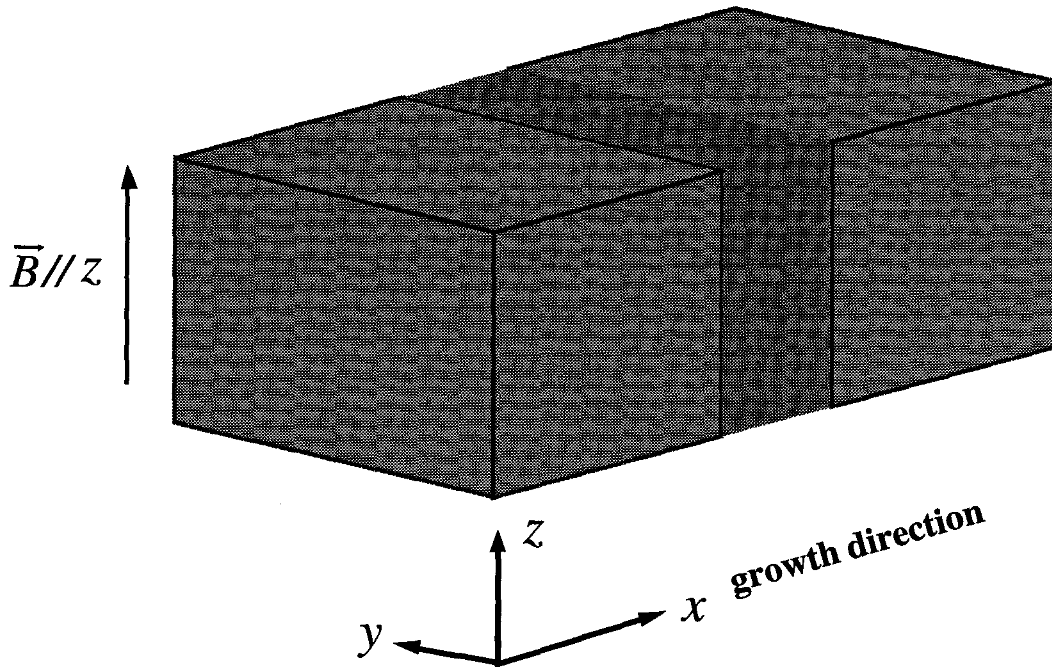

Figure 3.2: The growth direction of the tunnel structure is chosen along the x-axis. The external transverse magnetic field is applied along the z-axis, perpendicular to the transport direction.

In our study of magnetotunneling in InAs/GaSb/AlSb, the external magnetic field is applied long the z direction, perpendicular to the growth direction x, as shown in Fig. 3.2. Landau gauge for vector potential in this set-up is chosen so that

$$\mathbf{A} = (0, Bx, 0) \Longrightarrow \mathbf{B} = B\hat{z}. \tag{3.3}$$

Translational invariance parallel to the growth plane implies that transverse canonical momentum $\mathbf{k}_{\|} = (0, k_y, k_z)$ is still a good quantum number with k_y replaced by

$$k_y^{'} \Longrightarrow k_y + \frac{e}{c\hbar}Bx\,. \tag{3.4}$$

The effect of transverse magnetic field on the tunneling electron is to increase its mechanical momentum $k_y^{'}$ along the y-axis by $eBx/c\hbar$. The electrons in the

emitter will be shifted out in k space with respect to the well states, so that tunneling can occur through states with in-plane momentum different from that in the emitter. This allows us to probe the coupling between incident electrons from InAs electrodes and various hole states in the GaSb well, and to study the effects of valence band structures in the GaSb well in the interband tunneling structures.

To calculate the current-voltage characteristics, the energy-band profile of the heterostructure has to be obtained for a given applied bias. We compute the energy-band profile by solving Poisson's equation across the device, imposing a condition of charge neutrality over the entire device structure. The Thomas-Fermi approximation is used to relate the positions of the conduction- and valence-band edges at a given point to the local carrier concentration, and the effects of finite temperature on the Fermi distribution are included. For the band-bending calculations, a simple parabolic band structure model is typically assumed for the conduction and valence bands.

Having obtained the energy-band profile, the transmission coefficient for a carrier with a given energy E and in-plane wave vector $\mathbf{k}_{\|}$ is computed. Using the Landau gauge chosen in Eq. (3.3), the solutions to Schrödinger's equation is a one-dimensional problem. Therefore, the technique we developed in chapter 2 for discretizing the effective mass Schrödinger's equation and formulating boundary condition for tunneling can be applied to the calculations of transmission coefficients in the magnetotunneling study here.

The current density can be obtained following the approach of Duke[16] by integrating over the Fermi distribution of the incident electron population, including appropriate Fermi factors for occupied states in the emitter and empty states in the collector, and including appropriate velocity factors for the incident electrons. The total energy E and the wave vector component parallel to the device $\mathbf{k}_{\|}$ are taken to be conserved. The current density J is then given by[16]

$$J = \frac{e}{4\pi^3\hbar} \int T(E, \mathbf{k}_{\|})[f(E) - f(E + eV)] dE_{\perp} d^2\mathbf{k}_{\|}, \tag{3.5}$$

where V is the bias voltage applied to the device structure, and $T(E, \mathbf{k}_{\|})$ is the transmission coefficient.

Current-voltage characteristics computed this way include only the pure elastic transport process, which is responsible for giving rise to the main features observed in the experiments. Various scattering processes, such as electron-phonon scattering, electron-electron scattering, impurity scattering, and interface roughness, etc. are neglected. These scattering effects are important for detailed account of $I - V$ characteristics. They mainly modify the valley current in the resonant interband tunneling devices and are all very difficult to treat quantitatively and correctly.

3.3 Resonant Interband Tunneling (RIT) Structures

The resonant interband tunneling (RIT) structure we studied is the p-well RIT, as shown in Fig. 3.1. AT low bias, the electrons from the conduction band states in the InAs electrode interact with the quasi-bound hole states in the GaSb valence-band well to produce the resonant tunneling. For large voltage beyond resonance, the electrons must tunnel not only through the AlSb barriers, but also through the forbidden energy gap of the GaSb well. This leads to very strong suppression of the valley current, resulting in extremely high peak-to-valley ratio in $I - V$ characteristics. Peak-to-valley ratio as high as 20 (88) at 300K (77K) has been reported in the RIT devices[6].

3.3.1 Band Structures in GaSb Well

The valence-band structures in quantum wells are considerably more complex than conduction-band. Various hole subbands and significant mixing between heavy-hole states and light-hole states take place due to the quantum confinement. The resonant tunneling through the hole subbands formed in the quantum well are

responsible for the peak current observed in the $I - V$ characteristics. The hole subband dispersions in the GaSb valence-band well are calculated using the technique described in section 2.6.1.

Fig. 3.3 shows the calculated subband dispersions for three different GaSb well widths, 70Å, 80Å and 120Å at zero magnetic field. In RIT structures, the electrons only interact with hole subbands in GaSb wells in the energy range between the conduction-band edge of InAs and the valence-band edge of GaSb. Therefore, we only plot the subbands in this energy range of interests. The subbands are labeled according to their dominant bulk-state component. Each subband is two-fold spin-degenerate [1]. The calculations show that as the well width increases, the number of hole subbands formed in this energy range increases as expected. Strong hole mixing and non-parabolic dispersion occur as a result of quantum confinement. Also negative hole effective mass dispersion arises for certain subbands.

When external magnetic field is applied, the two-fold spin degeneracy is lifted, resulting in splitting of spin-up and spin-down states, as shown in Fig. 3.4. The subbands also shift in $k_{||}$ space as a result of applied magnetic field. In addition, the transverse magnetic field adds additional confinement to the electrons along the growth direction, giving rise to enhanced hole mixing and the interactions among the subbands. This is more evident for wider well width and stronger magnetic field.

3.3.2 Transmission Coefficients

Using the efficient and numerically stable multiband $\mathbf{k}\cdot\mathbf{p}$ technique developed in chapter 2, we have calculated the transmission coefficients in the RIT structures. Fig. 3.5 shows the transmission coefficients calculated for a RIT structure with 70Å GaSb well width and 40Å AlSb barrier width under flat band conditions for several

[1] Strictly speaking, the zinc-blend structures do not have the two-fold spin degeneracy due to lack of inversion symmetry. However the split is too small to account for in our calculations.

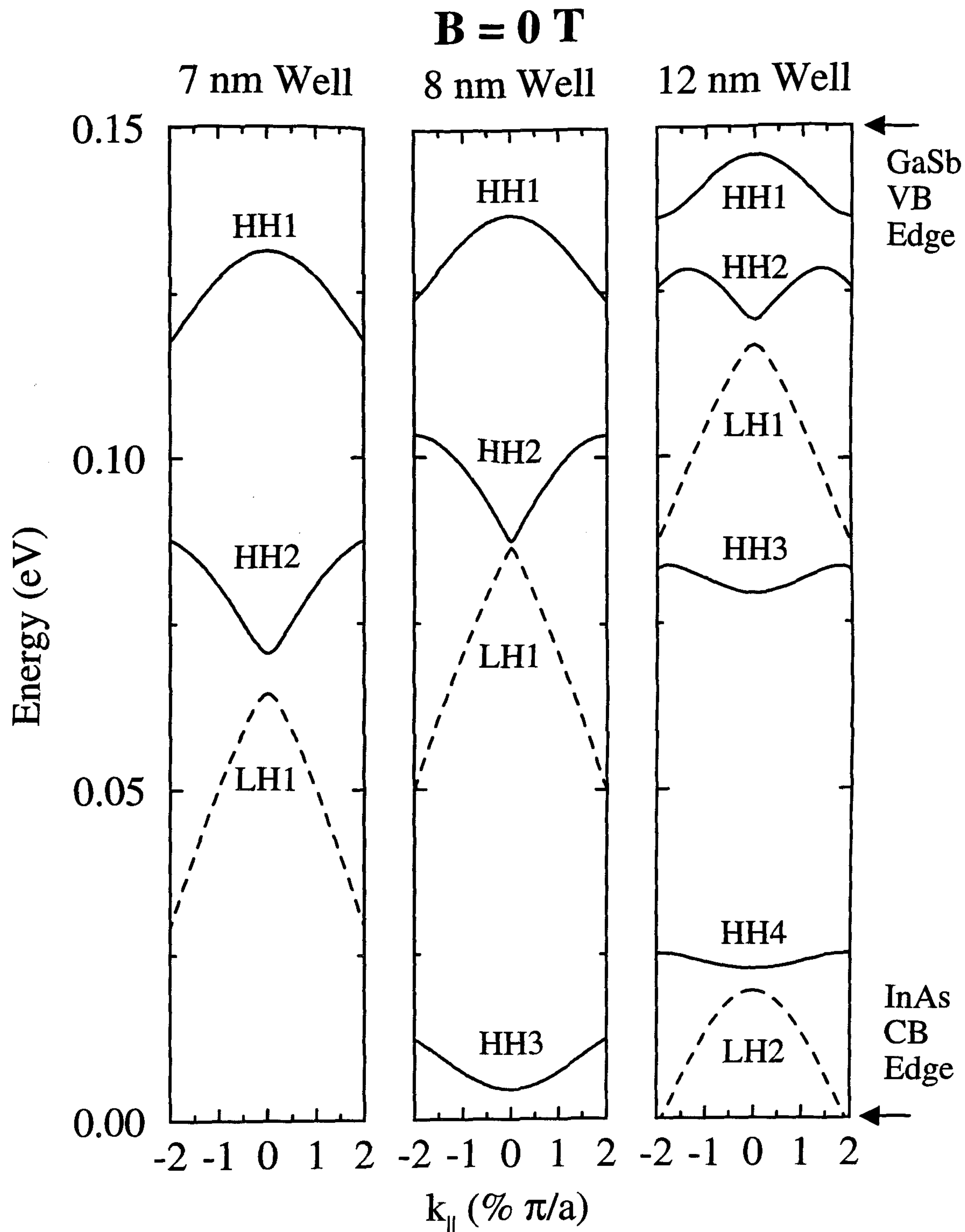

Figure 3.3: Hole subband dispersions for RIT devices having GaSb well widths of 70Å, 80Å, and 120Å, respectively. The energy range is chosen between the InAs conduction-band edge and GaSb valence-band edge.

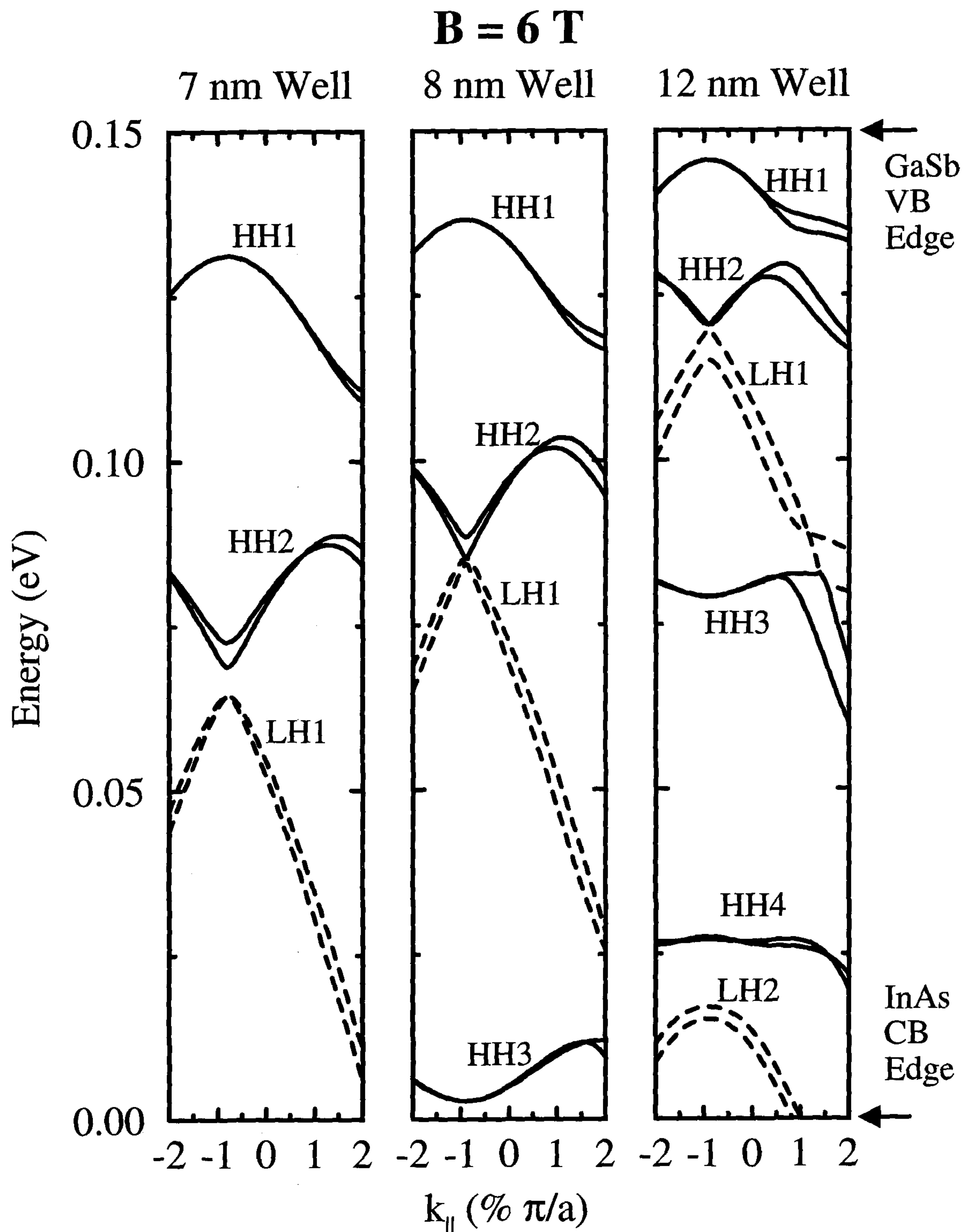

Figure 3.4: Hole subband dispersions for RIT devices having GaSb well widths of 70Å, 80Å, and 120Å, respectively, at a magnetic field of 6.0T. The magnetic field induces splitting between the spin-up and spin-down subbands, and also increases the hole mixing effects and interactions among subbands

different values of applied transverse magnetic field B. Fig. 3.3 shows that three quasi hole-subbands are formed in the GaSb well of 70Å thickness. At $B = 0$, the normal incident electrons from InAs conduction-band only interact with the light-hole states in the GaSb well, resulting in a single light-hole transmission resonance peak. At $B \neq 0$, two additional heavy-hole resonances are exhibited. As indicated by Eq. (3.4), the applied transverse magnetic field lends an in-plane momentum to the incident electron, which induces the coupling between electrons and heavy-hole states by the $k_y' p_y$ component in the Hamiltonian. As the applied B field strength increases, the resonance widths broaden, indicating stronger coupling between the electron states and hole states. Also the LH1 peak position shifts to lower energy, while the HH2 peak position shifts to higher energy, consistent with the subband dispersions in Fig. 3.3. The transmission probability comes mostly from LH1 and HH2 resonances. As the B field increases, the contributions from these resonances become comparable to each other.

3.3.3 Current-Voltage Characteristics

The RIT device in our calculation consists of 70Å GaSb well and 15Å AlSb barrier width. The doping concentration in the InAs electrodes is $n = 10^{17}/\text{cm}^3$ and temperature is $T = 77K$. The choice of thin barrier layer in our calculation is to reduce the heavy computational demands in the $I - V$ calculation. The calculated results are shown in Fig. 3.6. Experimental $I - V$ curve for a RIT device of similar structure except for the difference of 40Å AlSb barrier is also shown in Fig. 3.7. The calculated results bear a strong resemblance to the experimental $I - V$ characteristics and show several important features observed in the experimental data. The peak current density decreases as the magnetic field increases. Classically this is explained by the magneto-resistance effect. Quantum mechanically, it can be understood by examining the transmission coefficient in Fig. 3.5. The magnetic field effectively adds additional potential barrier (parabolic form in

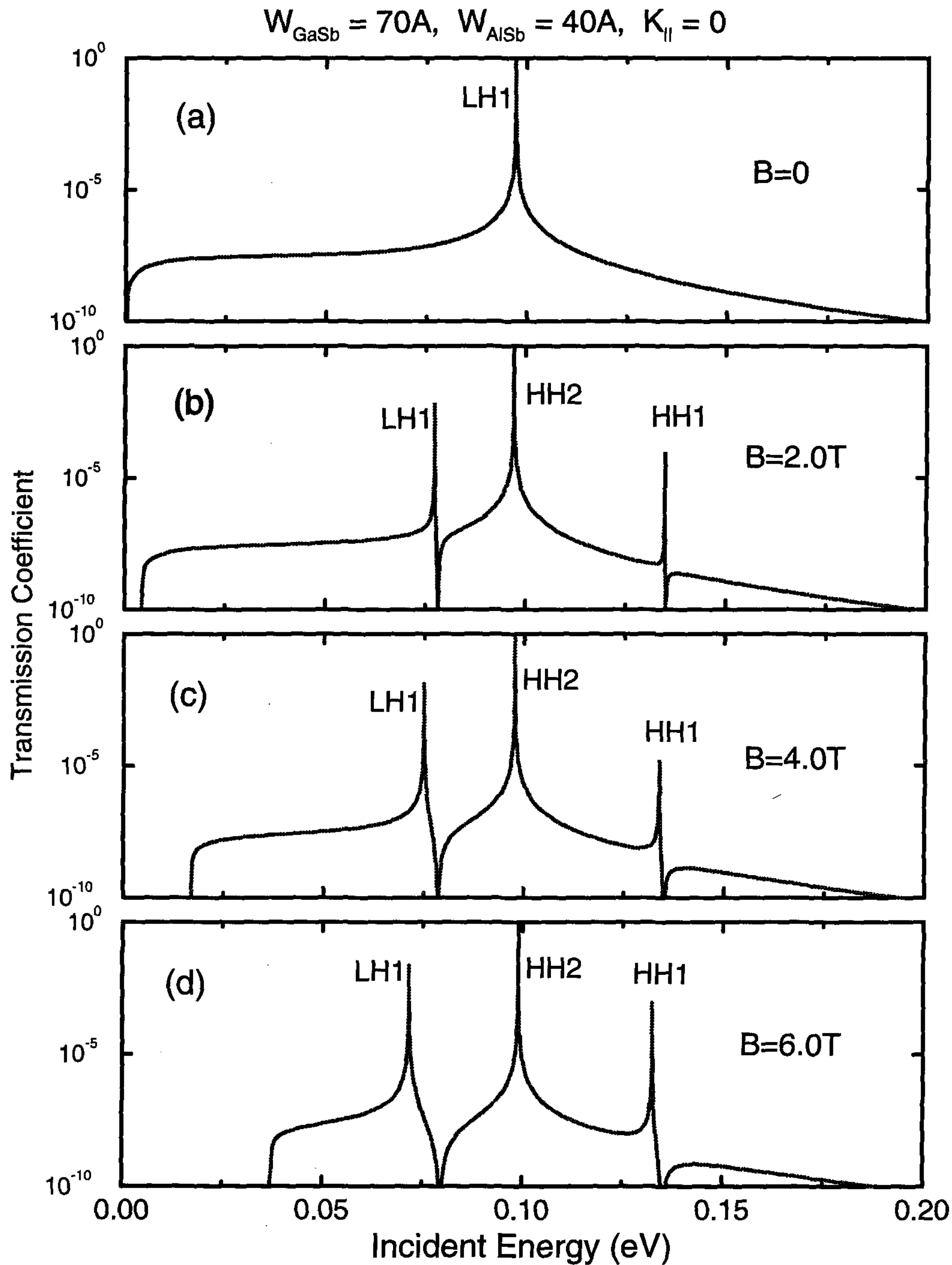

Figure 3.5: Calculated transmission coefficients for a RIT structure with a 70Å GaSb well width and 40Å AlSb barrier, at zero, 2.0, 4.0, and 6.0 tesla. At non-zero fields, additional heavy-hole resonances are present in additional to the LH1 resonance found at $B = 0$.

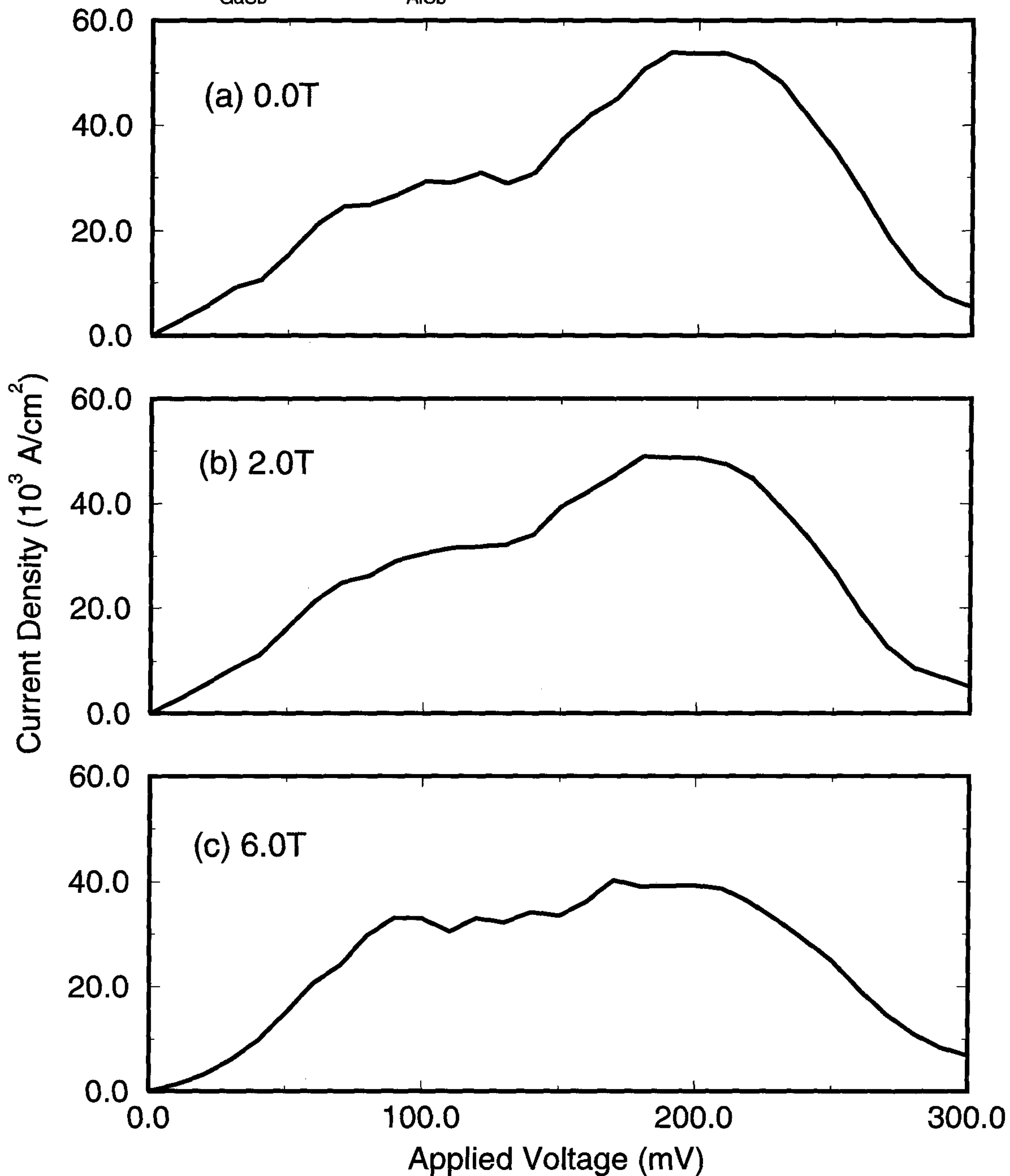

Figure 3.6: Calculated current-voltage characteristics for a p-well RIT device in zero, 2.0, and 6.0 tesla magnetic fields. The calculation is done for $T = 77K$, and a device having a 70Å-wide GaSb well and 40Å-wide AlSb barrier. The doping level in the InAs electrodes is $n = 10^{17}$ cm^{-3}.

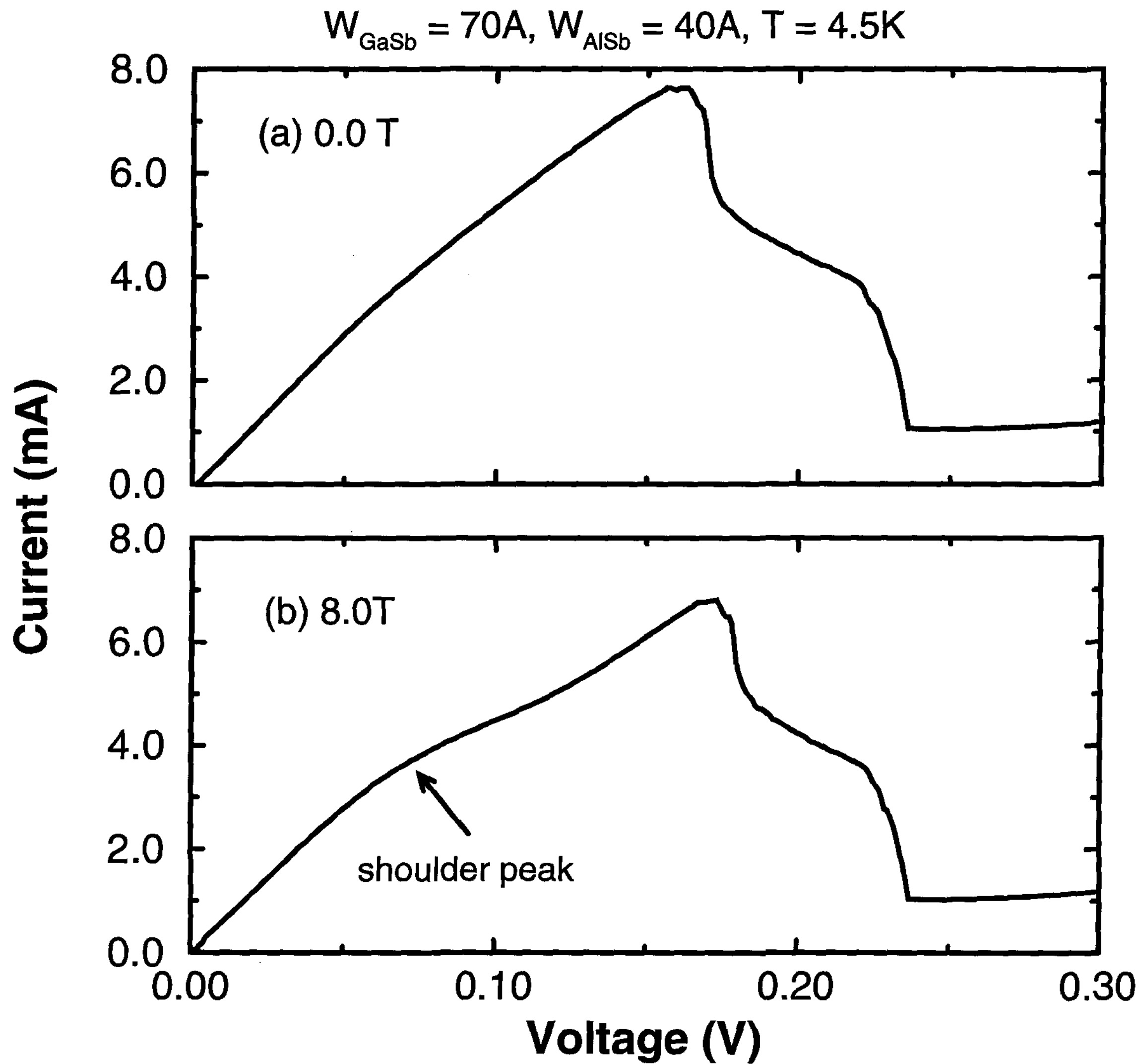

Figure 3.7: Measured current-voltage curves for a p-well RIT device at (a) 0.0T, and (b) 8.0T. The device consists of a 70Å-wide GaSb well and 40Å-wide AlSb barrier. The present of magnetic field reduces the peak current and develops a shoulder at lower bias.

one-band model) to the device. As the B field increases, only the electrons with certain minimum cut-off energy could tunnel through the device. This minimum cut-off energy increases as the B field increases. The effective electron population contributing to the current is thus reduced.

The main peak in the $I-V$ curve appears at about 200 meV, and the position remains relatively unchanged as the magnetic field increases. A shoulder peak is exhibited below the main peak at about 70 meV, and become more pronounced as the B field increases. We attribute the two peaks occurred in the $I-V$ curve to HH2 and LH1 resonances, respectively, as seen in the transmission coefficients. The shoulder peak is not evident for $B=0$ in the experimental $I-V$ curve, also not shown as strong in the experimental data as our calculation indicates. These differences are considered to be caused by the fact that thick AlSb barrier results in narrower transmission resonances, which are more easily to be washed out by the inelastic scattering processes neglected in our calculations.

3.4 Barrierless Resonant Interband Tunneling (BRIT) Structures

In contrast to RIT structures, in which resonant tunneling occurs via quasi-bound states localized by the AlSb barrier, quasi-bound hole states in the BRIT structures are formed in the GaSb layer due to the imperfect matching of InAs conduction–band and GaSb valence–band wave functions at the two InAs/GaSb interfaces. Consequently, resonant transport in this device can occur despite the absence of classically forbidden barrier regions.

3.4.1 Transmission Coefficients

The BRIT structure under consideration consists of a GaSb quantum well of 70Å thickness. Fig. 3.8 shows the calculated transmission coefficients for several dif-

ferent values of magnetic fields under flat-band conditions. At $B = 0$, only the light-hole states in the GaSb well interact with the normal incident electrons from InAs conduction-band, resulting in a single light-hole transmission resonance peak. Since the formation of the quasi-bound state does not involve any barriers, the transmission resonance width is rather broad — $\Delta E \approx 60$ meV, corresponding to an intrinsic quasi-bound state lifetime of ~ 10 fs.

For $B \neq 0$, two additional narrow heavy-hole resonances are exhibited as a result of induced coupling between the electron states and heavy-hole states by the magnetic field. The transmission probability comes mostly from light-hole resonance. However, as the applied B field increases, the light-hole transmission probability decreases, meanwhile the heavy-hole resonance widths broaden, indicating stronger coupling between the electron states and heavy-hole states.

3.4.2 Current-Voltage Characteristics

The calculated current-voltage characteristics for the BRIT structure under various B fields at $T = 77$K are shown in Fig. 3.9. The broad light-hole transmission resonance contributes mostly to the resonant tunneling current, and the high current density. A shoulder at 100 mV above the peak at $B = 0$ is attributed to the heavy-hole resonances. As the B field increases, the peak current decreases, meanwhile the shoulder peak becomes more pronounced. This phenomenon is attributed to increasing contributions from the heavy-hole resonances due to magnetic field. Again, our present calculation includes only elastic tunneling currents; in an actual device where inelastic scattering processes also contribute to the current, the heavy-hole shoulder would be interpreted as a part of the valley current.

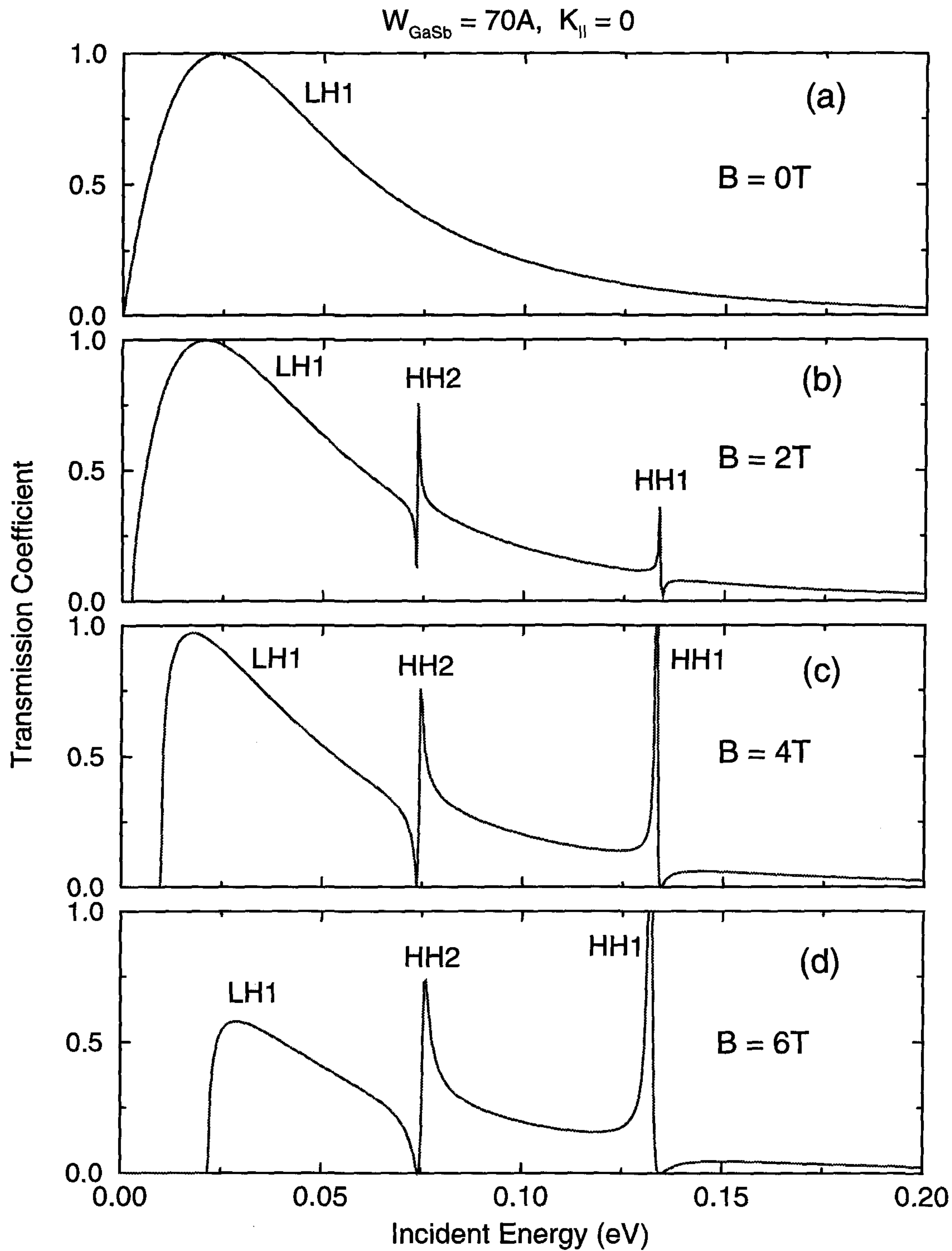

Figure 3.8: Calculated transmission coefficients for a BRIT structure with a 70Å GaSb well width, at zero, 2.0, 4.0, and 6.0 tesla. At non-zero B fields, additional narrow heavy-hole resonances are present in additional to the broad LH1 resonance found at $B = 0$.

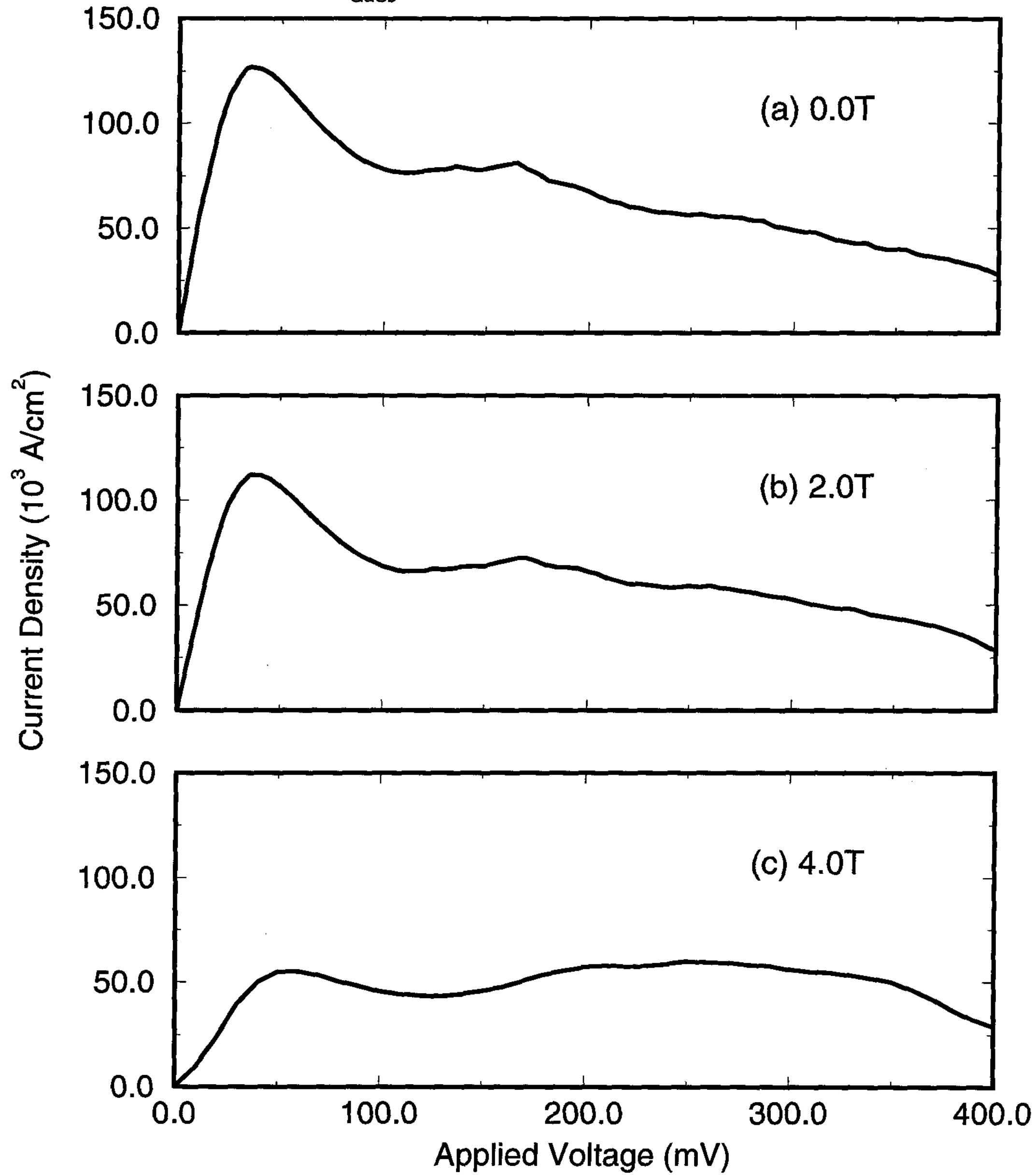

Figure 3.9: Current-voltage characteristics for the InAs-GaSb-InAs structure calculated for a series of B fields. The width of GaSb well is 70Å, and the doping level in the InAs electrodes is $n = 10^{17}$ cm^{-3}.

3.5 Discussions

We have limited our study of magnetotunneling to the case where the external magnetic field is perpendicular to the transport direction. In this set-up, the solutions to the effective mass Schrödinger's equation remain to be one-dimensional problem by choosing proper gauge for vector potential. The calculations of current density involve first solving a large system of linear equations ($8N$), typically on the order of a few thousands, to obtain the transmission coefficients, and then integrating over the incident electron states in energy and 2-D $\mathbf{k}_{\parallel}$ space to obtain current density. Tremendous computational power is needed to conduct the $I-V$ calculation. On IBM RS/6000 590 workstations, one of the fastest workstations available today, it took an average of 8 hours to obtain just one point on the $I-V$ curve. This enormous computational demand limits us from studying other interesting configuration of magnetic field alignment. For example, in the case when magnetic field is applied parallel to the transport direction, Landau levels with different cyclotron frequencies are expected to form in both the GaSb quantum well and InAs electrodes[17, 18]. Because the tunneling process involves both electron states and hole states, and the valence-band quantum well confinement induces considerable mixing between heavy-hole and light-hole states, the Landau level index is not conserved in interband magnetotunneling. Rigorous theoretical treatment of Landau level mixing effects requires extending the effective mass Schrödinger's equation to two-dimension, parallel as well as along the transport direction. Although the finite-difference method described in chapter 2 can be generalized to two-dimensional case, the computational cost is beyond our current limit.

3.6 Summary

We have applied the technique developed in chapter 2 for efficient and numerically stable multiband **k·p** treatment of quantum tunneling to the study of InAs/GaSb/AlSb based interband tunnel structures. Eight-band **k·p** model is employed in the calculations. We specifically investigate the effect of transverse magnetic field on the transport processes in the resonant interband tunneling (RIT) structures and barrierless resonant interband tunneling (BRIT) structures. It is found that resonances from different valence subbands in the GaSb well contribute differently to the tunneling current. The primary contribution comes from light-hole resonance. The applied magnetic field increases the coupling between the electron states in the InAs conduction-band and heavy-hole states in the GaSb valence-band, resulting in broader heavy-hole resonances. The heavy-hole effects are typically shown as a shoulder peak in the current-voltage characteristics, and the effects become more pronounced as the magnetic field strength increases. These calculated results agree well with the experimental data.

Bibliography

[1] *Molecular Beam Epitaxy and Heterostructures*, proceedings of the NATO Advanced Study Institute on Molecular Beam Epitaxy (MBE) and Heterostructures, Erice, Italy, edited by L. L. Chang and K. Ploog (Martinus Nijhoff, Dordrecht, 1985).

[2] R. K. Hayden *et al.*, *Phys. Rev. Lett.* **66**, 1749 (1991).

[3] J. P. Eisenstein, T. J. Gramila, L. N. Pfeiffer, and K. W. West, *Phys. Rev. B* **44**, 6511 (1991).

[4] U. Gennser *et al.*, *Phys. Rev. Lett.* **67**, 3828 (1991).

[5] R. R. Marquardt, Y. X. Liu, D. Z.-Y. Ting, D. A. Collins, and T. C. McGill, *Proc. of Microscopic and Mesoscopic Systems*, Hawaii, (1994), to be published in *Phys. Rev. B.*

[6] J. R. Söderström, D. H. Chow, and T. C. McGill, *Appl. Phys. Lett.* **55**, 1094 (1989).

[7] L. F. Luo, R. Beresford, and W. I. Wang, *Appl. Phys. Lett.* **55**, 2023 (1989).

[8] R. Beresford, L. F. Luo, and W. I. Wang, *Appl. Phys. Lett.* **56**, 551 (1990); *Appl. Phys. Lett.* **56**, 952 (1990).

[9] K. Taira, I. Hase, and K. Kawai, *Electron. Lett.* **25**, 1708 (1989).

[10] D. A. Collins, E. T. Yu, Y. Rajakarunanayake, J. R. Söderström, D. H. Chow, D. Z.-Y. Ting, and T. C. McGill, *Appl. Phys. Lett.* **57**, 683 (1990).

[11] L. Yang, J. F. Chen, and A. Y. Cho, *J. Appl. Phys.* **68**, 2997 (1990)

[12] D. Z.-Y. Ting, D. A. Collins, E. T. Yu., D. H. Chow, and T. C. McGill, *Appl. Phys. Lett.* **57**, 1257 (1990).

[13] J. R. Söderström, E. T. Yu, M. K. Jackson, Y. Rajakarunanayake, and T. C. McGill, *J. Appl. Phys.* **68**, 1372 (1990).

[14] D. Z.-Y. Ting, E. T. Yu, and T. C. McGill, *Phys. Rev. B* **45**, 3583 (1992).

[15] J. M. Luttinger, *Phys. Rev.* **102**, 1030 (1956).

[16] C. B. Duke, *Solid State Physics*, Suppl. 10, *Tunneling in Solids* (Academic Press, New York, 1969).

[17] E. E. Mendez, H. Ohno, L. Esaki, and W. I. Wang, *Phys. Rev. B* **43**, 5196(1992).

[18] R. R. Marquardt, *Quantum Magnetotransport Studies of Semiconductor Heterostructure Devices*, Ph.D thesis, California Institute of Technology, Pasadena, CA (1994).

Chapter 4

Schottky Barrier Induced Injecting Contact on Wide Bandgap II-VI Semiconductors

4.1 Introduction

Wide bandgap II-VI semiconductors have great potential for applications as optoelectronic materials in the short wave visible light regions. However, there are two major technological challenges in the effort of making blue and green light emitting devices based on wider bandgap II-VI semiconductors. One problem is difficult to dope them both *n*-type and *p*-type, where selective doping is almost always compensated by opposing charges, arising from defects, impurities or more complex entities[1]. The other problem is difficult to make ohmic contact to them. Ohmic contact requires either low Schottky barrier height formed between metal and semiconductor, or high doping concentration in the semiconductor. A metal with low Schottky barrier height does not generally exist for wide bandgap II-VI materials to allow thermionic injection. For tunneling injection, typical Schottky barrier heights ϕ_B observed, for example $\phi_B = 1.35$ eV for Au/n-ZnTe and $\phi_B =$

1.28 eV for Au/p-ZnSe [2], require that doping concentration should be well above 10^{19} cm^{-3}. Doping levels this high have not been reported.

Alternative scheme such as using heterojunction made up of highly doped p-type and n-type materials has been proposed[3, 4]. But the problem of making good ohmic contact to these materials still remains an important issue. In this chapter, we propose a new and very novel way of obtaining high doping levels in the contact region by minority carrier injection. The basic principle is to use a forming process, i.e. an applied electric field at an elevated temperature in the Schottky contact, to spatially separate dopants from compensating centers. In this way, the ratio of dopants to compensating centers can be greatly increased at the semiconductor surface. Upon cooling, the dopant concentrations are frozen to retain a large net concentration of dopants in a thin surface layer, resulting in a depletion layer that is sufficiently thin to allow tunneling injection.

In section 4.2, we give a detailed description of our proposal. Al doped ZnTe is used as the example. Calculations of band profiles, distributions of doping concentrations, and current-voltage characteristics are described. In section 4.3, we perform the calculations on Al doped ZnTe, and discuss the various important issues for achieving injecting contacts. Comparison with experiment is also presented. Finally, a summary is given in section 4.4.

4.2 Proposal and Calculation

The problem in making ohmic contacts to wide bandgap materials can be understood very simply in terms of the standard model of the ohmic contact [5]. An ohmic contact is produced by defeating the Schottky barrier typically existing between a metal and a semiconductor. This is done by doping the barrier region sufficiently heavily to produce a very short depletion region that allows tunneling. For barrier heights as high as the ones found for wide bandgap II-VI compounds, the doping concentration necessary is typically well above 10^{19} cm^{-3}. Doping lev-

els this high have not been reported for bulk n-ZnTe and p-ZnSe. For example, observed doping levels for p-ZnSe saturate at roughly 10^{18} cm^{-3}. The metastable nature of these successful doping schemes makes the possibility of obtaining much higher levels somewhat in doubt.

The method we propose consists of forming the device structure in an electric field at elevated temperatures, to spatially separate the ionized dopants from the compensating centers. In this way, the ratio of dopants to compensating centers can be greatly increased at the semiconductor surface. Upon cooling, the dopant concentrations are frozen to retain a large net concentration of dopants in a thin surface layer, resulting in a depletion layer that is sufficiently thin to allow tunneling injection.

The basic idea we use here is very simple, as illustrated in Fig. 4.1. In this figure, we have illustrated the model for the case of Al doped ZnTe, where the Al on a Zn site would be a donor. However, it is thought that an Al donor in ZnTe is usually complexed by a native doubly negative ionized Zn vacancy to form an "A-center" which acts as an acceptor to produce the total compensation[6, 7]. This situation is illustrated in Fig. 4.1a.

The forming process consists of heating the device structure to a temperature where one of the centers is mobile. Whether the actual mobile species is the V_{Zn}^{-2} or the singly ionized A center is not clear. This might depend on many factors, such as the dissociation energy of the A center, the temperature and the strength of the electric field, etc. However, we will see that the key results based on our model are insensitive to this nature of the mobile species. For the example illustrated here, we have selected the V_{Zn}^{-2} as the mobile species, as shown in Fig. 4.1b. The presence of an electric field at this elevated temperature will result in the motion of Zn vacancies inside the crystal. We assume that no additional Zn vacancies enter the crystal from the Zn contact. As noted, the charged vacancies move in the electric field in such a way as to produce a highly doped depletion region as shown in Fig. 4.2. That is, if one of the dopant centers is mobile at the elevated

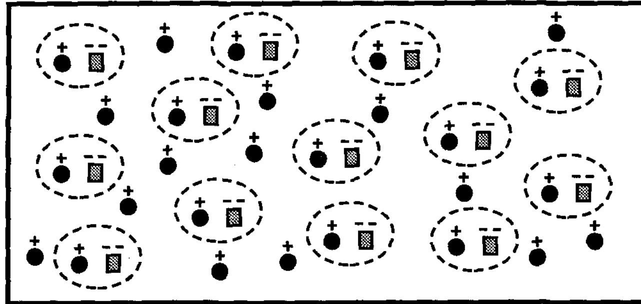

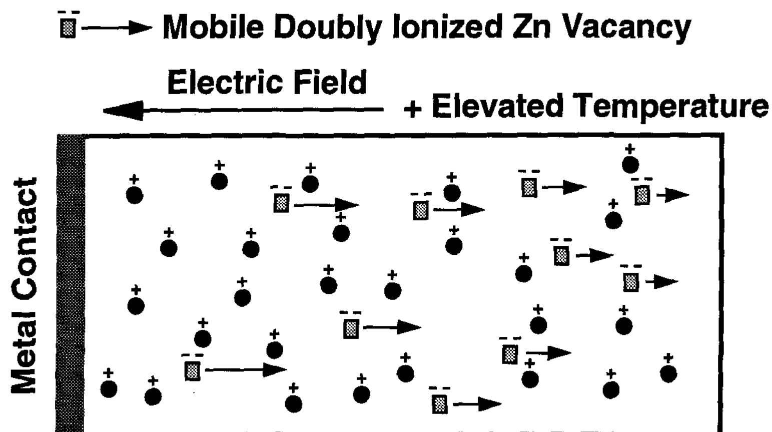

Figure 4.1: Schematic of the forming process. The figure illustrates the case of doping of ZnTe by Al. The Al donor is usually complexed by a native doubly negative ionized Zn vacancy V_{Zn}^{-2} to form an "A-center" which acts as an acceptor. The unformed sample is shown in the upper panel labeled a. The forming process is illustrated in the lower panel labeled b. The Zn vacancies are assumed to be the mobile species which are shown to be moving at the elevated temperature under the influence of the electric field in the semiconductor produced by the Schottky barrier and perhaps an additional applied potential.

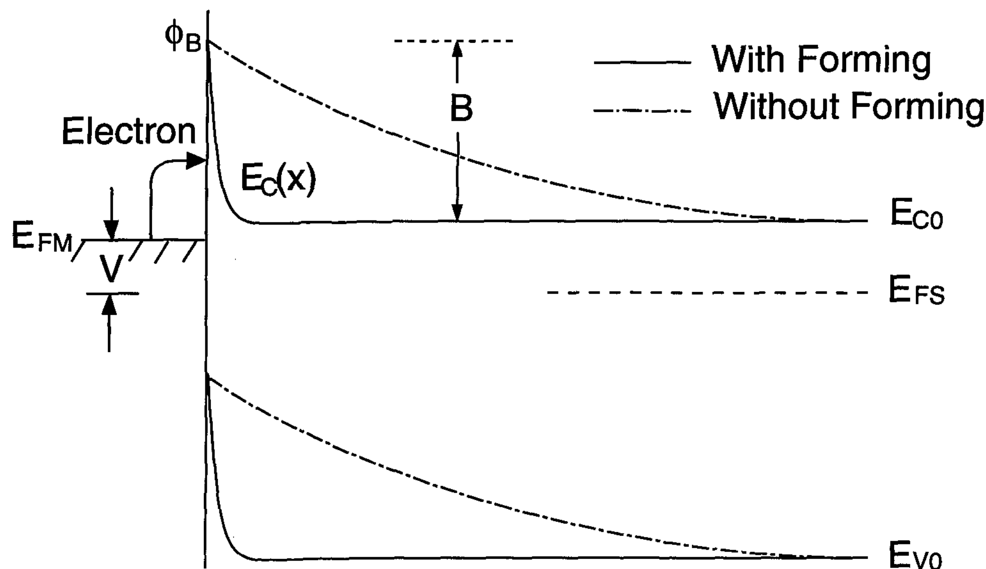

Figure 4.2: The energy diagram of the metal-semiconductor interface before and after the forming process. Before the forming process, the nearly perfect self-compensation results in a very lightly doped bulk where the depletion layer is very thick. After the forming process, the self-compensation is not as effective resulting in a very heavily doped region near the surface and a very thin depletion layer.

temperature, then the field produced by the Schottky barrier and perhaps an additional applied potential produces a highly doped region with a very narrow depletion width. This depletion region, if thin enough, can result in substantial injection current or an "ohmic contact" to the previously highly self-compensated material.

Most of the important parameters governing the calculations are given in Fig. 4.2. The important energy parameters are the Schottky barrier height, ϕ_B,

the Fermi energy in the metal, E_{FM}, the Fermi energy in the semiconductor, E_{FS}, which depends on the net doping in the semiconductor, the applied potential ,V, and the location of the conduction band edge in the bulk semiconductor where the bands are flat, E_{C0}. The driving term for the forming process is

$$B = \phi_B - E_{C0}, \tag{4.1}$$

the total band bending across the semiconductor layer. The semiconductor is taken to be nearly fully self-compensated, but with a small net carrier concentration of n_e.

The calculation of the charge rearrangement during the forming process assumes that mobile centers can move and establish thermal equilibrium at the elevated temperatures. The calculations are similar to those reported in Ref.[3]. The density of the non-mobile charge centers is assumed to be capped at the original level, N_D, throughout the process. The final density of mobile centers is taken to be given by

$$N_V = N_S \exp\left(\frac{-2q(E_C(x) - E_{C0})}{k_B T_f}\right), \tag{4.2}$$

where N_V is the density of doubly ionized Zn vacancy, N_S is the density of V_{Zn}^{-2} away from the interface, $E_C(x)$ is the conduction band edge as a function of position in the semiconductor, and T_f is the forming temperature. The band profile $E_C(x)$ and the mobile dopant distribution at forming are obtained by solving Poisson's equation:

$$\frac{d^2 E_C(x)}{dx^2} = \frac{q}{\epsilon_0 \epsilon}\left(N_D - 2N_V + p - n\right) , \tag{4.3}$$

where ϵ is the dielectric constant, n and p are the electron and hole concentrations respectively.

We assume that the equilibrium distribution of V_{Zn}^{-2} at forming conditions is fixed after cooling to the operating temperature T_m, typically room temperature. Poisson's equation is then solved again to produce the barrier shape with the non-uniform dopant concentration. The current-voltage characteristics at the operating

temperature are calculated using a model that includes thermionic emission over the barrier, field induced emission through the barrier as well as straight tunneling [5]. The basic equation in this model is

$$J = \frac{qm_c k_B T_m}{2\pi^2 \hbar^3} \int_{E_{CO}}^{\infty} dE\, T(E) \ln \left(\frac{\exp[-(E - E_{FM})/k_B T_m] + 1}{\exp[-(E - E_{FS})/k_B T_m] + 1} \right), \tag{4.4}$$

where $T(E)$ is the transmission coefficient calculated for the barrier shape given in Fig. 2 using the WKB approximation and two-band $k \cdot p$ model. The applied bias is $V = E_{FM} - E_{FS}$.

4.3 Study of Al Doped ZnTe

We apply the calculations to Al doped ZnTe. The results of these calculations are shown in Figs. 4.3 – 4.5. In Fig. 4.3, we present the compensating vacancy distribution for an Al doping concentration of $N_D = 10^{20}$ cm^{-3}. The calculations have been performed for the four different combinations of the parameters B (=1.5, 1.0 eV) and n_e (=10^{12}, 10^8 cm^{-3}). Fig. 4.3 illustrates a number of important points. First, the mobile V_{Zn}^{-2} distributions depend only on the value of B and not the bulk doping value. However, it should be noted that the applied voltage required to maintain the same value of B depends on the background doping in the bulk through the variation of the E_{FS} with doping. Second, the vacancy distribution dips to a very low level for both values of B. This low concentration of vacancies basically exposes all of the dopant atoms, leading to large concentrations of ionized donors.

As expected, these ionized donors make a substantial change in the current voltage characteristic of the resulting device structure at room temperature. The current-voltage characteristic is shown in Fig. 4.4 for the case of an Al concentration of 10^{20} cm^{-3} and a V_{Zn}^{-2} concentration of 5×10^{19} cm^{-3}. In this figure we have a number of different current-voltage characteristics. The lowest current is obtained before the forming. Four different cases are shown after the forming process,

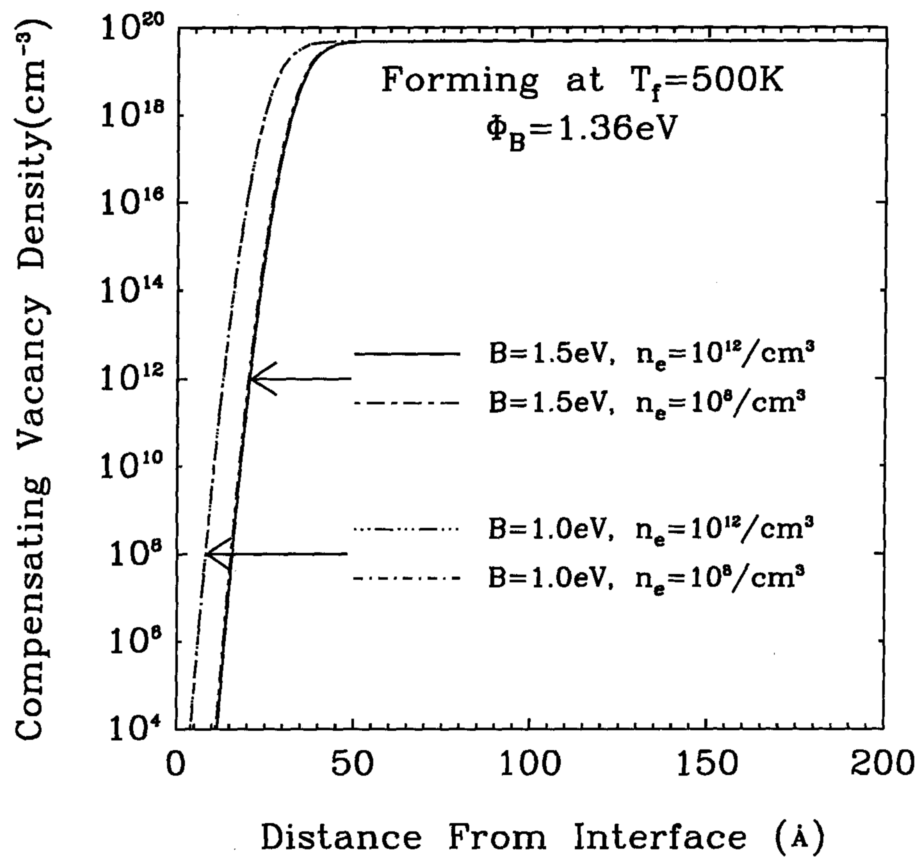

Figure 4.3: The computed density of vacancies as a function of distance from the metal-semiconductor interface. The curves are parameterized by the electron density far into the bulk of the material n_e and the total band bending B. The forming temperature is taken to be 500K and the Schottky barrier height to be 1.36 eV.

B (=1.5, 1.0 eV) and n_e (=10^{12}, 10^8 cm^{-3}). As can be seen from the figure, the current densities have been greatly enhanced after the forming treatment. The largest values of the current are obtained for the highest values of B and background doping, n_e. For light emitting diodes, current densities in excess of roughly 10 amp/cm^2 are required at relatively small voltage drops, typically less than 1 volt. For lasers, 100 amp/cm^2 are required at less than 1 volt. As can be seen from Fig. 4.4, only a few cases of doping and forming potential satisfy this criteria.

Since heavy doping of most of these systems is quite difficult, one might ask what effect reducing the doping concentration will have on these results. In Fig. 4.5, we have plotted the results for an Al dopant concentration of 10^{19} cm^{-3} and a background concentration of V_{Zn}^{-2} of 5×10^{18} cm^{-3}. As can be seen from these results, the currents under similar circumstances of background doping and bias during forming are substantially reduced. In fact, the current densities for all of the voltages of interest are sufficiently small that the contact would not be useful for light emitting devices. The large decrease in current densities is due to the increase in the depletion layer width in going from an Al concentration of 10^{20} cm^{-3} to 10^{19} cm^{-3}.

In our calculation, we have assumed that the mobile centers are doubly ionized under the forming treatment, for which we included the factor of 2 in equations (4.2) and (4.3). Since the details of the mobile species are not clear, it is important to see the effect of assuming that the mobile species is instead the singly ionized A-center in the case when the bonding between the V_{Zn}^{-2} and the Al donor is strong. Fig. 4.6 shows the comparisons of doubly and singly ionized compensating mobile charge distributions and the corresponding current-voltage characteristics. The results indicate that although the charge distributions near the surface depend on the mobile charge, the depletion widths are insensitive to the assumption, thus resulting in approximately the same band profile near the contact surface which gives rise to almost identical current-voltage characteristics. Therefore, the results

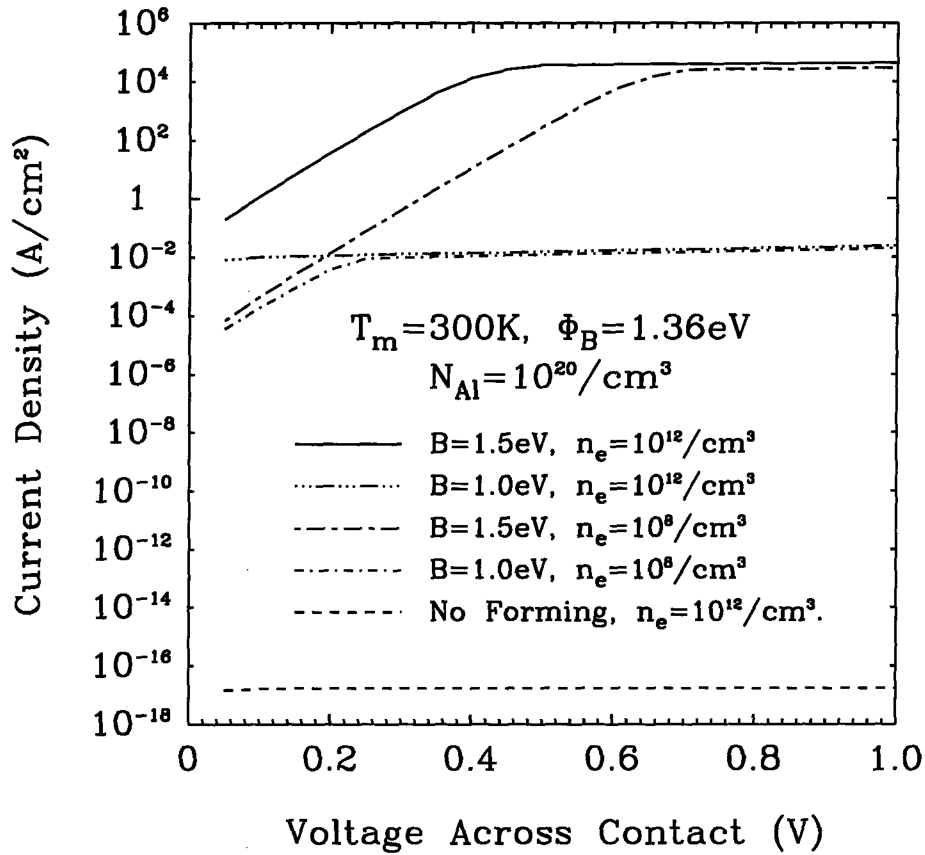

Figure 4.4: The current density as a function of applied bias for the unformed and formed devices at 300K operating temperature. The concentration of Al is taken to be 10^{20} cm^{-3}. The current-voltage characteristic is parameterized by the total band bending potential in the semiconductor during the forming B and the background net doping level in the bulk n_e.

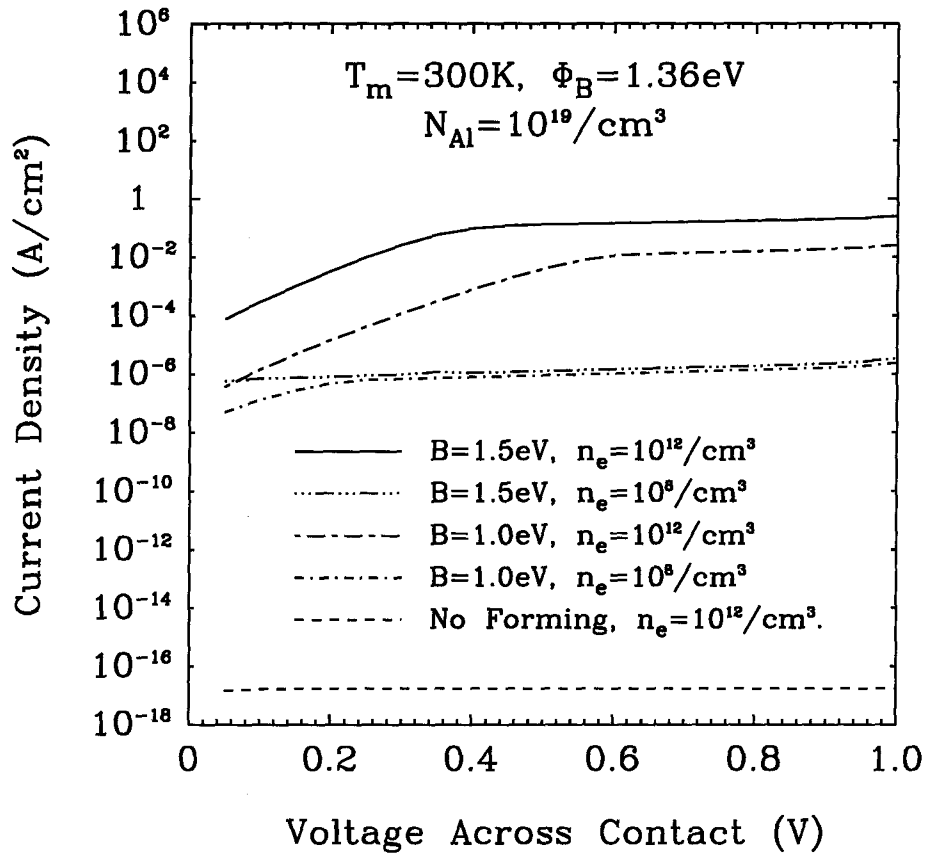

Figure 4.5: The current density as a function of applied bias for the unformed and formed devices at 300K operating temperature. The concentration of Al is taken to be 10^{19} cm^{-3}. The current-voltage characteristic is parameterized by the total band bending potential in the semiconductor during the forming B and the background net doping level in the bulk n_e.

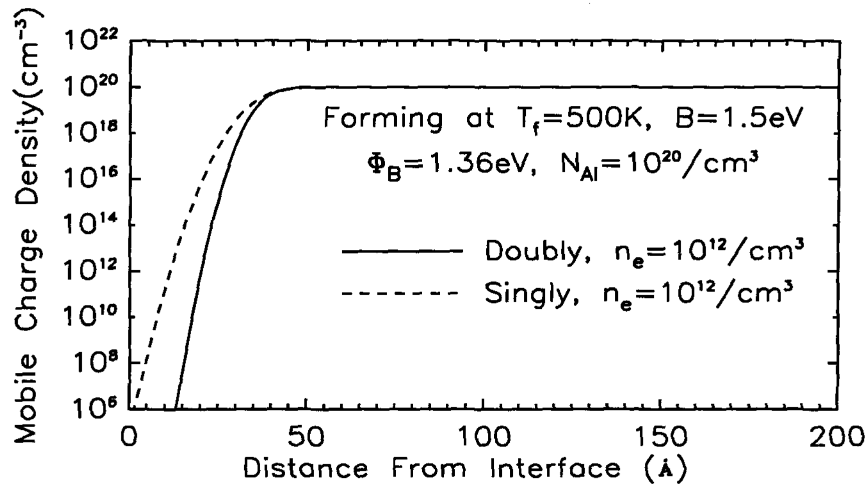

(a)

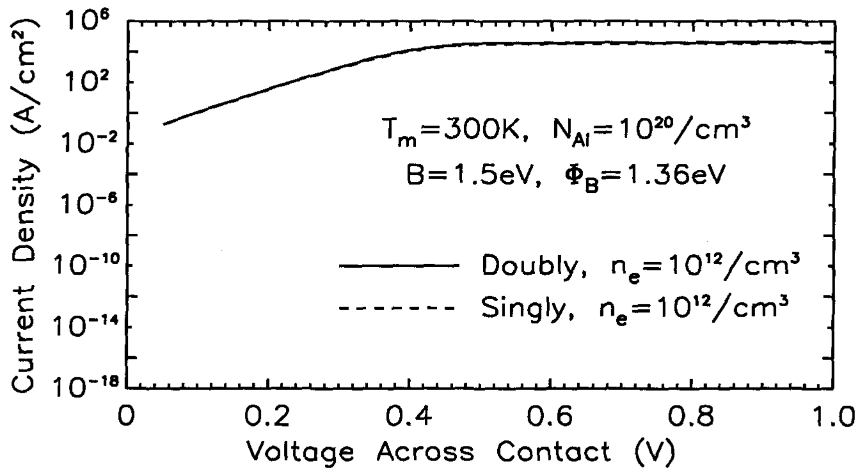

(b)

Figure 4.6: Comparisons of doubly and singly ionized mobile charge density distributions, (a), and the corresponding current-voltage characteristics, (b). The mobile charge density distributions shows the difference near the surface. However, the depletion widths are approximately the same, which results in almost identical I-V characteristics.

based on our model are independent of the charge of the mobile centers, as long as there exists a mobile charged species which can move and reach thermal equilibrium in the forming process.

Preliminary experiments have been performed to support that such forming effects do occur in ZnTe doped with Al [9]. The structure we studied in these experiments consisted of thin (generally 800 Å) layer of ZnTe doped with Al concentrations of $1.9\times10^{19}\text{cm}^{-3}$, grown on p-type ZnTe substrates. Zn was evaporated in the growth chamber onto the epilayer to form in situ contacts. Fig. 4.7 shows the effect of applying a 1.3 V bias at 210°C. The solid and dotted curves demonstrate that annealing at 210°C without a bias causes little change in the $I - V$ characteristics. The dashed line shows an increase in the current of up to three orders of magnitude after forming with a 1.3 V bias for 25 minutes. Forming voltages less than about 1.2 V do not change the $I - V$ significantly. It should be noted that the current in the devices used in the experiments contains both the injected electron current and hole current extracted from the p-type substrate. A direct comparison between the experimental results and the theoretical calculations is difficult.

4.4 Summary

In summary, we have proposed a novel method of obtaining a heavily doped layer for the wide bandgap semiconductors in which heavy doping is self-compensated. Using a forming process (elevated temperatures and applied electric field), a mobile species such as a Zn vacancy can be separated from a donor such as Al, leaving behind a high density of uncompensated donors. These donors can substantially change the current-voltage characteristics for Schottky barriers, resulting in an ohmic or an injecting contact. The crucial factors in the forming process for achieving injecting contacts are the doping concentration and the total band bending during the forming process. For Schottky barrier heights above 1eV, doping

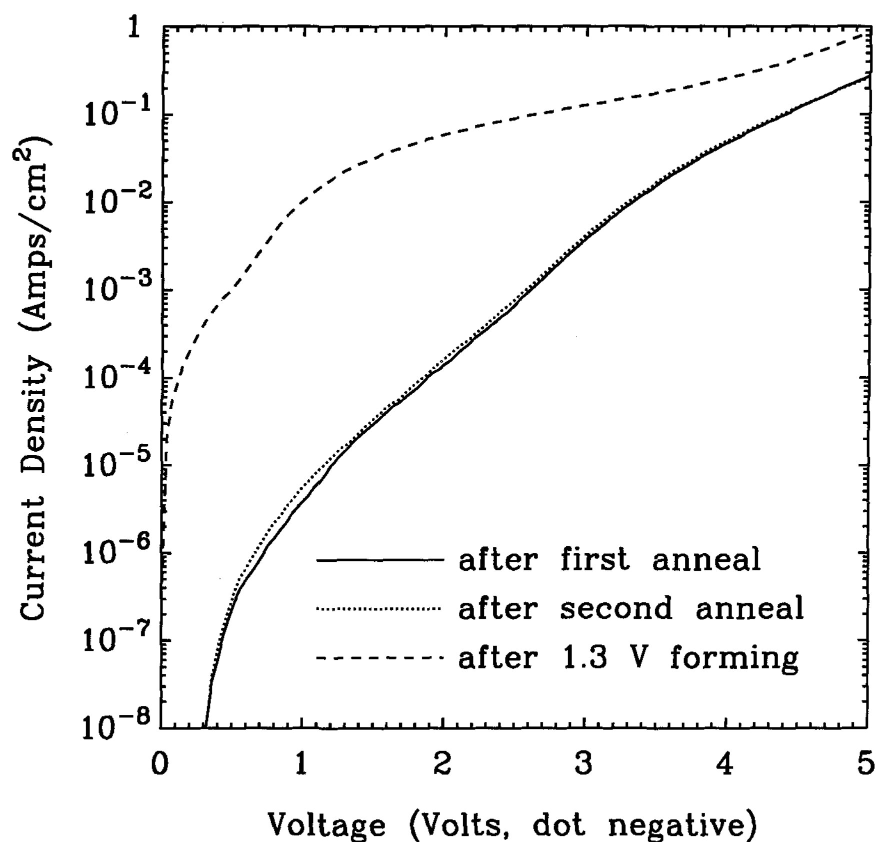

Figure 4.7: Measured $I - V$ characteristics before and after forming process. The solid curve is after annealing 1.5 hr at 210°Cto improve the back contact. The dotted curve shows very little change after another 1.5 hr at 210°C. The dashed curve shows the large change caused by applying 1.3 V bias for 25 min at 210°C.

concentrations as high as 10^{20} cm^{-3} are needed.

While the specific model and the calculations are presented for the case of ZnTe in which the donor is taken to be Al and the self-compensation mechanism consists of the pairing of two Al donors with the double acceptor produced by a Zn vacancy, one might envision the extension of this approach to produce injecting contacts or ohmic contacts to p-ZnSe. While in principle this method could work, the current doping schemes, doping with Li on a Zn sublattice or N on a Se sublattice, involve as yet unexplained self-compensation mechanisms. Basically, what is found is that increasing the Li or N concentrations does not lead to increased doping beyond roughly 10^{18} cm^{-3}. The saturation of doping levels may be due to the formation of electrically inert Li chalcogenides, which are very stable, or N pairs which are bound together by one of the strongest covalent bonds (roughly 9 eV). Hence, it may in fact be difficult to employ such a technique on p-ZnSe.

Bibliography

[1] J.O. McCaldin, *J. Vac. Sci. Technol. A* **8**, 1188 (1990).

[2] J. O. McCaldin, T. C. McGill and C.A. Mead, *Phys. Rev. Lett.* **36**, 56 (1976).

[3] F. Hiei, M. Ikeda, M. Ozawa, T. Miyajima, A. Ishibash, and K. Akimoto, *Electronics Letters* **29**, 878 (1993).

[4] M. C. Phillips, J. F. Swenberg, M. W. Wang, J. O. McCaldin, and T. C. McGill, *Physica B* **185**, 485(1993).

[5] W.J. Boudville and T.C. McGill, jvstb3, 1192 (1985).

[6] F.A. Kroger, *J. Phys. Chem. Solid* **26**, 1717 (1965).

[7] G. Mandal, *Phys. Rev.* **134**, A1073 (1964).

[8] Y. Rajakarunanayake, J. O. McCaldin and T. C. McGill, in: *Proc. 6th Intern. Conf. on Molecular Beam Epitaxy,* La Jolla, CA, 1990, *J. Cryst. Growth* **111**, 782 (1991).

[9] M. C. Phillips, J. F. Swenberg, Y. X. Liu, M. W. Wang, J. O. McCaldin and T. C. McGill, *J. Cryst. Growth* **117**, 1050 (1992).

Chapter 5

Excitons in Semiconductor Heterostructures

This chapter discusses excitons in semiconductor heterostructures and consists of two parts. In first part section 5.1, we will study excitons in two typical types of wide bandgap II-VI heterostructure systems, type I CdTe/ZnTe system and type II ZnTe/ZnSe system, and examine the roles of band alignment, strain and image charge at the interface on exciton binding energy and oscillator strength in these two model cases. The second part section 5.2 deals with exciton coherent transfer process in various low-dimensional structures, quantum wells, quantum wires and quantum dots.

5.1 Excitons in II-VI Heterostructures

5.1.1 Introduction

The II-VI semiconductor materials, with their wide and direct band gaps, have potential applications as optoelectronic materials in the visible light region. In quasi two-dimensional quantum well structures, it is known that excitons have larger binding energy and enhanced oscillator strength comparing with that in the

bulk, and they play an important role in various studies of optical properties[1]. Exciton has been reported responsible for the lasing conditions in ZnSe based laser diodes[2]. The band alignments in II-VI heterojunctions include not only the standard Type-I with very small valence band offset like CdTe/ZnTe but also the case of Type-II ZnTe/ZnSe, as shown in Fig 5.1. Both of these systems have shown fairly strong exciton luminescence[3]. The special band alignments and the intermediate values for the effective masses raise the interesting question of the role of the attractive interaction between the hole and electron on the binding energy and oscillator strength. In this section, we will study exciton properties in these two model systems.

5.1.2 CdTe/ZnTe Type I Heterostructure

The CdTe/ZnTe heterostructure is a strained system with 6.2% lattice mismatch. It is believed that the CdTe/ZnTe valence band offset without strain is small, obeying the common anion rule[4]. For CdTe/ZnTe heterostructure grown along [001] crystal orientation, the uniaxial strain will shift up the heavy hole valence band and shift down the light hole valence band in the well region, while in the barrier region the corresponding bands shift in opposite directions. The large strain can shift the band edges by approximately 200meV. Experiment indicates that under heavy strain, the band structure for "heavy-hole" excitons is Type-I, while for "light-hole" excitons it is Type-II[5]. The photoluminescence is primarily due to the free heavy-hole exciton recombination.

In our calculation, the strain induced band offset is explicitly included. A free standing superlattice model is used to determine the value of strain. Although the small valence band offset only gives rise to weak confinement to the heavy hole state, the Coulomb attraction force by the strongly confined electrons in the conduction band may play an important role for the localization of heavy holes in the well region. The variational approach developed by Wu *et al.*[6] for small band

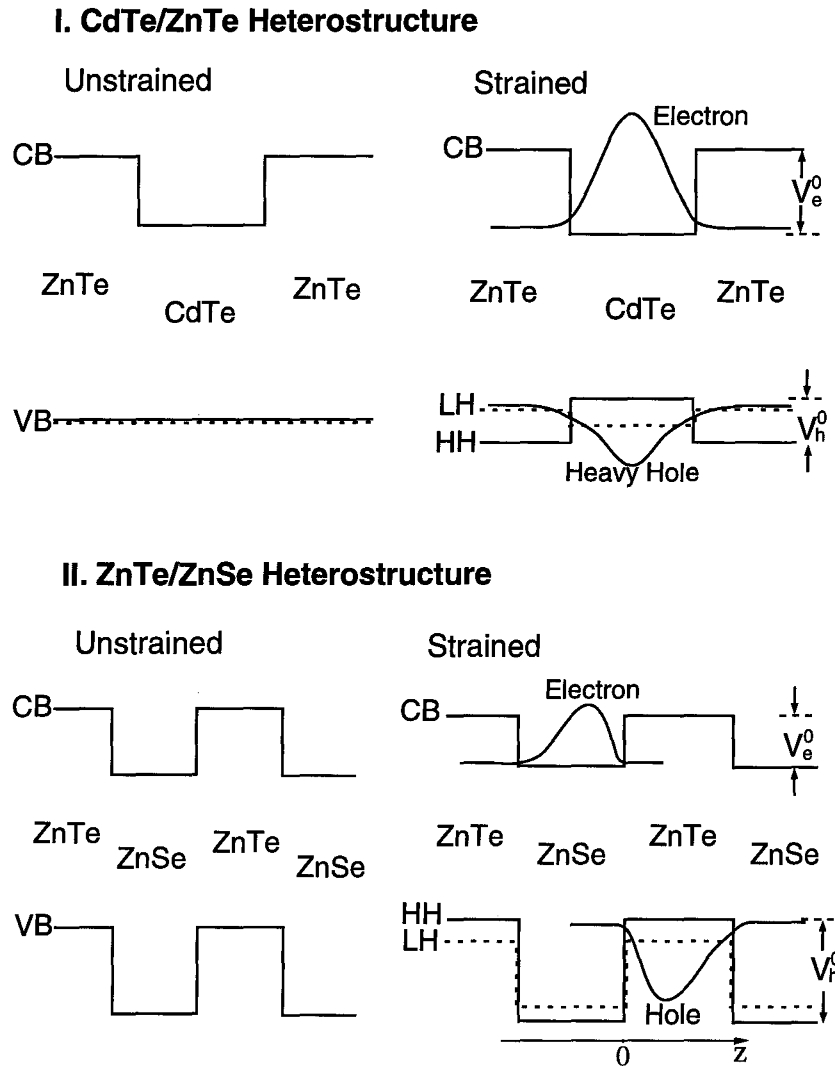

Figure 5.1: A schematic of the valence and conduction band edges in CdTe/ZnTe and ZnTe/ZnSe heterostructures. The conduction band and valence band are shown for both the strained and the unstrained cases. The valence band offset for the CdTe/ZnTe heterojunction without strain is small. Under strain the valence bands are split with the heavy-hole and conduction band forming a Type-I heterostructure and the light-hole and conduction band forming a Type-II. For ZnTe/ZnSe, the accepted values for the band offsets result in Type-II structures for both the strained and unstrained cases. The electron and hole wave functions making up the exciton are hence in different layers.

offset systems is applied to calculate the exciton binding energy in the CdTe/ZnTe system.

The Hamiltonian of the exciton system in the effective mass approximation can be written as

$$\begin{aligned} H_{\rm ex} &= \left(-\frac{\hbar^2}{2m_e}\frac{\partial^2}{\partial z_e^2} + V_e^0(z_e)\right) + \left(-\frac{\hbar^2}{2m_{z,h}}\frac{\partial^2}{\partial z_h^2} + V_h^0(z_h)\right) \\ &+ \frac{p_\parallel^2}{2\mu_\parallel} - \frac{e^2}{\epsilon[r_\parallel^2 + (z_e - z_h)^2]^{1/2}} \ , \end{aligned} \tag{5.1}$$

where m_e is the electron effective mass, $m_{z,h}$ is the heavy hole mass along the growth [001] direction, $\mu_\parallel$ is the reduced effective mass of heavy hole excitons in the plane of the well, $p_\parallel$ is the relative momentum in the plane of the well, and ϵ is the static dielectric constant. $m_{z,h}$ and $\mu_\parallel$ are given by[7]

$$\begin{aligned} m_{z,h} &= \frac{m_0}{\gamma_1 - 2\bar{\gamma}} \\ \frac{1}{\mu_\parallel} &= \frac{1}{m_e} + \frac{\gamma_1 + \bar{\gamma}}{m_0}, \end{aligned} \tag{5.2}$$

where m_0 is the free-electron mass, and the γ's are the Luttinger parameters. Here we use the spherical band model which assumes $\gamma_2 = \gamma_3 = \bar{\gamma}$. The effective mass mismatches at the CdTe/ZnTe interfaces are included[8].

The s-like ground state trial wave function of the exciton system is of the form:

$$\Psi(\vec{r}_\parallel, z_e, z_h) = \psi_e(z_e)\psi_h(z_h)\phi(r_\parallel, z_e - z_h). \tag{5.3}$$

The $\psi_e(z_e)$ and $\psi_h(z_h)$ are taken to be the ground state wave functions for finite square quantum wells. Instead of taking these well potentials to be identical with the fixed conduction band offset V_e^0 and heavy-hole valence band offset V_h^0 in the heterojunction, as extensively used in the study of III-V systems[9], the effective well potentials determining the forms of trial wave functions $\psi_e(z_e)$ and $\psi_h(z_h)$ are taken to be variational parameters V_e, V_h. We expect the difference between V_i and V_i^0 to be small for large band offsets. The wave function $\phi(r_\parallel, z_e - z_h)$ describing

Parameter	CdTe	ZnTe	ZnSe
Band gap at 4K (eV) E_g	1.60	2.39	2.82
Lattice constant (Å) a_0	6.482	6.104	5.669
Static dielectric Constant ϵ_0	9.4	9.67	8.66
Electron effective mass m_e	0.096	0.12	0.17
Luttinger parameter γ_1	5.3	3.74	3.77
Luttinger parameter $\bar{\gamma}$	1.89	1.07	1.24
Elastic constant(10^6N/cm^2) C_{11}	5.33	7.13	8.10
Elastic constant(10^6N/cm^2) C_{12}	3.65	4.07	4.88
Deformation potential(eV) a	1.23	1.35	1.35
Deformation potential(eV) b	-1.18	-1.78	-1.20

Table 5.1: The parameters used in the calculation for the exciton properties. The Luttinger parameters are obtained from reference[10]. The deformation potentials are obtained from references[11, 12]. The rest are from reference[13].

the relative motion is taken to be

$$\phi(r_{\|}, z) = \exp\left(-\frac{\sqrt{r_{\|}^2 + z^2}}{\lambda}\right), \tag{5.4}$$

where λ is the variational parameter describing the exciton size.

The parameters used in the calculation are given in Table 5.1. The resulting values for the binding energy of the exciton(subtracting from the lowest electron and hole subband energies) are shown in Figs. 5.2 and 5.3. In Fig. 5.2, we have made a contour plot of the binding energy for the exciton as a function of the CdTe and ZnTe layer thickness. The valence band offset for the unstrained system is taken to be zero. The contours are relatively insensitive to the value of the ZnTe layer thickness, which indicates that the exciton binding energy depends very weakly on the variation of valence band offset induced by the strain.

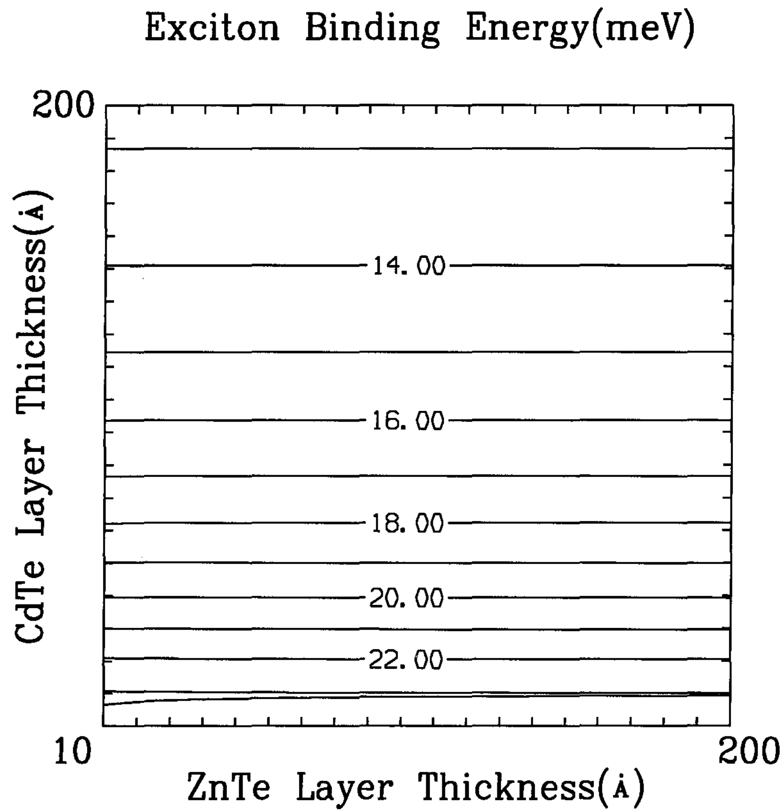

Figure 5.2: The exciton binding energy as a function of ZnTe and CdTe layer thickness. The valence band offset before introducing the strain is taken to be zero. The calculation is performed by explicitly including the strain induced band shift effect.

Figure 5.3 shows the effect of the valence band offset on the binding energy as a function of the CdTe layer thickness. The decrease in the binding energy at small CdTe layer thickness is due to the leakage of the hole wave function into the ZnTe layer. As expected, small valence band offset results in weaker binding, but the effects are relatively weak due to the larger heavy-hole mass and stronger Coulomb attraction by the electron.

Within the envelope function approximation, the oscillator strength per unit area for an exciton localized in a quantum well is given by[14]

$$f_{\mathrm{qw}} = \frac{2mE}{\hbar^2 e^2}|\mu|^2 \left| \int \Psi(0, z, z) dz \right|^2, \tag{5.5}$$

where μ is the dipole transition matrix element between the conduction band and the heavy hole valence band, which only has components in the plane of the well. The exciton envelope function $\Psi(\vec{r}_{\|}, z_e, z_h)$ is assumed to be properly normalized so that

$$\int | \Psi(\vec{r}_{\|}, z_e, z_h) |^2 \, dz_e dz_h d\vec{r}_{\|} = 1. \tag{5.6}$$

To compare with the exciton oscillator strength in the bulk material, the normalized oscillator strength per unit volume for an exciton confined in a quantum well is obtained by dividing the results in eq.(5.5) by the well width L. The ratio of the normalized exciton oscillator strength in the quantum well to the bulk exciton oscillator strength is plotted in Fig. 5.4 as a function of well width. The reference bulk material is taken to be CdTe in the well region. The oscillator strength shows enhancement in the quantum well structure, where the confinement of the electron and hole results in more overlap between electron and hole wave functions.

5.1.3 Type II ZnTe/ZnSe System

The band diagram of the ZnTe/ZnSe system is shown in the lower part of Fig. 5.1. This Type-II band alignment results in the confinement of electrons and holes in separate adjacent layers. Excitons are formed near the interface. Because of

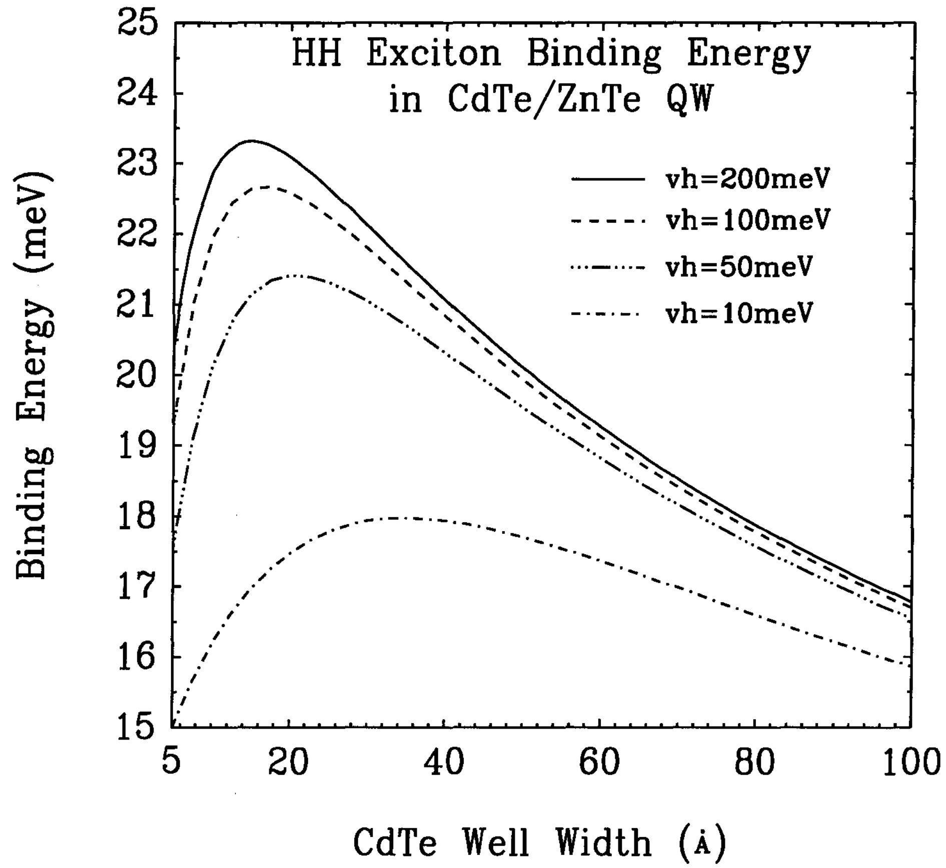

Figure 5.3: The exciton binding energy in the CdTe/ZnTe system as a function of the thickness of the CdTe layer. The parameters are the total valence band offsets.

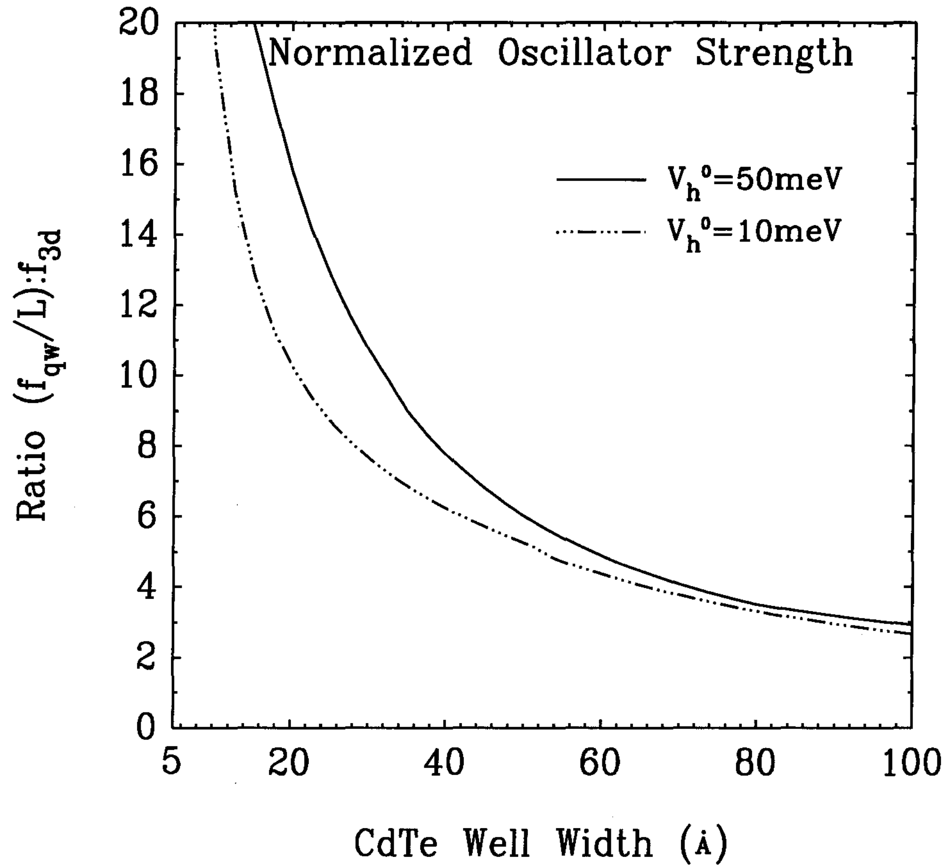

Figure 5.4: The ratio of the oscillator strength in the quantum well divided by the CdTe layer thickness to the value of the exciton oscillator strength for bulk CdTe as a function of CdTe layer thickness. The oscillator strength shows the enhancement expected for quantum well structures, where the confinement of the electron and hole results in an increase in the overall value for the matrix element.

the different dielectric constants in the ZnTe layer and ZnSe layer, we take into account the correction to the Coulomb interaction between electron and hole and the image charge effect at the interface[15]. The Hamiltonian of the exciton system is

$$H = H_{\rm ex} + H_{\rm im} \tag{5.7}$$

with

$$\begin{aligned} H_{\rm ex} &= \left(-\frac{\hbar^2}{2m_e}\frac{\partial^2}{\partial z_e^2} + V_e^0(z_e)\right) + \left(-\frac{\hbar^2}{2m_{z,h}}\frac{\partial^2}{\partial z_h^2} + V_h^0(z_h)\right) + \frac{p_\parallel^2}{2\mu_\parallel} - \frac{2e^2}{(\epsilon_1+\epsilon_2)r}, \\ H_{\rm im} &= -\frac{\epsilon_1-\epsilon_2}{\epsilon_1+\epsilon_2}\left(\frac{e^2}{2\epsilon_2|z_e|} - \frac{e^2}{2\epsilon_1|z_h|}\right), \end{aligned} \tag{5.8}$$

where the origin of the z axis is taken at the interface between ZnTe and ZnSe layers. Because the dielectric constant in the ZnTe layer, ϵ_1, is larger than that in the ZnSe layer, ϵ_2, the hole localized in the ZnTe layer induces a repulsive image charge at the interface, while the electron in the ZnSe layer induces an attractive image charge at the interface.

The valence band offset for the ZnTe/ZnSe heterostructure is about 0.9eV[3]. Due to the large band offsets for both conduction band and valence band, we assume that electron and hole are perfectly confined in separate adjacent layers. The overlap between electron and hole wave functions is zero. The trial wave function for the ground state of s symmetry is chosen to be[16]

$$\begin{aligned} \psi_h(z_h) &= e^{-\alpha_h z_h}\sin\left(\frac{\pi z_h}{L_h}\right) \\ \psi_e(z_e) &= e^{\alpha_e z_e}\sin\left(\frac{\pi z_e}{L_e}\right) \\ \phi(r_\parallel, z) &= e^{-r_\parallel/\lambda}, \end{aligned} \tag{5.9}$$

where $0 \le z_h \le L_h$, $-L_e \le z_e \le 0$. The variational parameters α_e and α_h describe the relative shifts of electron and hole wave functions at the interface as a result of the Coulomb interaction and image charge effect. Parameter λ describes the

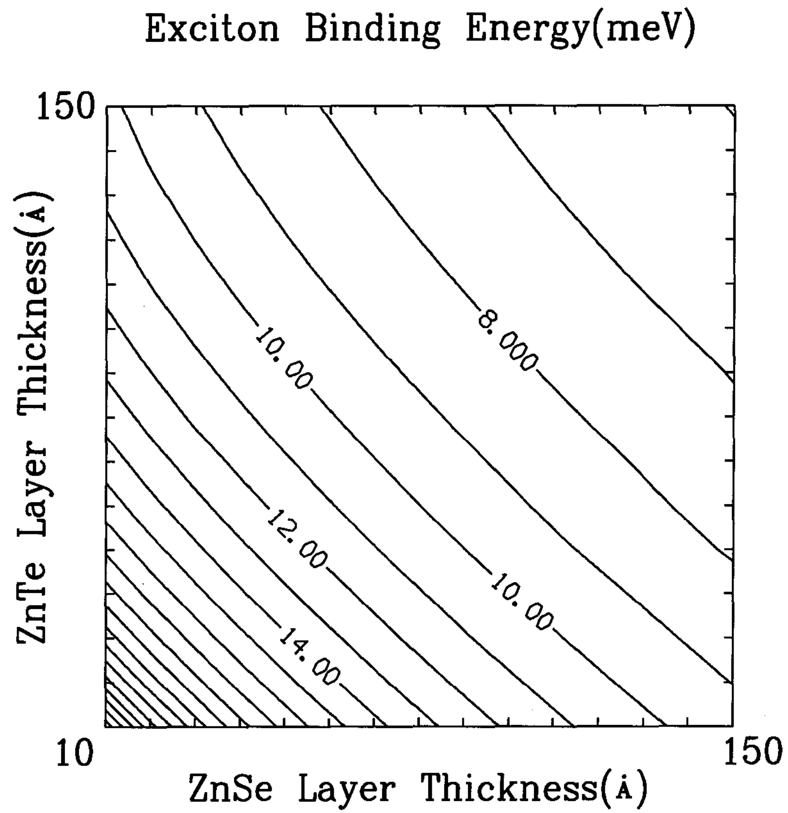

Figure 5.5: The exciton binding energy as a function of ZnTe and ZnSe layer thickness. The assumption of total confinement of the electron and hole makes the result independent of the band offsets and their strain dependence.

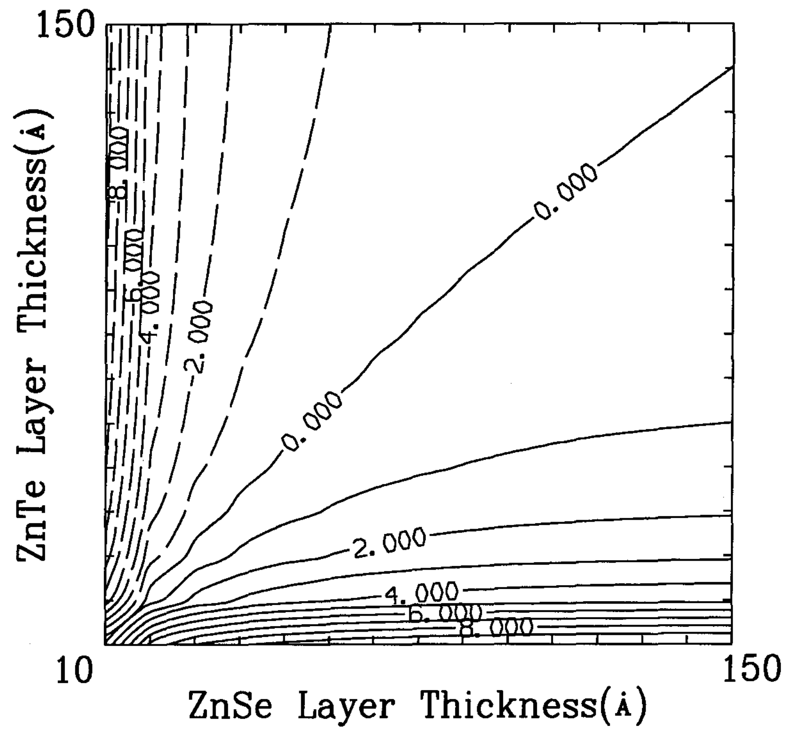

Figure 5.6: Image charge effect corrections to the total energy of the exciton as a function of ZnTe and ZnSe layer thickness. The solid contours are for positive contributions (net repulsion) and the dashed contours are for negative contributions (net attraction).

exciton lateral size. The exciton binding energy is determined by minimizing the total Hamiltonian in eq.(5.7) as a function of the parameters α_e, α_h, and λ.

The heavy exciton binding energy(subtracting lowest electron and heavy hole subband energies from E_{ex}) as a function of ZnTe and ZnSe layer thickness is shown in the contour plot in Fig. 5.5. The contour plot shows the strong dependence of the attractive interaction between the electron and hole on the layer thickness. The confinement of electrons and holes by thin layers can give rise to quite large exciton binding energies. In Fig. 5.6, the image charge correction to the total energy in eq.(5.7) is given as a function of the thickness of the ZnTe and ZnSe layers. For an asymmetric structure, the contribution from the image charge effect can be very important in determining the localization of electron and hole states.

5.2 Exciton Coherent Transfer in Semiconductor Nanostructures

5.2.1 Introduction

Novel semiconductor growth and lithography techniques have enabled us to control the fabrication of device structures on the atomic scale. Structures typically on the scale of nanometers have been investigated. These structures are large enough, on one hand, to exhibit collective properties of bulk crystals qualitatively different from those of constituent atoms, yet small enough to demonstrate quantum confinement and low dimensional behavior. The well known examples are semiconductor quantum well, quantum wire, and quantum dot structures.

These structures have shown various novel properties, giving rise to both new physics and new technology. Excitons confined in these semiconductor structures have higher binding energies and oscillator strengths than those in bulk materials[1]. When an exciton localized in a quantum structure recombines and emits a photon, the photon can be reabsorbed creating an exciton in another quan-

tum structure nearby. In systems where the typical dimensions of the semiconductor quantum structures and the spacings between them are significantly smaller than the photon wavelength, the transfer of excitons between different structures is accomplished through the interaction of near field dipole-dipole transitions (exchange of virtual photons).

Exciton transfer has been extensively studied in the molecular crystals[17, 18]. There the neutral molecules are bound together through the Van der Waals force, which is very small compared to the Coulomb force which binds the electrons to the molecules. An exciton in a molecular crystal is therefore strongly localized around a molecule. The local excitons can well be represented by the excited molecular states. Such a localized excited state will propagate from one molecule to another as a result of the interaction of their electric multipole-multipole transitions. Exciton transfer plays an important role in various phenomena such as photochemical reactions, delayed fluorescence, etc. Therefore it is of significant interest, from both theoretical and practical points of view, to investigate the exciton transfer process in low dimensional semiconductor quantum structure systems.

5.2.2 Theory

The structures we consider are large on the scale of a semiconductor unit cell, but small enough to strongly confine electronic states. Therefore an exciton within a single semiconductor quantum structure can be treated in the Wannier exciton model using the effective mass approximation, while the transfer of localized excitons between quantum structures can be described by analogy with the Frenkel excitons in the molecular crystals. The individual quantum structures are analogous to the molecules in molecular crystals.

We formulate our model in the Hartree-Fock scheme. The Coulomb interaction terms in the complete Hamiltonian of the system are explicitly taken into account only for the electrons in the conduction band and holes in the valence band.

These electrons and holes are subject to the Hartree-Fock self-consistent fields depending on single electron coordinates, including the contributions from the inner electrons together with the nuclear lattice sites and the interactions with the full valence band electrons. The self-consistent potential has the periodicity of the host semiconductor material. The effects from the virtual transitions among the inner electrons are represented by an effective dielectric constant ϵ. The Coulomb interactions between electrons and holes within a quantum structures give rise to the local exciton states localized in that structure. The Coulomb interactions between the electron-hole pairs localized in different structures result in the transfer of excitons between the structures.

The total exciton Hamiltonian of a system, consisting of structure units at positions $\vec{L}, \vec{M}, \cdots$, can be written as

$$H = \sum_{\vec{L}} E_{0,\vec{L}} B_{\vec{L}}^{+} B_{\vec{L}} + \sum_{\vec{L} \neq \vec{M}} \Gamma_{\vec{L},\vec{M}} B_{\vec{L}}^{+} B_{\vec{M}} , \tag{5.10}$$

where $B_{\vec{L}}$ annihilates an exciton localized in the structure at $\vec{L}$ and $E_{0,\vec{L}}$ is the corresponding exciton energy. $\Gamma_{\vec{L},\vec{M}}$ is the coupling matrix element between structures at $\vec{L}$ and $\vec{M}$.

In the framework of a two-band model and neglecting the spin, the local exciton wave functions in a single quantum structure can be written as[19, 20]:

$$\psi_{\mathrm{ex},\vec{L}}(\vec{r}_e, \vec{r}_h) = \phi_{\vec{L}}(\vec{r}_e, \vec{r}_h) u_C(\vec{r}_e) u_V^*(\vec{r}_h) , \tag{5.11}$$

where u_C and u_V are the periodic parts of the Bloch wave functions at the conduction band edge and valence band edge, and $\phi_{\vec{L}}(\vec{r}_e, \vec{r}_h)$ is the exciton envelope function determined by the exciton effective mass equation

$$\left[\sum_{\mu,\nu} \left(-\frac{\hbar^2}{2m_{e,\mu\nu}^*} \frac{\partial^2}{\partial x_{e,\mu} \partial x_{e,\nu}} + \frac{\hbar^2}{2m_{h,\mu\nu}^*} \frac{\partial^2}{\partial x_{h,\mu} \partial x_{h,\nu}} \right) + (E_{0,C} - E_{0,V}) \right.$$
$$\left. + V_C(\vec{r}_e) - V_V(\vec{r}_h) - \frac{e^2}{\epsilon |\vec{r}_e - \vec{r}_h|} \right] \phi_{\vec{L}}(\vec{r}_e, \vec{r}_h) = E_{0,\vec{L}} \phi_{\vec{L}}(\vec{r}_e, \vec{r}_h) . \tag{5.12}$$

Here the $m_{e,\mu\nu}^*$ and $m_{h,\mu\nu}^*$ are the effective mass tensors of the electron and hole, $V_C(\vec{r})$ and $V_V(\vec{r})$ are the effective potentials describing the quantum confinement

of conduction band electrons and valence band holes, and $E_{0,C}$ and $E_{0,V}$ are the conduction band and valence band edges.

An exciton is a quantized polarization field with a transition dipole moment. With the definition

$$\vec{\mu} = e < u_V \, |\vec{r}| \, u_C >_{\text{cell}} \tag{5.13}$$

for the transition dipole moment between the conduction band and the valence band, the oscillator strength of an exciton in a single quantum structure is given by[21]

$$f_{\vec{L}} = \frac{2m\omega}{\hbar e^2} \, |\mu_{\vec{L}}|^2 \left| \int \phi_{\vec{L}}(\vec{r}, \vec{r}) \, d\vec{r} \right|^2 , \tag{5.14}$$

where m is the free electron mass and ω is the transition frequency.

The transfer matrix element due to the Coulomb interaction between structures at $\vec{L}$ and $\vec{M}$ is derived in appendix B

$$\begin{aligned} \Gamma_{\vec{L},\vec{M}} &= \iint \phi^*_{\vec{L}}(\vec{r}\,', \vec{r}\,') u^*_C(\vec{r}\,') u_V(\vec{r}\,') \, \frac{e^2}{\epsilon|\vec{r} - \vec{r}\,'|} \, \phi_{\vec{M}}(\vec{r}, \vec{r}) u_C(\vec{r}) u^*_V(\vec{r}) \, d\vec{r} \, d\vec{r}\,' \\ &- \iint \phi^*_{\vec{L}}(\vec{r}\,', \vec{r}) u^*_C(\vec{r}\,') u_V(\vec{r}) \, \frac{e^2}{\epsilon|\vec{r} - \vec{r}\,'|} \, \phi_{\vec{M}}(\vec{r}\,', \vec{r}) u_C(\vec{r}\,') u^*_V(\vec{r}) \, d\vec{r} \, d\vec{r}\,' \end{aligned} \tag{5.15}$$

where the second term is due to the exchange Coulomb interaction which depends on the overlap of exciton wave functions located in different quantum structures. In what we consider, this term is small and will be neglected.

Expanding the Coulomb interaction in Eq.(5.15) through the dipole term and noticing that the monopole moment contributes nothing because $< u_V \,|\, u_C >_{\text{cell}} = 0$, the transfer matrix element becomes

$$\Gamma_{\vec{L},\vec{M}} = \iint \phi^*_{\vec{L}}(\vec{r}\,', \vec{r}\,') \, \frac{\vec{\mu}^*_{\vec{L}} \cdot \vec{\mu}_{\vec{M}} - 3(\vec{\mu}^*_{\vec{L}} \cdot \hat{n})(\vec{\mu}_{\vec{M}} \cdot \hat{n})}{\epsilon|\vec{r} - \vec{r}\,'|^3} \, \phi_{\vec{M}}(\vec{r}, \vec{r}) \, d\vec{r} \, d\vec{r}\,' , \tag{5.16}$$

where $\hat{n}$ is the unit vector along $(\vec{r} - \vec{r}\,')$. We will see in the following that $\Gamma_{\vec{L},\vec{M}}$ is directly related to the exciton oscillator strength in Eq.(5.14).

For quantum superlattices with N units, the total Hamiltonian of the system in Eq.(5.10) can be diagonalized by introducing the exciton operators with definite

wave vector $\vec{k}$:

$$B_{\vec{k}}^{+} = \frac{1}{\sqrt{N}} \sum_{\vec{L}} e^{i\vec{k}\cdot\vec{L}} B_{\vec{L}}^{+}$$

$$B_{\vec{k}} = \frac{1}{\sqrt{N}} \sum_{\vec{L}} e^{-i\vec{k}\cdot\vec{L}} B_{\vec{L}}\,, \tag{5.17}$$

and by noticing that the coupling matrix element $\Gamma_{\vec{L},\vec{M}} = \Gamma(\vec{L}-\vec{M}\,)$ depends only on $(\vec{L}-\vec{M})$. Eq.(5.10) becomes

$$H = \sum_{\vec{k}} E(\vec{k})\, B_{\vec{k}}^{+} B_{\vec{k}} \tag{5.18}$$

with

$$E(\vec{k}) = E_0 + \sum_{\vec{L}} \Gamma(\vec{L}-\vec{M}\,)\, e^{i\vec{k}\cdot(\vec{L}-\vec{M}\,)}\,. \tag{5.19}$$

In the next three sections, we will study respectively exciton transfer in quantum dots, quantum wires and quantum wells systems.

5.2.3 Quantum Dots

In quantum dots, excitons are confined in all three dimensions. Exciton transfer in quantum dot systems is analogous to that in molecular crystals[18]. The transfer matrix element between two dots separated by R, when the size of the dots is much smaller than the separation, can be obtained from (5.16) and (5.14):

$$\Gamma_{\vec{L},\vec{M}} = \frac{\hbar e^2}{2m\omega\epsilon} \frac{(f_{\vec{L}}\, f_{\vec{M}})^{\frac{1}{2}}}{R^3} \frac{\vec{\mu}_{\vec{L}}^{*}\cdot\vec{\mu}_{\vec{M}} - 3(\vec{\mu}_{\vec{L}}^{*}\cdot\hat{n})(\vec{\mu}_{\vec{M}}\cdot\hat{n})}{\mu_{\vec{L}}\,\mu_{\vec{M}}}\,, \tag{5.20}$$

where $\hat{n}$ is the unit vector along $\vec{R}$. Note the proportionality to $1/R^3$ and to the geometric mean of the exciton oscillator strengths in the two dots.

For a one-dimensional periodic array of dots with adjacent spacing R, the exciton energy band can be evaluated from Eq.(5.19) as

$$E(\vec{k}) \simeq E_0 - \frac{2e^2\hbar f}{\epsilon m\omega R^3} P_2(\cos(\vec{k},\vec{\mu}))\cos kR\,, \tag{5.21}$$

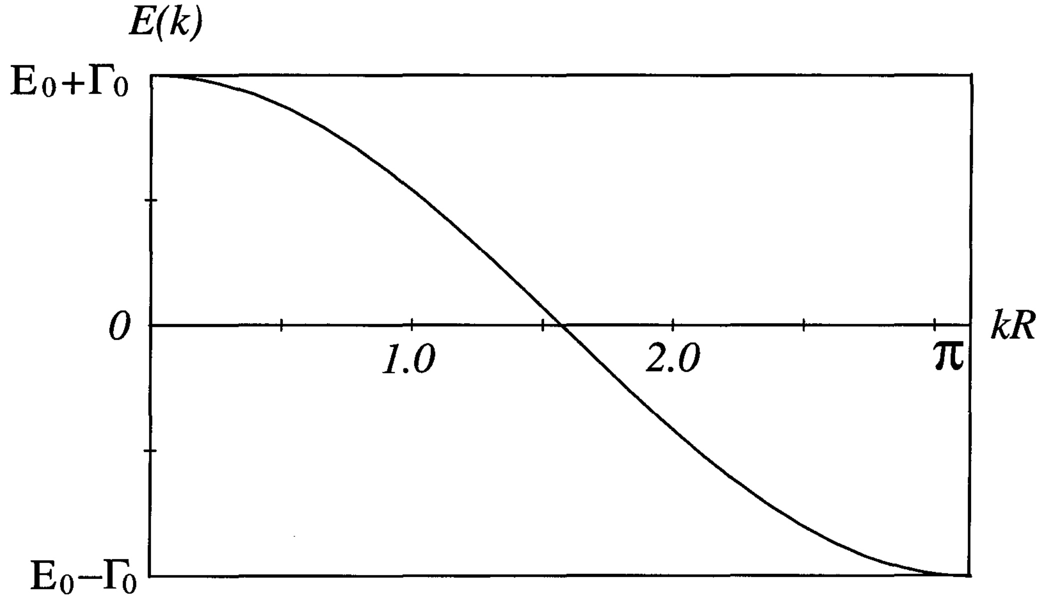

Figure 5.7: Exciton band dispersion in one-dimensional array quantum dot superlattices. E_0 is the exciton energy in a quantum dot and Γ_0 denotes the coupling strength between quantum dots and is given in Eq. (5.21).

where E_0 is the exciton energy in a single quantum dot, P_2 is the second-order Legendre polynomial, and $(\vec{k}, \vec{\mu})$ denotes the angle between $\vec{k}$ and $\vec{\mu}$. The energy dispersion is plotted in Fig. 5.7 The exciton effective mass is

$$\frac{m}{m^*} = \frac{2e^2 f}{\epsilon \hbar \omega R} P_2(\cos(\vec{k}, \vec{\mu})) . \tag{5.22}$$

For a three-dimensional cubic array of quantum dots of finite total volume V, the energy band is[23]:

$$E(\vec{k}) = E_0 + \frac{4\pi n_0 e^2 \hbar f}{3\epsilon m \omega} P_2(\cos(\vec{k}, \vec{\mu})) \left[j_0(kR_0) + j_2(kR_0) - 1 \right] , \tag{5.23}$$

where n_0 is the number of dots per unit volume, j_0 and j_2 are the spherical Bessel functions, and R_0 obeys $(4\pi/3)R_0^3 = V$, where V is the total array volume. The dispersion relation is shown in Fig. 5.8. Notice that $E(\vec{k})$ is singular at $k = 0$.

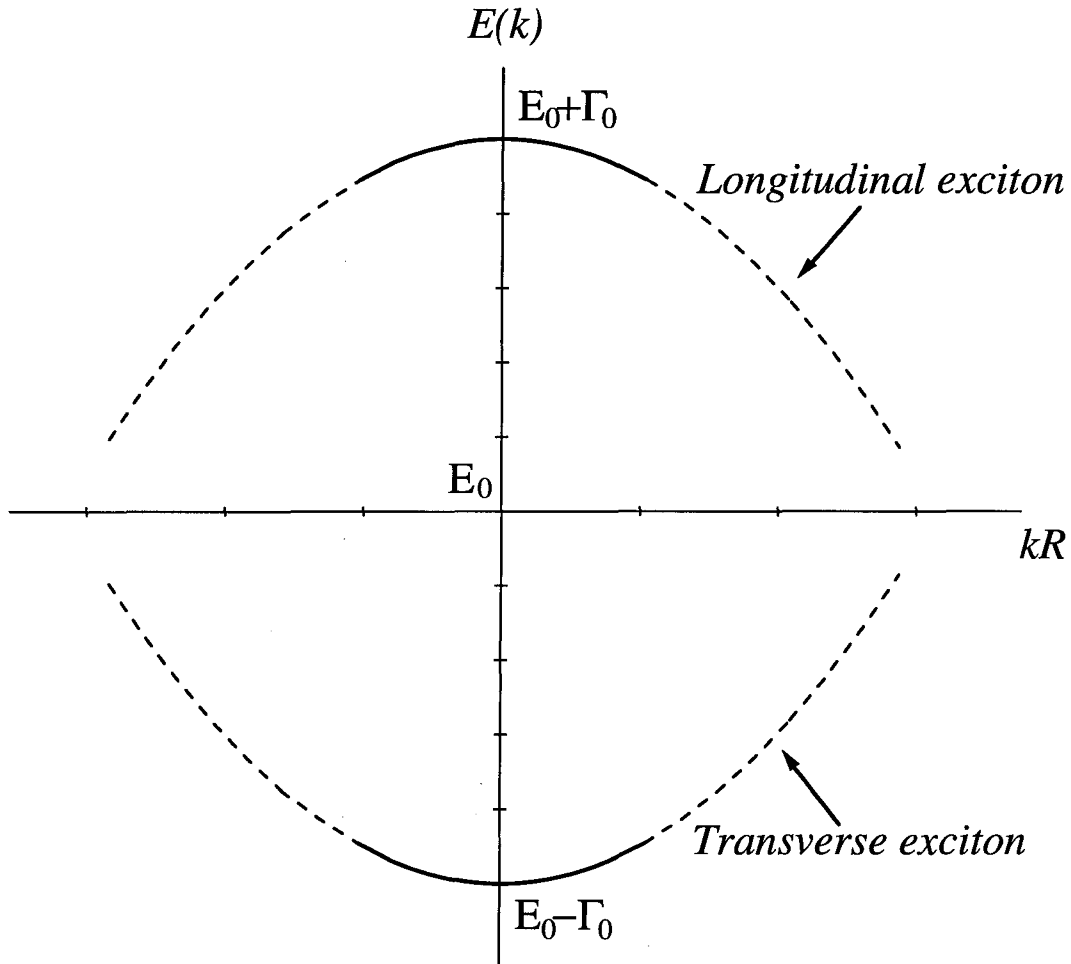

Figure 5.8: Exciton band dispersion in three-dimensional quantum dot configuration with density n_0. E_0 is the exciton energy in a single quantum dot, and the coupling Γ_0 is given in Eq. (5.23), proportional to density n_0.

The effective mass of the exciton near (but not at) $k = 0$ is given by

$$\left(\frac{m}{m^*}\right)_{k\approx 0} = -\frac{8\pi}{135}\left(\frac{3}{4\pi}\right)^{\frac{2}{3}} P_2(\cos(\vec{k},\vec{\mu}))\frac{e^2 n_0^{\frac{1}{3}} f}{\epsilon\hbar\omega} . \tag{5.24}$$

The sign of the effective mass depends on the relative orientation of $\vec{\mu}$ and $\vec{k}$. For optically excited excitons, the mass is positive since $\vec{k} \perp \vec{\mu}$. For certain relative orientations of $\vec{\mu}$ and $\vec{k}$, the coupling between two dots vanishes and the effective mass becomes infinite. Generally, the greater the oscillator strength, the faster the excitons propagate for a given exciton momentum.

5.2.4 Quantum Wires

In quantum wires, excitons are free along the wire axis z direction but confined in the other two dimensions. The exciton envelope function can be factored as

$$\phi_{\vec{L}}(\vec{r}_e,\vec{r}_h) = \varphi_{\vec{L}}(\vec{\rho}_e,\vec{\rho}_h,|z_e - z_h|)\frac{1}{\sqrt{l}}e^{ik_{z,\vec{L}}Z} \tag{5.25}$$

where

$$Z = \frac{m_{e,z}z_e + m_{h,z}z_h}{m_{e,z} + m_{h,z}} , \tag{5.26}$$

l is the length of the wire, $\vec{\rho}$ is the position vector perpendicular to the wire, $k_{z,\vec{L}}$ is the exciton wave vector along the wire, and $\varphi_{\vec{L}}(\vec{\rho}_e,\vec{\rho}_h,z)$ is normalized so that

$$\int |\varphi_{\vec{L}}(\vec{\rho}_e,\vec{\rho}_h,z)|^2 d\vec{\rho}_e d\vec{\rho}_h dz = 1 . \tag{5.27}$$

The transfer matrix element between two wires at $\vec{L}$ and $\vec{M}$, to the lowest order, can be calculated from Eq.(5.16)

$$\begin{aligned}\Gamma_{\vec{L},\vec{M}} &= \delta_{k_{z,\vec{L}},k_{z,\vec{M}}} 2\left[\vec{\mu}_{\vec{L}}^* \cdot \vec{\mu}_{\vec{M}} - 2(\vec{\mu}_{\vec{L}}^* \cdot \hat{n})(\vec{\mu}_{\vec{M}} \cdot \hat{n})\right] \\ &\quad \times \iint \varphi_{\vec{L}}^*(\vec{\rho}',\vec{\rho}',0)\frac{1}{\epsilon(\vec{\rho}-\vec{\rho}')^2}\varphi_{\vec{M}}(\vec{\rho},\vec{\rho},0)d\vec{\rho}d\vec{\rho}' ,\end{aligned} \tag{5.28}$$

where $\vec{\mu}$ is the exciton transition dipole moment perpendicular to the wire, and $\hat{n}$ is the unit vector along $\vec{L}-\vec{M}$ in the plane perpendicular to the wires. Note that the exciton momentum along the wires, $k_{z,\vec{L}}$, is conserved during the transfer. When

the separation between two wires R is much larger than the wire cross-section, one obtains from Eq.(5.28), to order $1/R^2$,

$$\Gamma_{\vec{L},\vec{M}} = \delta_{k_{z,\vec{L}},k_{z,\vec{M}}} \frac{\hbar e^2}{\epsilon m\omega} \frac{(f_{\vec{L}} f_{\vec{M}})^{\frac{1}{2}}}{R^2} \frac{\vec{\mu}^*_{\vec{L}} \cdot \vec{\mu}_{\vec{M}} - 2(\vec{\mu}^*_{\vec{L}} \cdot \hat{n})(\vec{\mu}_{\vec{M}} \cdot \hat{n})}{\mu_{\vec{L}} \mu_{\vec{M}}} , \qquad (5.29)$$

where $f_{\vec{L}}$ is the exciton oscillator strength per unit length in a quantum wire given by

$$f_{\vec{L}} = \frac{2m\omega}{\hbar e^2} |\mu_{\vec{L}}|^2 \left| \int \varphi_{\vec{L}}(\vec{\rho}, \vec{\rho}, 0) \, d\vec{\rho} \right|^2 . \qquad (5.30)$$

For a one-dimensional periodic array of wires with adjacent spacing R, the exciton band dispersion, from Eq.(5.19), is given by

$$\begin{aligned} E(\vec{k}) &= E_0(k_z) + \sum_{M'} e^{i\vec{q}\cdot(\vec{\rho}_L - \vec{\rho}_M)} \Gamma(\vec{L} - \vec{M}) \\ &= E_0(k_z) - \frac{\hbar e^2}{2\epsilon m\omega} \frac{f}{R^2} \cos 2(\vec{q}, \vec{\mu}) \left[(|qR| - \pi)^2 - \frac{\pi^2}{3} \right] , \end{aligned} \qquad (5.31)$$

where $\vec{k} = (\vec{q}, k_z)$, $E_0(k_z)$ is the exciton band dispersion along the wire, which can be derived in the effective mass approximation[24]. The energy dispersion is given in Fig. 5.9.

The exciton effective mass normal to the wire is

$$\frac{m}{m^*} = -\frac{f e^2 \cos 2(\vec{q}, \vec{\mu})}{\epsilon \hbar \omega} , \qquad (5.32)$$

independent of the wire spacing, but inversely proportional to the local exciton oscillator strength. The effective mass is positive for transverse excitons and negative for longitudinal excitons.

For a two-dimensional periodic array of wires, when the exciton wave vector $\vec{q}$ is near the zone center and $qR \ll 1$, we can replace the summation in Eq.(5.19) with an integral. Assuming that the density of wires in the array is n_0, the exciton band dispersion is

$$E(\vec{k}) = E_0(k_z) - \frac{\pi \hbar e^2 n_0 f}{\epsilon m\omega} \cos 2(\vec{q}, \vec{\mu}) . \qquad (5.33)$$

The transverse and longitudinal exciton bands split in the opposite directions.

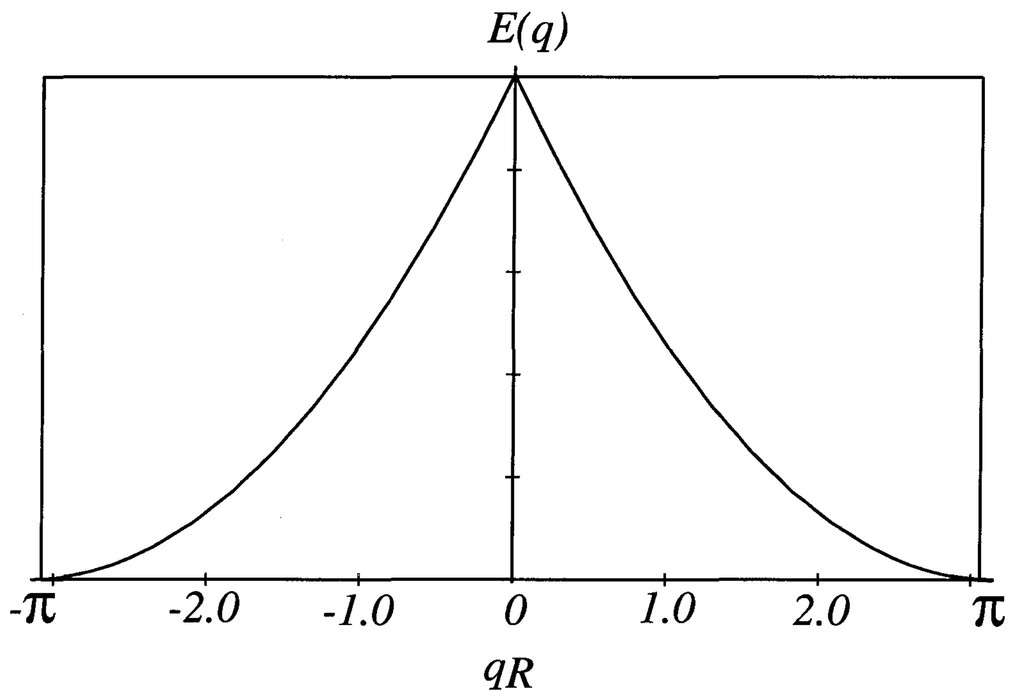

Figure 5.9: Exciton band dispersion in one-dimensional array quantum wire superlattices. The energy dispersion is given by Eq. (5.31).

5.2.5 Quantum Wells

In quantum wells, the electron and hole are confined normal to the well but free in the plane of the well. Choosing the z direction normal to the well, the exciton field and confining potentials in quantum well systems are functions of z only, characteristic of one-dimensional systems. The exciton envelope function can be factored as

$$\phi_{\vec{L}}(\vec{r}_e, \vec{r}_h) = \varphi_{\vec{L}}(z_e, z_h, \vec{\rho}_e - \vec{\rho}_h)\frac{1}{\sqrt{A}}e^{i\vec{k}_{\parallel}\cdot\vec{R}_{\parallel}} \tag{5.34}$$

where

$$\vec{R}_{\parallel} = \frac{m_{e,\parallel}\vec{\rho}_e + m_{h,\parallel}\vec{\rho}_h}{m_{e,\parallel} + m_{h,\parallel}} , \tag{5.35}$$

A is the total in-plane area of the quantum well, and $\vec{\rho}$ is the position vector in the plane of the well. Here we assume that both electrons and holes have simple parabolic band dispersion in the plane of the well with effective masses $m_{e,\parallel}$ and $m_{h,\parallel}$, and the envelope function $\varphi_{\vec{L}}(z_e, z_h, \vec{\rho})$ is properly normalized so that

$$\int |\varphi_{\vec{L}}(z_e, z_h, \vec{\rho})|^2 dz_e dz_h d\vec{\rho} = 1 . \tag{5.36}$$

The transfer matrix element between quantum wells at $\vec{L}$ and $\vec{M}$ can be calculated from Eq.(5.16)

$$\begin{aligned}\Gamma_{\vec{L},\vec{M}} &= \delta_{\vec{k}_{\parallel,\vec{L}},\vec{k}_{\parallel,\vec{M}}}\frac{k_{\parallel}}{\epsilon}(\mu^*_{\parallel,\vec{L}}\mu_{\parallel,\vec{M}} - \mu^*_{z,\vec{L}}\mu_{z,\vec{M}} - i\mu^*_{\parallel,\vec{L}}\mu_{z,\vec{M}} + i\mu^*_{z,\vec{L}}\mu_{\parallel,\vec{M}}) \\ &\quad \times \iint \varphi^*_{\vec{L}}(z', z', 0)e^{-k_{\parallel}|z'-z|}\varphi_{\vec{M}}(z, z, 0)dz\,dz' ,\end{aligned} \tag{5.37}$$

where $\mu_{\parallel} = \vec{\mu}\cdot\vec{k}_{\parallel}/k_{\parallel}$ is the dipole component parallel to the exciton in-plane wave vector $\vec{k}_{\parallel}$. In-plane momentum is conserved: $\vec{k}_{\parallel,\vec{L}} = \vec{k}_{\parallel,\vec{M}} = \vec{k}_{\parallel}$. The transfer matrix element vanishes when $k_{\parallel} = 0$. In this case, the dipole polarization field is uniform in the plane of the wells and there is no dipole transition field outside the well, so the coupling vanishes.

If we assume that the exciton states localized in two wells separated by R do not overlap, the transfer matrix element becomes

$$\Gamma_{\vec{L},\vec{M}} = \delta_{\vec{k}_{\parallel,\vec{L}},\vec{k}_{\parallel,\vec{M}}}\frac{k_{\parallel}\,e^{-k_{\parallel}R}}{\epsilon}(\mu^*_{\parallel,\vec{L}}\mu_{\parallel,\vec{M}} - \mu^*_{z,\vec{L}}\mu_{z,\vec{M}} - i\mu^*_{\parallel,\vec{L}}\mu_{z,\vec{M}} + i\mu^*_{z,\vec{L}}\mu_{\parallel,\vec{M}})$$

$$\times \int \phi^*_{\vec{L}}(z', z', 0) e^{-k_\parallel z'} dz' \times \int \phi_{\vec{M}}(z, z, 0) e^{k_\parallel z} dz \,, \tag{5.38}$$

where the origins of the coordinates are redefined at the centers of each quantum well.

The oscillator strength per unit area of an exciton localized in a quantum well can be obtained from Eq.(5.14)

$$f_{\vec{L}} = \frac{2m\omega}{\hbar e^2} |\mu_{\vec{L}}|^2 \left| \int \varphi_{\vec{L}}(z, z, 0) dz \right|^2 . \tag{5.39}$$

For small but nonzero $k_\parallel$ satisfying $k_\parallel R \ll 1$, as for optically excited excitons, we have

$$\Gamma_{\vec{L},\vec{M}} = \delta_{\vec{k}_{\parallel,\vec{L}}, \vec{k}_{\parallel,\vec{M}}} \frac{\hbar e^2}{2\epsilon m\omega} (f_{\vec{L}}\, f_{\vec{M}})^{\frac{1}{2}}\, k_\parallel \frac{(\mu^*_{\parallel,\vec{L}}\mu_{\parallel,\vec{M}} - \mu^*_{z,\vec{L}}\mu_{z,\vec{M}} - i\mu^*_{\parallel,\vec{L}}\mu_{z,\vec{M}} + i\mu^*_{z,\vec{L}}\mu_{\parallel,\vec{M}})}{\mu_{\vec{L}}\, \mu_{\vec{M}}} . \tag{5.40}$$

The transfer matrix element in this case is proportional to $k_\parallel$ and to the geometric mean of the oscillator strengths in two wells.

From Eq.(5.38), we see that the maximum $\Gamma_{\vec{L},\vec{M}}$ occurs when $k_\parallel R \sim 1$. When this holds, the coupling strength is proportional to $1/R$. Normally R is on the order of 10nm, therefore an exciton created by optical means requires the participation of phonons to obtain such a large in-plane momentum. Excitons with such large momentum can also be excited by alternative means, such as α particles.

In quantum well superlattices with adjacent well separation R, the exciton band dispersion from Eq.(5.19) and Eq.(5.38) is given by

$$\begin{aligned} E(\vec{k}\,) &= E_0(k_\parallel) + \sum_{\vec{M}'} e^{ik_z(z_{\vec{L}} - z_{\vec{M}})} \Gamma_{\vec{L},\vec{M}} \\ &= E_0(k_\parallel) + \frac{1}{\epsilon R}(\mu^*_{\parallel,\vec{L}}\mu_{\parallel,\vec{M}} - \mu^*_{z,\vec{L}}\mu_{z,\vec{M}} - i\mu^*_{\parallel,\vec{L}}\mu_{z,\vec{M}} + i\mu^*_{z,\vec{L}}\mu_{\parallel,\vec{M}}) \\ &\quad \times D(k_\parallel R, k_z R) \int \varphi^*(z', z', 0) e^{-k_\parallel z'} dz' \int \varphi(z, z, 0) e^{k_\parallel z} dz \end{aligned} \tag{5.41}$$

with

$$D(x, y) = 2x e^{-x} \frac{\cos y - e^{-x}}{1 - 2e^{-x}\cos y + e^{-2x}} \,, \tag{5.42}$$

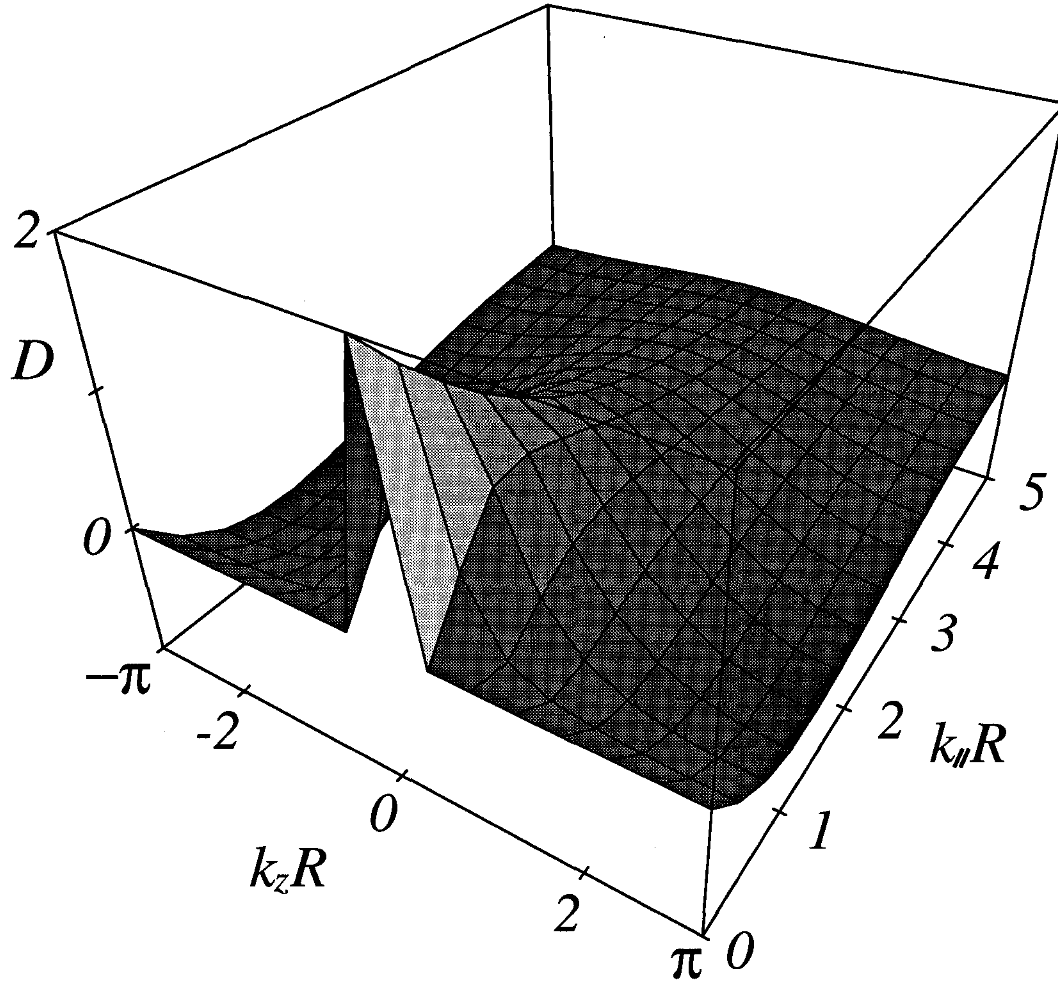

Figure 5.10: Exciton band dispersion function $D(k_{\|}R, k_zR)$ in the quantum well superlattice given in Eq.(5.42).

where $E_0(\vec{k}_{\|})$ denotes the exciton energy in-plane dispersion. The dispersion function $D(k_{\|}R, k_zR)$ is depicted in Fig. 5.10. Notice that D is singular at $k_{\|} = 0$.

For $k_{\|}R \ll 1$ and $k_{\|} \neq 0$, we have

$$m_z^* \propto \frac{Rk_{\|}^2}{f_{\text{ex}}} \,. \tag{5.43}$$

The exciton effective mass is positive when it is polarized along the z direction or longitudinally polarized, and it is negative when transversely polarized.

In quantum well superlattices, the exciton energy band and effective mass exhibit some unusual features due to the long range, in-plane momentum dependent coupling between the quasi 2-D wells. From Fig. 5.10, we see that the exciton band has stronger dispersion near $k_z = 0$ when $k_{\|}R$ is small, which is the case for optically excited excitons. The exciton effective mass decreases for smaller $k_{\|}$. The exciton band dispersion and effective mass are singular at $k_{\|} = 0$, in which case the coupling between wells vanishes.

5.2.6 Discussions

We have derived the exciton transfer matrix elements between quantum wells, quantum wires and quantum dots. The transfer rate for an exciton initially in structure $\vec{L}$ with energy $E_{\vec{L}}$ to structure $\vec{M}$ with energy $E_{\vec{M}}$ is given by Rabi's formula[25]

$$\mathcal{P}_{\vec{L},\vec{M}}(t) = \frac{4|\Gamma_{\vec{L},\vec{M}}|^2}{4|\Gamma_{\vec{L},\vec{M}}|^2 + (E_{\vec{L}} - E_{\vec{M}})^2} \sin^2\left[\sqrt{4|\Gamma_{\vec{L},\vec{M}}|^2 + (E_{\vec{L}} - E_{\vec{M}})^2}\,\frac{t}{2\hbar}\right] . \tag{5.44}$$

The transfer phenomenon is pronounced only when $|\Gamma_{\vec{L},\vec{M}}|$ is comparable with or bigger than $|E_{\vec{L}} - E_{\vec{M}}|$. At resonance when $E_{\vec{L}} = E_{\vec{M}}$, the transfer time is determined only by the coupling strength $\Gamma_{\vec{L},\vec{M}}$

$$t = \frac{h}{\Gamma_{\vec{L},\vec{M}}} . \tag{5.45}$$

We have done numerical analysis for prototypical GaAs/GaAlAs systems of quantum wells, quantum wires and quantum dots. The exciton effective mass equations (5.12) in these three systems are solved using variational approaches[26, 24, 27]. The exciton states are taken to be heavy hole associated. It is found that, for quantum wire and quantum dot structures of 50Å cross section separated by about 100Å, the transfer matrix element is on the order of 10^{-3}meV, which corresponds to a resonant transfer time of 1 ns, comparable with the exciton lifetime. The transfer matrix element between quantum wells depends on the exciton in-plane

Systems	Well	Wire	Dot	Anthracene
Γ	$\propto \frac{k_{\parallel} e^{-k_{\parallel} R}}{a^2}$	$\propto \frac{1}{R^2 a}$	$\propto \frac{1}{R^3}$	$\propto \frac{1}{R^3}$
Dipole Moment	4.3Å	4.3Å	4.3Å	1.3Å
Spacing R	10^2Å	10^2Å	10^2Å	9Å
Exciton Size a	10^2Å	10^2Å	10^2Å	1.3Å
Strength	$10^{-4} \sim 10^{-3}$meV	10^{-3}meV	10^{-3}meV	14meV

Table 5.2: Summary of results for quantum wells, quantum wires, quantum dots based on GaAs material system, and their comparison with molecular crystal anthracene.

wavelength $\lambda_{\parallel}$. For two quantum wells 50Å in width separated by a 50Å barrier, the transfer matrix element is on the order of 10^{-4}meV for $\lambda_{\parallel} = 10^4$Å, corresponding to optically excited excitons, and it is increased by an order of magnitude for $\lambda_{\parallel} = 100$Å. The coupling strength between two semiconductor quantum structures is significantly smaller than that in molecular crystals such as anthracene, where the intermolecular spacing is about 10Å and the transfer matrix element is about 14meV[18]. This is primarily due to the loosely bound nature of Wannier excitons in semiconductors. Table 5.2 summarize the results for quantum wells, quantum wires, quantum dots based on GaAs material system, and their comparison with molecular crystal anthracene.

Due to phonons and structural imperfection in most synthesized semiconductor quantum structures, the exciton transition exhibits inhomogeneous broadening of a few meV, much larger than the dipole-dipole coupling between structures. Therefore it is necessary either to reduce the effects due to phonons and structural defects or to increase the coupling in order to observe exciton transfer experimentally. The transfer matrix element between semiconductor quantum structures

can be increased by increasing the localized exciton oscillator strengths and by reducing the distance between the structures. The enhancement of the exciton oscillator strength relies on the increase of Coulomb correlation in the exciton system. Structures producing increased quantum confinement and materials of more ionic character, such as the II-VI semiconductor compounds with wide bandgaps[28], can give rise to larger exciton oscillator strength. In addition, since the electronic states in the structures are not completely confined, reducing the separation between structures will result in increased overlap of local exciton states. Tunneling of electron-hole pairs and the exchange Coulomb interaction term in Eq.(5.15) will become important. The transfer matrix elements due to the tunneling of electron-hole pairs and Coulomb exchange interaction are given in appendix B, they fall off exponentially with the distance between structures[22].

5.2.7 Summary

We have studied two subjects in this chapter regarding excitons in semiconductor heterostructures. In the first part, excitons in two wide bandgap II-VI heterostructures are studied. In CdTe/ZnTe superlattice, exciton is found to behave like a classic Type-I heterojunction with large exciton binding energy due to close correlation of the electron and hole in the CdTe layer. For small CdTe layer thickness, however, the confinement of holes in the CdTe layer is weak. The leakage of the hole into the surrounding ZnTe layer results in a lowering of the binding energy of the exciton. The oscillator strength in the quantum well shows the expected enhancement over the oscillator strengths in the bulk.

For the case of ZnTe/ZnSe, the Type-II character of the heterojunction results in the confinement of the electrons and holes in different layers. The image charge induced by the difference in dielectric constants plays an important role in determining the degree of localization of the electron and hole at the interface. The binding energy of the exciton in these systems is much smaller than that for the

Type-I case of CdTe/ZnTe.

In the second part, we have investigated the exciton transfer and some resulting band structures in semiconductor quantum structure systems. It was shown that the transfer matrix elements between quantum dots and quantum wires depend on the exciton polarization and are proportional to the geometric mean of the exciton oscillator strengths in the structures. They vary with the distance R between structures as R^{-3} and R^{-2} respectively. The transfer matrix element between quantum wells depends on the exciton wave vector in the plane of the wells, $\vec{k}_{\|}$, and vanishes when $\vec{k}_{\|} = 0$. The exploration of this new exciton transfer phenomenon offers a wealth of new physics and may be a source of new technology based on excitonic devices in the future.

Bibliography

[1] A. C. Gossard, *Treatise on Material Science and Technology*, edited by K. T. Tu and R. Rosenberg(Academic, New York, 1982), Vol. 24.

[2] J. Ding, H. Jeon, T. Ishihara, M. Hagerott, and A. V. Nurmikko, *Phys. Rev. Lett.* **69** 1707 (1992).

[3] Y. Rajakarunanayake, M. C. Phillips, J. O. McCaldin, D. H. Chow, D. A. Collins, and T. C. McGill, *Proc. of the SPIE.* Vol. **1285**, 142(1990).

[4] J. O. McCaldin, T. C. McGill and C.A. Mead, *Phys. Rev. Lett.* **36**, 56(1976).

[5] R.P. Stanley, B.J. Hawdon, J. Hegarty, R.D. Feldman, and R.F. Austin *Appl. Phys. Lett.* **58** (1991) 2972.

[6] Ji-Wei Wu and A.V. Nurmikko, *Phys. Rev. B* **38** 1504 (1988).

[7] A. Baldereschi and N.C. Lipari, *Phys. Rev. B* **3** 439 (1971).

[8] C. Priester, G. Allen and M. Lannoo, *Phys. Rev. B* **30** 7302 (1984).

[9] R.L. Greene, K.K. Bajaj and D.E. Phelps, *Phys. Rev. B* **29** 1807(1984).

[10] P. Lawaetz, *Phys. Rev. B* **4** 3460 (1971).

[11] D.L. Camphausen, G.A.N. Connell and W. Paul, *Phys. Rev. Lett.* **26** 184 (1971).

[12] A.A. Kaplyanskii and L.G. Suslina, *Sov. Phys. Solid State* **7** 1881(1966).

[13] *Landolt-Börnstein Numerical Data and Functional Relationships in Science and Technology*, edited by O. Madelung(Springer-Verlag, Berlin, 1987), Vol. 22a.

[14] R.J. Elliott, *Phys. Rev.* **108** 1384 (1957).

[15] J.D. Jackson, *Classical Electrodynamics*, 2nd edition, Chap. 4, John Wiley & Sons, New York 1975.

[16] G. Duggan and H.I. Ralph, *Phys. Rev. B* **35** 4152 (1987).

[17] W. R. Heller and A. Marcus, *Phys. Rev.* **84**, 809 (1951).

[18] A. S. Davydov, *Theory of Molecular Excitons*, New York-London 1971.

[19] G. Dresslhaus, *J. Phys. Chem. Solids* **1**, 14 (1956).

[20] E. O. Kane, *Phys. Rev. B* **11**, 3850 (1975).

[21] R. J. Elliott, *Phys. Rev.* **108**, 1384 (1957).

[22] Y. X. Liu, S. K. Kirby and T. C. McGill, unpublished.

[23] M. H. Cohen and F. Keffer, *Phys. Rev.* **99**, 1128 (1955).

[24] I. Suemune and L. A. Coldren, *IEEE J. Quantum Electron.* **24**, 1778 (1988).

[25] C. Cohen-Tannoudji, B. Diu and F. Lalöe, *Quantum Mechanics*, Vol. 1, Chap. IV, Wiley Interscience, New York-London 1 977.

[26] R. L. Greene, K. K. Bajaj, and D. E. Phelps, *Phys. Rev. B* **29**, 1807 (1984).

[27] G. W. Bryant, *Phys. Rev. B* **37**, 8763 (1988).

[28] Y. X. Liu, Y. Rajakarunanayake and T. C. McGill, *J. Crystal Growth* **117**, 742(1992).

Appendix A

Eight-band k·p Hamiltonian

A.1 Basis and k·p Hamiltonian

The basis functions in eight-band **k·p** model include the Γ_6 conduction-band, the Γ_8 light-hole and heavy-hole bands, and the Γ_7 spin-orbit split-off valence-band:

$$u^{\Gamma_6}_{1/2} = |s\rangle\uparrow, \tag{A.1}$$

$$u^{\Gamma_6}_{-1/2} = |s\rangle\downarrow, \tag{A.2}$$

$$u^{\Gamma_8}_{3/2} = \frac{i}{\sqrt{6}}\left[(|X\rangle - i|Y\rangle)\uparrow + 2|Z\rangle\downarrow\right], \tag{A.3}$$

$$u^{\Gamma_8}_{1/2} = -\frac{i}{\sqrt{2}}(|X\rangle - i|Y\rangle)\downarrow, \tag{A.4}$$

$$u^{\Gamma_8}_{-1/2} = \frac{i}{\sqrt{2}}(|X\rangle + i|Y\rangle)\uparrow, \tag{A.5}$$

$$u^{\Gamma_8}_{-3/2} = -\frac{i}{\sqrt{6}}\left[(|X\rangle + i|Y\rangle)\downarrow - 2|Z\rangle\uparrow\right], \tag{A.6}$$

$$u^{\Gamma_7}_{1/2} = -\frac{i}{\sqrt{3}}\left[(|X\rangle + i|Y\rangle)\downarrow + |Z\rangle\uparrow\right], \tag{A.7}$$

$$u^{\Gamma_7}_{-1/2} = -\frac{i}{\sqrt{3}}\left[(|X\rangle - i|Y\rangle)\uparrow - |Z\rangle\downarrow\right]. \tag{A.8}$$

The phases of these basis satisfy $Cu^{\Gamma_6}_{1/2} = u^{\Gamma_6}_{-1/2}$, $Cu^{\Gamma_6}_{-1/2} = -u^{\Gamma_6}_{1/2}$, $Cu^{\Gamma_8}_{3/2} = -u^{\Gamma_8}_{-3/2}$, $Cu^{\Gamma_8}_{-3/2} = u^{\Gamma_8}_{3/2}$, $Cu^{\Gamma_8}_{1/2} = u^{\Gamma_8}_{-1/2}$, $Cu^{\Gamma_8}_{-1/2} = -u^{\Gamma_8}_{1/2}$, $Cu^{\Gamma_7}_{1/2} = -u^{\Gamma_7}_{-1/2}$, $Cu^{\Gamma_7}_{-1/2} = u^{\Gamma_7}_{1/2}$, where the conjugation operator $C = JK$ is the product of space inversion operator

J and the Kramers time reversal operator K.

The $\mathbf{k}\cdot\mathbf{p}$ Hamiltonian is given by[1]

$$\begin{bmatrix} u^{\Gamma_6}_{-1/2} & u^{\Gamma_6}_{1/2} & u^{\Gamma_8}_{-3/2} & u^{\Gamma_8}_{-1/2} & u^{\Gamma_8}_{1/2} & u^{\Gamma_8}_{3/2} & u^{\Gamma_7}_{-1/2} & u^{\Gamma_7}_{1/2} \\ A & 0 & T^*+V^* & 0 & -\sqrt{3}(T-V) & \sqrt{2}(W-U) & W-U & \sqrt{2}(T^*+V^*) \\ 0 & A & \sqrt{2}(W-U) & -\sqrt{3}(T^*+V^*) & 0 & T-V & -\sqrt{2}(T-V) & W^*+U \\ T+V & \sqrt{2}(W^*-U) & -P+Q & -S^* & R & 0 & \left(\frac{3}{2}\right)^{1/2} S & -\sqrt{2}Q \\ 0 & -\sqrt{3}(T+V) & -S & -P-Q & 0 & R & -\sqrt{2}R & \frac{1}{\sqrt{2}}S \\ -\sqrt{3}(T^*-V^*) & 0 & R^* & 0 & -P-Q & S^* & \frac{1}{\sqrt{2}}S^* & \sqrt{2}R^* \\ \sqrt{2}(W^*-U) & T^*-V^* & 0 & R^* & S & -P+Q & \sqrt{2}Q & \left(\frac{3}{2}\right)^{1/2} S^* \\ W^*-U & -\sqrt{2}(T^*-V^*) & \left(\frac{3}{2}\right)^{1/2} S^* & -\sqrt{2}R^* & \frac{1}{\sqrt{2}}S & \sqrt{2}Q & Z & 0 \\ \sqrt{2}(T+V) & W+U & -\sqrt{2}Q & \frac{1}{\sqrt{2}}S^* & \sqrt{2}R & \left(\frac{3}{2}\right)^{1/2} S & 0 & Z \end{bmatrix}, \tag{A.9}$$

where

$$A = E_c + \left[A' + \frac{\hbar^2}{2m}\right](k_x^2 + k_y^2 + k_z^2)\,, \tag{A.10}$$

$$P = -E_v + \frac{\hbar^2}{2m}\gamma_1(k_x^2 + k_y^2 + k_z^2)\,, \tag{A.11}$$

$$U = \frac{1}{\sqrt{3}}P_0 k_z\,, \tag{A.12}$$

$$Q = \frac{\hbar^2}{2m}\gamma_2(k_x^2 + k_y^2 - 2k_z^2), \tag{A.13}$$

$$V = \frac{1}{\sqrt{6}}P_0(k_x - ik_y)\,, \tag{A.14}$$

$$R = \frac{\hbar^2}{2m}\sqrt{3}[-\gamma_2(k_x^2 - k_y^2) + 2i\gamma_3 k_x k_y]\,, \tag{A.15}$$

$$W = i\frac{1}{\sqrt{3}}Bk_x k_y\,, \tag{A.16}$$

$$S = \frac{\hbar^2}{2m}2\sqrt{3}\gamma_3(k_x - ik_y)k_z\,, \tag{A.17}$$

$$T = \frac{1}{\sqrt{6}}Bk_z(k_x + ik_y)\,, \tag{A.18}$$

$$Z = E_v - \Delta - \frac{\hbar^2}{2m}\gamma_1(k_x^2 + k_y^2 + k_z^2)\,. \tag{A.19}$$

The constants γ_1, γ_2 and γ_3 are the modified Luttinger parameters, and are related to the parameters used by Luttinger[3] for top of valence band, γ_1^L, γ_2^L and γ_3^L, by

$$\gamma_1 = \gamma_1^L - \frac{E_p}{3E_g + \Delta}\,, \tag{A.20}$$

$$\gamma_2 = \gamma_2^L - \frac{1}{2}\frac{E_p}{3E_g + \Delta}\,, \tag{A.21}$$

$$\gamma_3 = \gamma_3^L - \frac{1}{2}\frac{E_p}{3E_g + \Delta}, \tag{A.22}$$

where the conduction to valence band gap

$$E_g = E_c - E_v \tag{A.23}$$

and the conduction-valence interaction parameter E_p is related to the transition matrix element P_0 by

$$E_p = \frac{2m}{\hbar^2} P_0^2 . \tag{A.24}$$

Parameter A' is related to the electron effective mass in the conduction band by

$$A' = \frac{\hbar^2}{2m}\left[\frac{m}{m_c} - 1 - \left(2 + \frac{E_g}{E_g + \Delta}\right)\frac{E_p}{3E_g}\right] . \tag{A.25}$$

A.2 Strain Induced Hamiltonian

Under external strain, addition term is added to the **k·p** Hamiltonian. The Hamiltonian due to strain contribution is given by[1, 2]

$$\begin{bmatrix} a'e & 0 & t^*+v^* & 0 & -\sqrt{3}(t+v) & \sqrt{2}(w+u) & w+u & \sqrt{2}(t^*-v^*) \\ 0 & a'e & \sqrt{2}(w-u) & -\sqrt{3}(t^*+v^*) & 0 & t+v & -\sqrt{2}(t+v) & w^*-u \\ t-v & \sqrt{2}(w^*+u) & -p+q & -s^* & r & 0 & \left(\frac{3}{2}\right)^{1/2}s & -\sqrt{2}q \\ 0 & -\sqrt{3}(t-v) & -s & -p-q & 0 & r & -\sqrt{2}r & \frac{1}{\sqrt{2}}s \\ -\sqrt{3}(t^*+v^*) & 0 & r^* & 0 & -p-q & s^* & \frac{1}{\sqrt{2}}s^* & \sqrt{2}r^* \\ \sqrt{2}(w^*+u) & t^*+v^* & 0 & r^* & s & -p+q & \sqrt{2}q & \left(\frac{3}{2}\right)^{1/2}s^* \\ w^*+u & -\sqrt{2}(t^*+v^*) & \left(\frac{3}{2}\right)^{1/2}s^* & -\sqrt{2}r^* & \frac{1}{\sqrt{2}}s & \sqrt{2}q & -ae & 0 \\ \sqrt{2}(t-v) & w-u & -\sqrt{2}q & \frac{1}{\sqrt{2}}s^* & \sqrt{2}r & \left(\frac{3}{2}\right)^{1/2}s & 0 & -ae \end{bmatrix}, \tag{A.26}$$

where

$$w = i\frac{1}{\sqrt{3}}b' e_{xy} , \tag{A.27}$$

$$p = a(e_{xx} + e_{yy} + e_{zz}) , \tag{A.28}$$

$$t = \frac{1}{\sqrt{6}}b'(e_{xz} + ie_{yz}) , \tag{A.29}$$

$$q = b[e_z z - \frac{1}{2}(e_{xx} + e_{yy})] , \tag{A.30}$$

$$u = \frac{1}{\sqrt{3}} P_0 \sum_j e_{zj} k_j \,, \tag{A.31}$$

$$r = \frac{\sqrt{3}}{2} b(e_{xx} - e_{yy}) - i d e_{xy} \,, \tag{A.32}$$

$$v = \frac{1}{\sqrt{6}} P_0 \sum_j (e_{xj} - i e_{yj}) k_j \,, \tag{A.33}$$

$$s = -d(e_{xz} - i e_{yz}) \,, \tag{A.34}$$

$$e = e_{xx} + e_{yy} + e_{zz} \,. \tag{A.35}$$

The Bir and Pikus deformation potential constants a, b, and d describe the coupling of the valence band to strain while the constants a' and b' describe the coupling of the conduction band to strain. a is referred to as the hydrostatic deformation potential which determines the shift due to isotropic strain. b is referred to as the uniaxial deformation strain which determines the heavy-hole and light-hole band splitting for [001] strain.

A.3 Interaction of Spin and Magnetic Field

When external magnetic field presents, the interaction of spin and B field adds a constant term to the **k·p** Hamiltonian. In eight-band model, the following terms are added to the **k·p** matrix elements[4].

$$H'_{11} = \frac{1}{2} \mu B \,, \tag{A.36}$$

$$H'_{22} = -\frac{1}{2} \mu B \,, \tag{A.37}$$

$$H'_{33} = -\frac{3}{2} \kappa \mu B \,, \tag{A.38}$$

$$H'_{44} = -\frac{1}{2} \kappa \mu B \,, \tag{A.39}$$

$$H'_{47} = i \frac{1}{2} \sqrt{2} (\kappa + 1) \mu B \,, \tag{A.40}$$

$$H'_{55} = \frac{1}{2} \kappa \mu B \,, \tag{A.41}$$

$$H'_{58} = -i \frac{1}{2} \sqrt{2} (\kappa + 1) \mu B \,, \tag{A.42}$$

$$H'_{66} = \frac{3}{2}\kappa\mu B\,, \tag{A.43}$$

$$H'_{74} = -i\frac{1}{2}\sqrt{2}(\kappa+1)\mu B\,, \tag{A.44}$$

$$H'_{77} = -\left(\kappa+\frac{1}{2}\right)\mu B\,, \tag{A.45}$$

$$H'_{85} = i\frac{1}{2}\sqrt{2}(\kappa+1)\mu B\,, \tag{A.46}$$

$$H'_{88} = \left(\kappa+\frac{1}{2}\right)\mu B\,, \tag{A.47}$$

where $\mu = e\hbar/2mc$ is the Bohr magneton.

Bibliography

[1] T. B. Bahder, *Phys. Rev. B* **41**, 11992 (1992).

[2] G. L. Bir and G. E. Pikus, *Symmetry and Strain Induced Effects in Semiconductors*, (Wiley, New York, 1 974).

[3] J. M. Luttinger, *Phys. Rev.* **102**, 1030 (1956).

[4] C. R. Pidgeon and R. N. Brown, *Phys. Rev.* **146**, 575 (1966).

Appendix B

Exciton Transfer Matrix Element in Quantum Structures

B.1 Basis Functions and Hamiltonian

In deriving the exciton transfer matrix element in semiconductor quantum structures, we employ an approach analogous to that developed by Heller and Marcus in studying exciton transfer in ionic and molecular crystals[1, 2]. We consider a system consisting of N identical quantum structures. The filled valence band Ψ_0 is defined as the ground-state of the system. The basis functions are the Wannier functions of the conduction band and the valence band localized in a particular structure

$$\begin{aligned} W^*_{n,C}(\vec{r}-\vec{L}) &= a^+_{n,\vec{L}}\Psi_0 \,, \\ W_{n,V}(\vec{r}-\vec{L}) &= d^+_{n,\vec{L}}\Psi_0 \,, \end{aligned} \tag{B.1}$$

where we use $\{\vec{L}, \vec{M}, \cdots\}$ to specify the positions of quantum structures, $\{C, V\}$ to denote the conduction band and the valence band respectively, and $\{n\}$ to indicate the localized electronic states.

As a starting approximation, we neglect spin and electron-phonon interaction. We further assume that for each quantum structure the electrons in the inner band together with the positive atomic nuclei contribute to an effective potential $U_{\vec{L}}(\vec{r})$. The total Hamiltonian for the electron system, in the Born-Oppenheimer approximation, can be expressed as

$$\begin{aligned} H &= \sum_{\vec{L}} \left(\sum_i \frac{p_{Li}^2}{2m} - U_{\vec{L}}(\vec{r}_{Li}) + \frac{1}{2} \sum_{i \neq j} \frac{e^2}{|\vec{r}_{Li} - \vec{r}_{Lj}|} \right) \\ &\quad - \sum_{\substack{i \\ \vec{L} \neq \vec{M}}} U_{\vec{M}}(\vec{r}_{Li}) + \frac{1}{2} \sum_{\substack{i,j \\ \vec{L} \neq \vec{M}}} \frac{e^2}{|\vec{r}_{Li} - \vec{r}_{Mj}|} \end{aligned} \tag{B.2}$$

where $\{i, j, \cdots\}$ refer to the electrons. Since the the quantum structures and their separations are usually very small compared with the wavelength of optical transitions in the quantum structures, we treat the interactions between electrons with a simple Coulomb interaction and ignore the retardation effect.

When expanded in the basis (B.1), the Hamiltonian of the system, with respect to a constant reference energy of the full valence band, is

$$\begin{aligned} H &= \sum_{\substack{n,n' \\ \vec{L},\vec{M}}} a^+_{n,\vec{L}} a_{n',\vec{M}} H^C_{n\vec{L},n'\vec{M}} - \sum_{\substack{n,n' \\ \vec{L},\vec{M}}} d^+_{n,\vec{L}} d_{n',\vec{M}} H^V_{n\vec{L},n'\vec{M}} \\ &- \sum_{\substack{n_1,n_2,n_3,n_4 \\ \vec{L}_1,\vec{L}_2,\vec{L}_3,\vec{L}_4}} a^+_{n_1,\vec{L}_1} a_{n_2,\vec{L}_2} d^+_{n_3,\vec{L}_3} d_{n_4,\vec{L}_4} \left[A\begin{pmatrix} n_4 & n_1 & n_2 & n_3 \\ \vec{L}_4 & \vec{L}_1 & \vec{L}_2 & \vec{L}_3 \\ V & C & C & V \end{pmatrix} - A\begin{pmatrix} n_4 & n_1 & n_3 & n_2 \\ \vec{L}_4 & \vec{L}_1 & \vec{L}_3 & \vec{L}_2 \\ V & C & V & C \end{pmatrix} \right] \end{aligned} \tag{B.3}$$

with

$$\begin{aligned} H^C_{n\vec{L},n'\vec{M}} &= \int W^*_{n,C}(\vec{r}-\vec{L}) \left(-\frac{\hbar^2}{2m} \nabla^2 \right) W_{n',C}(\vec{r}-\vec{M}) d\vec{r} \\ &+ \sum_{\vec{L}',i} \left[\int W^*_{n,C}(\vec{r}-\vec{L})\, U_{\vec{L}'}(\vec{r})\, W_{n',C}(\vec{r}-\vec{M}) d\vec{r} + A\begin{pmatrix} i & n & n' & i \\ \vec{L}' & \vec{L} & \vec{M} & \vec{L}' \\ V & C & C & V \end{pmatrix} - A\begin{pmatrix} i & n & i & n' \\ \vec{L}' & \vec{L} & \vec{L}' & \vec{M} \\ V & C & V & C \end{pmatrix} \right] \end{aligned} \tag{B.4}$$

$$\begin{aligned} H^V_{n\vec{L},n'\vec{M}} &= \int W^*_{n,V}(\vec{r}-\vec{L}) \left(-\frac{\hbar^2}{2m} \nabla^2 \right) W_{n',V}(\vec{r}-\vec{M}) d\vec{r} \\ &+ \sum_{\vec{L}',i} \left[\int W^*_{n,V}(\vec{r}-\vec{L})\, U_{\vec{L}'}(\vec{r})\, W_{n',V}(\vec{r}-\vec{M}) d\vec{r} + A\begin{pmatrix} i & n & n' & i \\ \vec{L}' & \vec{L} & \vec{M} & \vec{L}' \\ V & V & V & V \end{pmatrix} - A\begin{pmatrix} i & n & i & n' \\ \vec{L}' & \vec{L} & \vec{L}' & \vec{M} \\ V & V & V & V \end{pmatrix} \right]. \end{aligned}$$

Here we use the abbreviated notation for the matrix element describing the Coulomb interaction

$$A\begin{pmatrix} n_1 & n_2 & n_3 & n_4 \\ \vec{L}_1 & \vec{L}_2 & \vec{L}_3 & \vec{L}_4 \\ j_1 & j_2 & j_3 & j_4 \end{pmatrix} = \iint W^*_{n_1,j_1}(\vec{r}-\vec{L}_1)W^*_{n_2,j_2}(\vec{r}\,'-\vec{L}_2)\,\frac{e^2}{\epsilon|\vec{r}-\vec{r}\,'|}\,W_{n_3,j_3}(\vec{r}\,'-\vec{L}_3)W_{n_4,j_4}(\vec{r}-\vec{L}_4)\,d\vec{r}\,d\vec{r}\,'\,. \tag{B.5}$$

The first two terms in Hamiltonian (B.3) describe individual electron and hole states. The third term describes the interactions between electrons and holes, including the direct Coulomb interactions and Coulomb exchange interactions. The dielectric constant ϵ accounts for all the virtual transitions between the bands and the screening of Coulomb interactions.

The third term describing Coulomb interactions in Eq. (B.3) can be grouped as follows, according to the locations of electron and hole Wannier functions:

1. $\vec{L}_1 = \vec{L}_2 = \vec{L}$ and $\vec{L}_3 = \vec{L}_4 = \vec{M}$

$$-\,a^+_{n_1,\vec{L}}a_{n_2,\vec{L}}d^+_{n_3,\vec{M}}d_{n_4,\vec{M}}\left[A\begin{pmatrix} n_4 & n_1 & n_2 & n_3 \\ \vec{M} & \vec{L} & \vec{L} & \vec{M} \\ v & c & c & v \end{pmatrix} - A\begin{pmatrix} n_4 & n_1 & n_3 & n_2 \\ \vec{M} & \vec{L} & \vec{M} & \vec{L} \\ v & c & v & c \end{pmatrix}\right]. \tag{B.6}$$

These terms describe the Coulomb interaction between an electron and a hole in the corresponding quantum structures. Particularly, terms with $\vec{L} = \vec{M}$ give rise to exciton state localized in the $\vec{L}$th quantum structure. The sum of the terms with $L \neq M$ contribute to a mean value of dipole moment of the system.

2. $\vec{L}_1 = \vec{L}_3 = \vec{L}$, $\vec{L}_2 = \vec{L}_4 = \vec{M}$ and $\vec{L} \neq \vec{M}$

$$a^+_{n_1,\vec{L}}a_{n_2,\vec{M}}d^+_{n_3,\vec{L}}d_{n_4,\vec{M}}\left[A\begin{pmatrix} n_4 & n_1 & n_3 & n_2 \\ \vec{M} & \vec{L} & \vec{L} & \vec{M} \\ v & c & v & c \end{pmatrix} - A\begin{pmatrix} n_4 & n_1 & n_2 & n_3 \\ \vec{M} & \vec{L} & \vec{M} & \vec{L} \\ v & c & c & v \end{pmatrix}\right]. \tag{B.7}$$

These terms describe annihilation of an electron-hole pair in quantum structure $\vec{M}$ and creation of an electron-hole pair in quantum structure $\vec{L}$, therefore representing to transfer of electron-hole pair.

3. All other terms.

These terms describe the annihilation of an initially separated electron-hole pair in different structures and the subsequent creation of another separated electron-hole pair. Since the electron and hole state are strongly confined within each quantum

structure, the overlap between $W_{n,j}(\vec{r}-\vec{L})$ in different quantum structures is small. So these terms are generally very small and can be neglected.

The Hamiltonian in equation (B.3) can be divided into two parts: the sum of Hamiltonians of each individual quantum structures, and the interactions between quantum structures:

$$H = \sum_{\vec{L}} H_{\vec{L}} + \sum_{\vec{L}\neq\vec{M}} H_{\vec{L},\vec{M}} \tag{B.8}$$

with

$$\begin{aligned} H_{\vec{L}} = & \sum_{n,n'} a^{+}_{n,\vec{L}} a_{n',\vec{L}} H^{C}_{n\vec{L},n'\vec{L}} - \sum_{n,n'} d^{+}_{n,\vec{L}} d_{n',\vec{L}} H^{V}_{n\vec{L},n'\vec{L}} \\ & - \sum_{n_1,n_2,n_3,n_4} a^{+}_{n_1,\vec{L}} a_{n_2,\vec{L}} d^{+}_{n_3,\vec{L}} d_{n_4,\vec{L}} \left[A\begin{pmatrix} n_4 & n_1 & n_2 & n_3 \\ \vec{L} & \vec{L} & \vec{L} & \vec{L} \\ v & c & c & v \end{pmatrix} - A\begin{pmatrix} n_4 & n_1 & n_3 & n_2 \\ \vec{L} & \vec{L} & \vec{L} & \vec{L} \\ v & c & v & c \end{pmatrix} \right], \end{aligned} \tag{B.9}$$

and

$$\begin{aligned} H_{\vec{L},\vec{M}} = & \sum_{n,n'} a^{+}_{n,\vec{L}} a_{n',\vec{M}} H^{C}_{n\vec{L},n'\vec{M}} - \sum_{n,n'} d^{+}_{n,\vec{L}} d_{n',\vec{M}} H^{V}_{n\vec{L},n'\vec{M}} \\ & + \sum_{n_1,n_2,n_3,n_4} a^{+}_{n_1,\vec{L}} a_{n_2,\vec{M}} d^{+}_{n_3,\vec{L}} d_{n_4,\vec{M}} \left[A\begin{pmatrix} n_4 & n_1 & n_3 & n_2 \\ \vec{M} & \vec{L} & \vec{L} & \vec{M} \\ v & c & v & c \end{pmatrix} - A\begin{pmatrix} n_4 & n_1 & n_2 & n_3 \\ \vec{M} & \vec{L} & \vec{M} & \vec{L} \\ v & c & c & v \end{pmatrix} \right] \\ & - \sum_{n_1,n_2,n_3,n_4} a^{+}_{n_1,\vec{L}} a_{n_2,\vec{L}} d^{+}_{n_3,\vec{M}} d_{n_4,\vec{M}} \left[A\begin{pmatrix} n_4 & n_1 & n_2 & n_3 \\ \vec{M} & \vec{L} & \vec{L} & \vec{M} \\ v & c & c & v \end{pmatrix} - A\begin{pmatrix} n_4 & n_1 & n_3 & n_2 \\ \vec{M} & \vec{L} & \vec{M} & \vec{L} \\ v & c & v & c \end{pmatrix} \right]. \end{aligned} \tag{B.10}$$

B.2 Band Offset Model and Effective Mass Approximation

The expressions in the bracket of equation (B.4) represent the contributions from the lattice potential $U_{\vec{L}}(\vec{r})$ and the interaction with electrons of a full valence band in different quantum structures. Introducing an effective potential on a single electron in a scheme similar to that of the Hartree-Fock approximation and using

the band offset model for describing the band discontinuity at the interface between different materials, the matrix elements in Eqs. (B.4) can be expressed as

$$\begin{aligned} H^C_{n\vec{L},n'\vec{M}} &= \int W^*_{n,C}(\vec{r}-\vec{L})\left(-\frac{\hbar^2}{2m}\nabla^2+V_0(\vec{r})+\sum_{\vec{L}'}V_{\vec{L}',C}(\vec{r})\right)W_{n',C}(\vec{r}-\vec{M})d\vec{r} \\ H^V_{n\vec{L},n'\vec{M}} &= \int W^*_{n,V}(\vec{r}-\vec{L})\left(-\frac{\hbar^2}{2m}\nabla^2+V_0(\vec{r})+\sum_{\vec{L}'}V_{\vec{L}',V}(\vec{r})\right)W_{n',V}(\vec{r}-\vec{M})d\vec{r} \end{aligned} \tag{B.11}$$

where $V_0(\vec{r})$ represents the periodic effective potential, and $V_{\vec{L},C}(\vec{r})$ and $V_{\vec{L},V}(\vec{r})$ are the potential profiles describing the conduction band offset and valence band offset in the Lth quantum structure.

The Wannier basis $W_{n,j}(\vec{r}-\vec{L})$ in Eq. (B.1) can be well-approximated by the localized electron and hole wave functions in the quantum structure L satisfying

$$\begin{aligned} \left(-\frac{\hbar^2}{2m}\nabla^2+V_0(\vec{r})+V_{\vec{L},C}(\vec{r})\right)W_{n,C}(\vec{r}-\vec{L}) &= E_{n,C}W_{n,C}(\vec{r}-\vec{L}) \\ \left(-\frac{\hbar^2}{2m}\nabla^2+V_0(\vec{r})+V_{\vec{L},V}(\vec{r})\right)W_{n,V}(\vec{r}-\vec{L}) &= E_{n,V}W_{n,V}(\vec{r}-\vec{L}) \end{aligned} \tag{B.12}$$

where $E_{n,C}$ and $E_{n,V}$ are the energy levels in the conduction band and valence band, respectively.

The solution to Eqs. (B.12) using effective-mass approximation are given by

$$\begin{aligned} W_{n,C}(\vec{r}-\vec{L}) &= F_{n,C}(\vec{r}-\vec{L})u_C(\vec{r})\ , \\ W_{n,V}(\vec{r}-\vec{L}) &= F_{n,V}(\vec{r}-\vec{L})u_V(\vec{r})\ , \end{aligned} \tag{B.13}$$

where u_C and u_V are the periodic Bloch wave functions at the conduction band edge and valence band edge respectively, and the localized envelope functions $F_{n,j}(\vec{r}-\vec{L})$ satisfy the corresponding effective mass equations

$$\begin{aligned} \left(-\sum_{\mu,\nu}\frac{\hbar^2}{2m^*_{e,\mu\nu}}\frac{\partial^2}{\partial x_{e,\mu}\,\partial x_{e,\nu}}+V_{\vec{L},C}(\vec{r})\right)F_{n,C}(\vec{r}-\vec{L}) &= \mathcal{E}_{n,C}F_{n,C}(\vec{r}-\vec{L}) \\ \left(-\sum_{\mu,\nu}\frac{\hbar^2}{2m^*_{h,\mu\nu}}\frac{\partial^2}{\partial x_{h,\mu}\,\partial x_{h,\nu}}+V_{\vec{L},V}(\vec{r})\right)F_{n,V}(\vec{r}-\vec{L}) &= \mathcal{E}_{n,V}F_{n,V}(\vec{r}-\vec{L}) \end{aligned} \tag{B.14}$$

where the $m^*_{e,\mu\nu}$ and $m^*_{h,\mu\nu}$ are the effective mass tensors of electron and hole respectively, $\mathcal{E}_{n,C}$ and $\mathcal{E}_{n,V}$ denote electron and hole subband levels.

The matrix elements $H^C_{n\vec{L},n'\vec{M}}$ and $H^V_{n\vec{L},n'\vec{M}}$ describing individual electron and hole states in a quantum structure in equation (B.11) can now be calculated for the following situations:

1. When $\vec{L} = \vec{M}$

$$\begin{aligned} H^C_{n\vec{L},n'\vec{L}} &= \int W^*_{n,C}(\vec{r}-\vec{L})\left(-\frac{\hbar^2}{2m}\nabla^2 + V_0(\vec{r}) + V_{\vec{L},C}(\vec{r})\right) W_{n',C}(\vec{r}-\vec{L})d\vec{r} \\ &= \delta_{n,n'}(E_{0,C} + \mathcal{E}_{n,C}) \\ H^V_{n\vec{L},n'\vec{L}} &= \int W_{n,V}(\vec{r}-\vec{L})\left(-\frac{\hbar^2}{2m}\nabla^2 + V_0(\vec{r}) + V_{\vec{L},V}(\vec{r})\right) W^*_{n',V}(\vec{r}-\vec{L})d\vec{r} \\ &= \delta_{n,n'}(E_{0,V} + \mathcal{E}_{n,V})\,. \end{aligned} \tag{B.15}$$

These terms describe the energies of electrons and holes localized in a single quantum structure.

2. When $\vec{L} \neq \vec{M}$

$$\begin{aligned} H^C_{n\vec{L},n'\vec{M}} &= \int F^*_{n,C}(\vec{r}-\vec{L}) \sum_{\vec{L}'\neq M} V_{\vec{L}',C}(\vec{r})\, F_{n',C}(\vec{r}-\vec{M})d\vec{r} \\ H^V_{n\vec{L},n'\vec{M}} &= \int F_{n,V}(\vec{r}-\vec{L}) \sum_{\vec{L}'\neq M} V_{\vec{L}',V}(\vec{r})\, F^*_{n',V}(\vec{r}-\vec{M})d\vec{r}\,. \end{aligned} \tag{B.16}$$

These terms give rise to tunneling of individual electron and hole. The overlap between the localized envelope functions $F_{n,j}(\vec{r}-\vec{L})$ and $F_{n,j}(\vec{r}-\vec{M})$ determines the magnitudes of the tunneling transfer matrix elements.

B.3 Local Exciton States

The Hamiltonian of a single quantum structure, given in equation (B.9), can now be rewritten in the effective mass approximation as

$$H_{\vec{L}} = \sum_n a^+_{n,\vec{L}} a_{n,\vec{L}}\; (E_{0,C} + \mathcal{E}_{n,C}) - \sum_n d^+_{n,\vec{L}} d_{n,\vec{L}}\; (E_{0,V} + \mathcal{E}_{n,V})$$

$$- \sum_{n_1,n_2,n_3,n_4} a^+_{n_1,\vec{L}} a_{n_2,\vec{L}} d^+_{n_3,\vec{L}} d_{n_4,\vec{L}} \left[A\begin{pmatrix} n_4 & n_1 & n_2 & n_3 \\ \vec{L} & \vec{L} & \vec{L} & \vec{L} \\ V & C & C & V \end{pmatrix} - A\begin{pmatrix} n_4 & n_1 & n_3 & n_2 \\ \vec{L} & \vec{L} & \vec{L} & \vec{L} \\ V & C & V & C \end{pmatrix} \right] . \tag{B.17}$$

The first term of $H_{\vec{L}}$ represents the energy of electrons in the conduction band, and the second that of holes in the valence band. The third term describes the interaction between an electron and a hole in a given structure, which gives rise to the exciton binding.

In the Wannier model, the localized exciton state, which is the eigenstate of $H_{\vec{L}}$, can be constructed from the electron and hole states as

$$\Psi_{\text{ex},\vec{L}} = B^+_{\vec{L}} \Psi_0 = \sum_{n_1,n_2} C_{n_1 n_2,\vec{L}} a^+_{n_1,\vec{L}} d^+_{n_2,\vec{L}} \Psi_0 \tag{B.18}$$

which satisfies

$$H_{\vec{L}} \, \Psi_{\text{ex},\vec{L}} = E_{ex} \, \Psi_{\text{ex},\vec{L}} \, . \tag{B.19}$$

In the effective-mass approximation, the exciton effective-mass equation corresponding to Eq. (B.17) is given by

$$\left[\sum_{\mu,\nu} \left(-\frac{\hbar^2}{2m^*_{e,\mu\nu}} \frac{\partial^2}{\partial x_{e,\mu} \, \partial x_{e,\nu}} + \frac{\hbar^2}{2m^*_{h,\mu\nu}} \frac{\partial^2}{\partial x_{h,\mu} \, \partial x_{h,\nu}} \right) + (E_{0,C} - E_{0,V}) \right.$$
$$\left. + V_C(\vec{r}_e) - V_V(\vec{r}_h) - \frac{e^2}{\epsilon |\vec{r}_e - \vec{r}_h|} \right] \psi_{\text{ex},\vec{L}}(\vec{r}_e, \vec{r}_h) = E_{\text{ex},\vec{L}} \psi_{\text{ex},\vec{L}}(\vec{r}_e, \vec{r}_h) \tag{B.20}$$

with the exciton envelope function determined by

$$\psi_{\text{ex},\vec{L}}(\vec{r}_e, \vec{r}_h) = \sum_{n_1,n_2} C_{n_1 n_2,\vec{L}} F_{n_1,C}(\vec{r}_e - \vec{L}) F^*_{n_2,V}(\vec{r}_h - \vec{L}) \, . \tag{B.21}$$

Here we are only concerned with a single mode of excitation in a given quantum structure. The contributions from all other virtual transitions are included in a background dielectric constant ϵ in the Coulomb interaction between electron and hole[3].

B.4 Exciton Transfer Matrix Elements

B.4.1 Tunneling

The first two terms in equation (B.10) are

$$T_{n\vec{L},n'\vec{M}} = \sum_{n,n'} a^{+}_{n,\vec{L}} a_{n',\vec{M}} \, H^{C}_{n\vec{L},n'\vec{M}} - \sum_{n,n'} d^{+}_{n,\vec{L}} d_{n',\vec{M}} \, H^{V}_{n\vec{L},n'\vec{M}} \,. \tag{B.22}$$

These terms describe the tunneling of individual electrons and holes between quantum structures. The transfer matrix element for a localized exciton state from structure $\vec{L}$ to structure $\vec{M}$ is given by

$$\begin{aligned} T_{\vec{L},\vec{M}} &= < \Psi_{\mathrm{ex},\vec{L}} | \, T_{n\vec{L},n'\vec{M}} \, | \Psi_{\mathrm{ex},\vec{M}} > \\ &= \sum_{\substack{n_1,n_2 \\ n_3,n_4}} C^{*}_{n_1 n_2,\vec{L}} C_{n_3 n_4,\vec{M}} \, H^{C}_{n_1\vec{L},n_3\vec{M}} < W_{n_4,V}(\vec{r}-\vec{M}) | \, W_{n_2,V}(\vec{r}-\vec{L}) > \\ &- \sum_{\substack{n_1,n_2 \\ n_3,n_4}} C^{*}_{n_1 n_2,\vec{L}} C_{n_3 n_4,\vec{M}} \, H^{V}_{n_1\vec{L},n_3\vec{M}} < W_{n_2,C}(\vec{r}-\vec{L}) | \, W_{n_4,C}(\vec{r}-\vec{M}) > \,. \end{aligned} \tag{B.23}$$

The coupling matrix elements $H^{C}_{n\vec{L},n'\vec{M}}$ and $H^{V}_{n\vec{L},n'\vec{M}}$ are given in equation (B.16). Using the expressions in equation (B.13) for the basis functions $W_{n,j}(\vec{r})$ and exciton envelope function given in equation (B.21), $T_{\vec{L},\vec{M}}$ is lead to

$$T_{\vec{L},\vec{M}} = \int \psi^{*}_{\mathrm{ex},\vec{L}}(\vec{r}_e,\vec{r}_h) \sum_{\vec{L}' \neq \vec{M}} \left[V_{\vec{L}',C}(\vec{r}_e) - V_{\vec{L}',V}(\vec{r}_h) \right] \psi_{\mathrm{ex},\vec{M}}(\vec{r}_e,\vec{r}_h) \, d\vec{r}_e \, d\vec{r}_h \,. \tag{B.24}$$

The tunneling transfer matrix element $T_{\vec{L},\vec{M}}$ depends on the overlap of electron and hole wave functions localized in quantum structures $\vec{L}$ and $\vec{M}$. It decreases exponentially as the distance between the two structures increases. The tunneling is important only when the band offsets and barrier thickness are small.

B.4.2 Dipole Transitions

The more interesting means of exciton transfer is embodied in the third term of equation (B.10)

$$\sum_{n_1,n_2,n_3,n_4} a^{+}_{n_1,\vec{L}} a_{n_2,\vec{M}} d^{+}_{n_3,\vec{L}} d_{n_4,\vec{M}} \left[A\begin{pmatrix} n_4 & n_1 & n_3 & n_2 \\ \vec{M} & \vec{L} & \vec{L} & \vec{M} \\ V & C & V & C \end{pmatrix} - A\begin{pmatrix} n_4 & n_1 & n_2 & n_3 \\ \vec{M} & \vec{L} & \vec{M} & \vec{L} \\ V & C & C & V \end{pmatrix} \right] \,. \tag{B.25}$$

This term describes an electron-hole pair initially in quantum structure $\vec{M}$ moving from excited state to the ground state and transferring its energy by Coulomb interaction(or by exchange of virtual photon) to an electron-hole pair in quantum structure $\vec{L}$. The electron-hole pair moves as a single entity.

The transfer matrix element of an electron-hole pair is

$$\begin{aligned} D\begin{pmatrix} n_1 & n_3 \\ n_2 & n_4 \end{pmatrix}_{\vec{L},\vec{M}} &= A\begin{pmatrix} n_4 & n_1 & n_3 & n_2 \\ \vec{M} & \vec{L} & \vec{L} & \vec{M} \\ V & C & V & C \end{pmatrix} - A\begin{pmatrix} n_4 & n_1 & n_2 & n_3 \\ \vec{M} & \vec{L} & \vec{M} & \vec{L} \\ V & C & C & V \end{pmatrix} \\ &= \iint W^*_{n_4,V}(\vec{r}-\vec{M})W^*_{n_1,C}(\vec{r}\,'-\vec{L})\,\frac{e^2}{\epsilon|\vec{r}-\vec{r}\,'|}\,W_{n_3,V}(\vec{r}\,'-\vec{L})W_{n_2,C}(\vec{r}-\vec{M})\,d\vec{r}\,d\vec{r}\,' \\ &- \iint W^*_{n_4,V}(\vec{r}-\vec{M})W^*_{n_1,C}(\vec{r}\,'-\vec{L})\,\frac{e^2}{\epsilon|\vec{r}-\vec{r}\,'|}\,W_{n_2,C}(\vec{r}\,'-\vec{M})W_{n_3,V}(\vec{r}-\vec{L})\,d\vec{r}\,d\vec{r}\,'\,. \end{aligned} \tag{B.26}$$

The transfer matrix element between localized exciton states is given by

$$\begin{aligned} \Gamma_{\vec{L},\vec{M}} &= <\Psi_{\text{ex},\vec{L}}|\sum_{n_1,n_2,n_3,n_4} a^+_{n_1,\vec{L}}a_{n_2,\vec{M}}d^+_{n_3,\vec{L}}d_{n_4,\vec{M}}\,D\begin{pmatrix} n_1 & n_3 \\ n_2 & n_4 \end{pmatrix}_{\vec{L},\vec{M}}|\Psi_{\text{ex},\vec{M}}> \\ &= \sum_{\substack{n_1,n_3 \\ n_2,n_4}} C^*_{n_1n_3,\vec{L}}C_{n_2n_4,\vec{M}}\,D\begin{pmatrix} n_1 & n_3 \\ n_2 & n_4 \end{pmatrix}_{\vec{L},\vec{M}}\,. \end{aligned} \tag{B.27}$$

In simple two-band model represented by Eq. (B.21), the transfer matrix element can be written as

$$\begin{aligned} \Gamma_{\vec{L},\vec{M}} &= \iint \psi^*_{\text{ex},\vec{L}}(\vec{r}\,',\vec{r}\,')u^*_C(\vec{r}\,')u_V(\vec{r}\,')\,\frac{e^2}{\epsilon|\vec{r}-\vec{r}\,'|}\,\psi_{\text{ex},\vec{M}}(\vec{r},\vec{r})u_C(\vec{r})u^*_V(\vec{r})\,d\vec{r}\,d\vec{r}\,' \\ &- \iint \psi^*_{\text{ex},\vec{L}}(\vec{r}\,',\vec{r})u^*_C(\vec{r}\,')u_V(\vec{r})\,\frac{e^2}{\epsilon|\vec{r}-\vec{r}\,'|}\,\psi_{\text{ex},\vec{M}}(\vec{r}\,',\vec{r})u_C(\vec{r}\,')u^*_V(\vec{r})\,d\vec{r}\,d\vec{r}\,'\,. \end{aligned} \tag{B.28}$$

If the overlap between localized wave functions in different quantum structures is small, the second term in (B.28) can be neglected.

Exciton is quantized polarization field and can be regarded as a system with a transition dipole moment. Eq. (B.28) actually indicates that the process of exciton transfer is through the interaction of near field dipole-dipole transitions. Define the transition dipole moment between the conduction band and the valence band as

$$\vec{\mu} = e\,<u_V\,|\vec{r}\,|\,u_C>_{\text{cell}}\,. \tag{B.29}$$

Expanding the Coulomb interaction through the dipole term and noticing that the term corresponding to the monopole moment gives zero because $< u_V \,|\, u_C >_{\text{cell}} = 0$, the transfer matrix element $\Gamma_{\vec{L},\vec{M}}$ can be expressed as

$$\Gamma_{\vec{L},\vec{M}} = \iint \psi^*_{\text{ex},\vec{L}}(\vec{r}\,', \vec{r}\,') \, \frac{\vec{\mu}^*_{\vec{L}} \cdot \vec{\mu}_{\vec{M}} - 3(\vec{\mu}^*_{\vec{L}} \cdot \hat{n})(\vec{\mu}_{\vec{M}} \cdot \hat{n})}{\epsilon |\vec{r} - \vec{r}\,'|^3} \, \psi_{\text{ex},\vec{M}}(\vec{r}, \vec{r}) \, d\vec{r} \, d\vec{r}\,' \quad \text{(B.30)}$$

where $\hat{n}$ is the unit vector along the direction of $(\vec{r} - \vec{r}\,')$.

The oscillator strength characterizing the interaction of exciton with electromagnetic field is given by

$$\begin{aligned} f_{\text{ex},\vec{L}} &= \frac{2}{mE_{\text{ex},\vec{L}}} \left| < \Psi_{\text{ex},\vec{L}} \,|\, \vec{P} \,|\, \Psi_0 > \right|^2 \\ &= \frac{2}{mE_{\text{ex},\vec{L}}} \left| \sum_{n_1,n_2} C_{n_1 n_2,\vec{L}} < F_{n_2,V}(\vec{r} - \vec{L}) \, u_V(\vec{r}) \,|\, \vec{p} \,|\, F_{n_1,C}(\vec{r} - \vec{L}) \, u_C(\vec{r}) > \right|^2 \\ &= \frac{2mE_{\text{ex},\vec{L}}}{\hbar^2 e^2} \, |\mu|^2 \left| \int \psi_{\text{ex},\vec{L}}(\vec{r}, \vec{r}) \, d\vec{r} \right|^2 . \end{aligned} \quad \text{(B.31)}$$

We see the transfer matrix element $\Gamma_{\vec{L},\vec{M}}$ is proportional to the exciton oscillator strength $f_{\text{ex},\vec{L}}$ and depends on the exciton polarization.

Unlike tunneling mechanism, exciton transfer matrix element due to dipole interaction is long range. In low dimensional quantum structures, the additional confinement will give rise to enhanced exciton oscillator strength, and thereby, increased transfer matrix element.

Bibliography

[1] W. R. Heller and A. Marcus, *Phys. Rev.* **84**, 809 (1951).

[2] H. Haken, *Quantum Field Theory of Solids, An Introduction*, (North-Holland Publishing Company, Amsterdam, New York, 1976), chapter IV.

[3] J. J. Hopfield, *Phys. Rev.* **112**, 1555 (1958).